Alma Mater Studiorum - Università di Bologna

DOTTORATO DI RICERCA IN

MONITORAGGIO E GESTIONE DELLE STRUTTURE E DELL'AMBIENTE - SEHM2

Ciclo 35

Settore Concorsuale: 09/H1 - SISTEMI DI ELABORAZIONE DELLE INFORMAZIONI

Settore Scientifico Disciplinare: ING-INF/05 - SISTEMI DI ELABORAZIONE DELLE INFORMAZIONI

SENSOR NETWORKS OPTIMIZATION AND SOFTWARE DEVELOPMENT FOR STRUCTURAL HEALTH MONITORING BASED ON ULTRASONIC GUIDED WAVES

Presentata da: Marco Dibiase

Coordinatore Dottorato

Luca De Marchi

Supervisore

Marco Patella

Co-supervisore

Luca De Marchi

Esame finale anno 2023

Contents

Acknowledgements

My personal acknowledgments are written in Italian language, because, in my opinion, the native language better conveys what I want to say.

In primo luogo tengo a ringraziare molto i miei supervisori: i Professori Marco Patella e Luca De Marchi. In particolare tengo a ringraziare molto Marco Patella per l'ampia libertà di ricerca concessami, per la massima cordialità e disponibilità sempre mostratemi. Per la condivisione di diversi punti di vista. Per la possibilità di poter sfruttare il potenziale fisico/matematico in processi di ottimizzazione, al fine di ottenere dati "migliori" come input per algoritmi AI. Così affascinanti per la loro difficile interepretabilità, tipica dei sistemi complessi, mi auspico di poterli applicare, in virtù anche delle conoscenze acquisite in tale campo, in sviluppi futuri.

Tengo a ringraziare in particolar modo Luca De Marchi. Per essermi stato da guida in questo percorso di dottorato. Per i confronti sempre così interessanti e costruttivi tenuti su una moltitudine di aspetti di lavoro. Per le sue indicazioni sempre di aiuto e lungimiranti. Per le possibilità future prospettatemi. Per le sue qualità professionali e umane, capaci, puranco in un periodo storico e sociale complesso, di influire sempre positivamente sulla produttività lavorativa e non solo.

È da tempo immemore che vorrei ringraziare, in qualche modo, mia madre, Enrica Migli. Sebbene non abbia avuto la possibilità di averla accanto in questo percorso, vorrei ringraziarla per i valori e le qualità trasmessemi. In questo contesto ne cito solo due: l'impegno nello studio, diventato quindi lavoro in questi anni, assieme alla capacità di averne passione, senza la quale mancherebbe una spinta propulsiva a perseguire il meglio. La fiducia, nei propri mezzi e capacità. Ciò che posso e oso dire, è che per quanto non mi sia potuta essere più compagna di viaggio, questi valori sono rimasti in me intatti, come lei avrebbe desiderato.

Un ringraziamento speciale va alle persone a me care. A mio padre, Antonio, pronto per ogni evenienza. A mio fratello Massimiliano, per la capacità di trasmettere pragmaticità e forza d'animo. A sua moglie, Beatrice Condrò, per la sua gentilezza e familiarità, e alla mia nipotina Emilia, in grado di trasmettere gioia ed entusiasmo nella scoperta quotidiana delle piccole cose. Ringrazio i miei zii, Angelo e Filomena, diventati per me figure di riferimento. *La mia zia Giancarla* e mia cugina Grazia per essermi state sempre di supporto, nonostante le distanze. Il mio amico Francesco, per avermi supportato e sopportato specie durante alcuni monologhi fisico-matematici, apparentemente incomprensibili per i non "addetti ai lavori".

Tengo a ringraziare Daniele D'Andreamatteo, per la sua amicizia e per quella intesa instauratasi sin dai primi anni di studi universitari, rimasta sempre salda nel confronto intellettuale ed umano, lungo i nostri percorsi di vita. Vorrei ringraziare Federica Zonzini per la sua sempre grande disponibilità e gentilezza per ogni evenienza lavorativa. Per dei momenti di condivisione, capaci di rafforzare lo spirito proprio dei ricercatori. Chiedo venia alle persone a me care che non ho esplicitamente citato e che mi hanno accompagnato in questi anni di riflessione, di cambiamento e di ricerca incessante, nell'appagamento di quella instancabile curiosità sulla natura delle cose per il loro miglior impiego ingegneristico.

Infine, un ringraziamento speciale alla Scuola di Ingegneria dell'Università di Bologna. Capace di fornire una qualità di formazione invidiabile all'interno del panorama universitario mondiale. Che i suoi valori fondanti, quali la creatività, la condivisione, l'integrazione, l'eccellenza, siano sempre alla base dell'intera comunità.

Abstract

The Structural Health Monitoring (SHM) research area is increasingly investigated due to its high potential in reducing the maintenance costs and in ensuring the systems safety in a wide range of industrial application fields. A growing demand of new SHM systems, permanently embedded into the structures, for savings in weight and especially in cabling, comes from the aeronautical and aerospace application fields. As consequence, the embedded electronic devices are to be wirelessly connected and battery powered. To this aim, a low power consumption for the data transfer to central units and a reduced computational cost for the data processing are the main constraints to be satisfied. At the same time, high performance in defects or impacts detection and localization are to be ensured to assess the structural integrity. In order to achieve these goals, the design paradigms can be changed together with the associate signal processing.

The present dissertation proposes design strategies and unconventional solutions, suitable both for real-time monitoring and periodic inspections, relying on piezo-transducers and Ultrasonic Guided Waves (GWs). In the first context, arrays of closely located sensors were designed, according to appropriate optimality criteria, by exploiting sensors re-shaping and optimal positioning, in order to achieve improved damages/impacts localisation performance in noisy environments. Therefore, two different solutions, referred to as *Shaped Sensors Optimal Cluster* (SS-OC) and *Disk Sensors Optimal Cluster* (DS-OC) were designed and numerically assessed. A dedicated signal processing, based on the waves time-delays estimation, was developed to attain the estimation performance lower bound.

An additional sensor re-shaping procedure was developed to tackle another well-known issue which arises in realistic scenario, namely the reverberation or multi-path propagation. The designed sensor, referred to as *Directive Complex*

Sensor (DCS), able to filter undesired mechanical boundaries reflections, was validated via simulations based on the Green's functions formalism and FEM. The estimation performance of a DCSs array was assessed in some realistic cases, when multiple edge reflections and noise affect the measurements.

In the active SHM context, a novel design methodology was used to develop a single transducer, called *Spectrum-Scanning Acoustic Transducer* (S-SAT), to actively inspect a structure. It is able to estimate the number of defects and their distances with an accuracy of 2[cm]. It can estimate also the damage angular coordinate with an equivalent mainlobe aperture of 8[deg], when a 24[cm] radial gap between two defects is ensured. A suitable signal processing was developed in order to limit the computational cost, allowing its use with embedded electronic devices.

Acronyms

2D-FT Bi-dimensional Fourier Transform

ADA Average Directional Attenuation

AE Acoustic Emission

AFR Amplitude Frequency Response

ANN Artificial Neural Networks

AS Acoustic Source

AUGN Additive Uncorrelated Gaussian Noise

AWGN Additive White Gaussian Noise mode

BR Barankin bound

CC Cross-Correlation

CoV Calculus of Variations

CRLB Cramér–Rao Lower Bound

CRMB Cramér Rao Matrix Bound

CRT Complex Radon Transform

DA Directional Attenuation

DAS delay-and-sum

DCS Directive Complex Sensor

DDoP Difference in Distance of Propagation

DL Deep Learning

DoA Direction of Arrival

DS-OC Disk Sensors Optimal Cluster

DToAs Differences in Time of Arrival

e-NDE embedded non-destructive evaluation

EUSR Embedded Ultrasonic Structural Radar

FFT Fast Fourier Transform

FI Fisher Information

FIM Fisher information Matrix

f-IR Frequency Impulse Response

FrT Frequency-Time

F-SAT Frequency Steerable Acoustic Transducer

GCC Generalized Cross-Correlation

GCC-PHAT GCC with phase transform

GFs Green's functions

GM Gauss-Markov

GP Gaussian Pulse

GW Guided Waves

HT Hilbert Transform

IRT Inverse Radon Transform

IS Image Sources

ME Maximum Error

ML Maximum Likelihood

MSE Mean Square Error

M-L Machine Learning

NDE Non Destructive Evaluation

P pressure (waves)

pdf probability density function

PSNR Peak Signal to Noise Ratio

PVDF polyvinylidene fluoride

PZT lead zirconate titanate

RT Radon Transform

S shear (waves)

SC Standard Cluster

SD Standard Deviation

SHM Structural Health Monitoring

SNR Signal to Noise Ratio

S-SAT Spectrum Scanning Acoustic Transducer

S-SAT Spectrum-Scanning Acoustic Transducer

SS-OC Shaped Sensors Optimal Cluster

Introduction

Motivations

In the last decades, structural Non Destructive Evaluation (NDE) techniques have been used in many application contexts, e.g. civil, industrial, aerospace etc., for identifying local damage, in order to prevent systems failure and ensure safety. Among them, ultrasonic inspections have been widely investigated and exploited [1]. Conventional ultrasonic methods use piezoelectric probes placed on the structural surface to excite ultrasonic waves and "listen" anomalous echoes due to damages (*pulse-echo* method). Alternatively, the excited waves are acquired by a secondary transducer. The wave dispersion and attenuation due to diffused damage in the material are used as flaw indicators (*pitch-catch* method). Both methods require the usage of an *active* transducer to excite ultrasonic waves and perform a structural inspection.

In more recent times, a transition has been observed from the conventional NDE techniques to approaches based on permanent installed instruments, which define the Structural Health Monitoring (SHM) field. The benefits are multiple. While ultrasonic NDE methods require time-consuming mechanical inspections and to put offline the tested structures, the SHM ones allow to perform inspections on in-service systems via embedded sensors, able to detect critical damages and to prevent incipient structural collapses. Moreover, the SHM field makes possible real-time monitoring: embedded *passive* piezoelectric sensors are able to detect Acoustic Emissions (AEs) due to defects growth or impacts with objects. As result, besides the opportunity to improve the systems safety, SHM technologies enable to estimate the remaining life of the structures, particularly important for the ones that are beyond their design life, and to reduce the maintenance costs.

For their high potentials, a growing demand of SHM systems comes from different application fields, such as the aeronautic and aerospace ones. In particular, the latter additionally require embedded monitoring systems with a reduced weight. Typically, the main weight contribution is determined by the cabling. Wireless and battery powered embedded devices for data acquisition, pre-processing and transfer to a central unit are often the only feasible approach. Unfortunately, they needs a low power consumption which, in turn, requests a reduced amount of data to be transferred and a low computational cost for the in-site signal processing. If these constraints are to be satisfied, on the other hand, the performance of the monitoring systems in flaw detection and localization has to remain high, even when issues, such as noise and reverberation, arise. This PhD research work was conducted to tackle these issues.

In this Thesis, both passive and active monitoring techniques are investigated. Regarding the first ones, the basic idea is to exploit interconnected nodes, composed by a cluster of closely located passive piezo-sensors and an electronic device, such as a micro-controller unit, in charge to acquire, pre-process and transfer the data. Each node can estimate the wave-fronts Direction of Arrival (DoA) on each cluster. Multiple DoAs estimations, provided by different nodes, allow to locate an Acoustic Source (AS), given by a flaw growth or an impact. Acoustic Sources generate Ultrasonic Guided (Lamb) Waves (GWs) in thin-plate structures, e.g. the aircraft wing skins. This kind of waves cover large distances with low attenuation but are prone to dispersion.

The corruption induced by noise, reverberations and dispersion were addressed, mainly, at the sensors array design level, by exploiting the arrangement and the shape of piezo-transducers. After defining suitable optimality criteria, the *Shaped Sensors Optimal Cluster* (SS-OC) and the *Disk Sensors Optimal Cluster* (DS-OC) were designed for a more robust DoA estimation for noise affected measurements.

In order to address the spatial colored noise, i.e. directional interference due to edges reflections/reverberation, an unconventional array base sensor, refereed to as *Directive Complex Sensor* (DCS) was designed. Its directivity properties, able to filter GWs with a DoA out of the monitored angles work-range, were double assessed via two different simulation methods (the Green's functions (GFs) formalism-based simulations and the well-known FEM ones).

In the active SHM context, firstly a design procedure was investigated and well-formalized to excite directional waves, developing a less general procedure firstly proposed in [2]. After that, a novel single piezo-transducer, referred to as *Spectrum-Scanning Acoustic Transducer* (S-SAT) was designed to inspect a structure with an equivalent mainlobe aperture of 8°. According to the embedded applications context which require a low power consumption, both the design and the defined signal processing were developed to limit the computational cost.

Contributions

The research work illustrated in this Thesis led to the following contributions:

- A novel array consisting in 3 shaped-sensors was designed. An optimality criterion based on the Theory of the Measurements and the Calculus of Variations was proposed to find the optimal sensors shapes. The obtained array is referred to as *Shaped Sensors Optimal Cluster.* A numeric validation, based on the Green's functions formalism, shows improved performance in wave-front DoA estimation when compared to a *Standard Cluster* (SC) of conventional disk-sensors.

- The Radon Transform, a math-tool used to shape appropriately the piezo-sensors, was exploited to compute the time-response of a piezo-load, with an arbitrary shape, to take into account both the *wave-number tuning* effect and *dispersion.*

- A refined optimal criterion based on system and noise modeling, on Estimation Theory techniques, and on the assumption of unknown wave velocity, was developed to find the optimal M-disk-sensors positioning within a restricted array area, i.e. a circle of fixed radius. Such criterion was then applied to the case of a three sensors array (called *Disk Sensor Optimal cluster*). A DoA efficient estimator was derived on the basis of the *Gauss-Markov* time-delays estimation. The DS-OC and the efficient DoA estimator provided increased performance w.r.t. a SC and conventional time-delays procedures.

- The piezo-sensor reshaping procedure was used to design a novel base sensors for array, refereed to as *Directive Complex Sensor*, to filter undesired directional interference such as edge reflections. The design procedure and the DCS effectiveness was validated via a double numerically assessment thanks to the GFs simulations and FEM ones. The double numerical check allowed to assess the GFs simulator, widely employed for the numerical tests both in the passive SHM context and the active one.

- In the active SHM context, the double-phase design procedure proposed in [3] to excite directional waves, was reviewed and linked to the procedure proposed in [2] with a novel mathematical formulation.

- A novel single Transducer, able to simultaneously inspect an angular range of 360°, was designed according to the Encoder principles. It is referred to as *Spectrum-Scanning Acoustic Transducer*. The number of defects and their distances can be estimated with an accuracy of just 2[cm]. An equivalent mainlobe aperture of 8[deg] was achieved, when a 24[cm] radial gap of two different defects is ensured. The design and the signal processing were developed to minimize the computational cost, enabling its use for low power consuming electronic devices.

Organization

The manuscript is subdivided as follows. In Chapter 1 a brief overview on the NDE-SHM transition and the passive ultrasonic SHM techniques is presented. The SHM methods which uses cluster of closely located piezo-sensor was selected as the most suitable technique for low power embedded devices. In Chapter 2, the Lamb Waves Theory, a model for the frequency response of a piezo-sensor in presence of a Lamb wave mode and the GFs formalism simulation are illustrated. In Chapter 3, a cluster of three sensors optimally shaped is provided. The improved performance in defect/impact acoustic emissions DoA estimation are shown w.r.t. the SC of three disk-sensors. In Chapter 4 a more refined optimality criterion for the sensor positioning, when wave velocity is unknown, is defined and applied to the case of three-disks array. A DoA efficient estimator is found. The performance increase in

DoA estimation is assessed numerically. In Chapter 5, the reverberation issue is addressed by design novel shaped-sensor arrays, able to filter undesired directional interference. The Chapter 6 is entirely dedicated to active SHM. A design procedure and a suitable excitation signal to excite directional waves is illustrated and linked to the less general model presented in [2]. A novel Transducer, called S-SAT, is proposed. The design criteria and procedure are detailed shown, together with the signal processing which was developed to limit the computational cost. Finally, conclusions and future developments are provided in Chapter 7.

Chapter 1

Passive Monitoring

1.1 Transition from NDE to SHM

In the last decades, a large number of Non-Destructive Evaluation (NDE) techniques have been proposed and used, able to test the structural integrity, avoiding invasive inspections which could compromise the future usefulness. NDE techniques have been developed relying on different inspection typologies, such as X-Rays, Electromagnetic fields, Acoustic Emissions, etc. Among them, ultrasonic inspections have been widely investigated and used [1, 4]. A conventional ultrasonic NDE techqniques relies on time-consuming, meticulous, trough-the thickness scans, obtained by moving a transducer mechanically along the surface, e.g. aircraft shells, tanks, pipelines etc. In this way, flaws, such as cracks can be detected via anomalous acoustic echoes. Alternatively, Guided Lamb waves (GWs) [5] can be generated to inspect large distances with low attenuation. A brief review of guided wave theory is given in Ch. (2). Here, we observe that the Lamb waves are dispersive, i.e. their wave velocity depends by the frequency, according to the *dispersion curve*, and have a multi-mode character, i.e. each wave-mode has a different behaviour (symmetric or antisymmetric) and a characteristic dispersion curve. The multi-mode property can be used to detect different defect typologies, thanks to the higher sensitive of certain modes with respect to some damages [6]. However, often the wave dispersive behaviour may complicate the acquired signal interpretation. GWs are appropriate for thin-plate and shell structures. They have shown the ability to detects not only cracks but also disbounds in metallic and composite structures [7].

With the technological evolution, increasingly smaller, lighter and more sensitive piezoelectric sensors have been produced, replacing the conventional piezoelectric ultrasonic probes (see [7]) . As result, conventional NDE techniques have been applied in the emerging research area known as Structural Health Monitoring (SHM).

SHM techniques use sensors/transducers permanently embedded (attached or integrated) into the structure to be monitored. Unlike the conventional ultrasonic methods, the SHM ones can be divided in passive and active. In the passive methods, the sensors only "listen" the acoustic waves generated by ASs due to damages or undesired impacts of external objects with the structure. In this case, a real-time monitoring is performed.

Conversely, the active SHM approaches use transducers both as actuators and receivers. Active sensors interact with the structure in much the same way that conventional NDE transducers do. For this reason, active SHM can be also viewed as embedded non-destructive evaluation (e-NDE), i.e. an NDE method that utilizes embedded transducers. Viewing active SHM from the e-NDE point of view allows us to draw on the experience already developed in the NDE field and to transition it into SHM applications.

For an overview on the most commonly adopted techniques for active SHM, refer to Ch. (6), entirely dedicated to the active monitoring.

In the following, some passive SHM techniques will be investigated considering their pros and cons. Among them, a technique will be selected for its considerable advantages and considered for the following chapters related to the passive monitoring for the AS localisation.

1.2 Ultrasound Passive SHM techniques: Background

In the ultrasonic passive SHM context, different techniques have been proposed and used. In this Section, some of them will be presented with their advantages and disadvantages, with a special focus on the computational cost. The last aspect is due to one of the main aim of the research work illustrated in this dissertation: SHM sensor systems development which are suitable for an embedded low computational cost signal processing. Indeed, such SHM approaches are demanded by aerospace and aeronautical fields where low power wireless devices can be used, allowing to limit the monitoring system wiring. In the following, a brief overview of the main passive SHM techniques presented in literature is provided.

1.2.1 Time reversal

The time reversal method was developed by Fink [8] in the NDE context, namely in the active one. It was observed that by using a transducer as actuator and a second one as receiver (*pitch-catch* method), if the acquired signal is time-reversed and sent back, also the medium effects are reversed. Therefore, the input signal is equal to the acquired sent back signal. This behaviour is explained thanks to the the linear reciprocity of a propagation system [9]. In the passive SHM context, if a wave is detected, by knowing the accurate modeling of the ultrasonic propagation, it can be simulated the inverse propagation to find the points where waves energy concentrates, i.e. the acoustic sources. Ing and Fink in [10] showed experimentally that the extensive dispersion of certain Lamb wave modes can be almost completely compensated through the time reversal method. The time-reversal method, used for the ultrasonic imaging, i.e. for the passive monitoring, requires to know previously the structural parameters or to measure them [11]. However, the main limitations of inverse methods, are that they require a high computational cost. As consequence, both the wireless-transmission of the entire acquired signal and the reversal simulation on the in site devices, are incompatible with the low-power embedded systems.

1.2.2 Hyperbolic positioning

The Hyperbolic positioning methods can be easily explained observing Fig. (1.1). Each time-delay of wave signal between two sensors defines an hyperbole on the geometric top plane, whose foci are given by the sensors location. The AS positioning can be estimated as the intersection point of geometric hyperbola derived by the

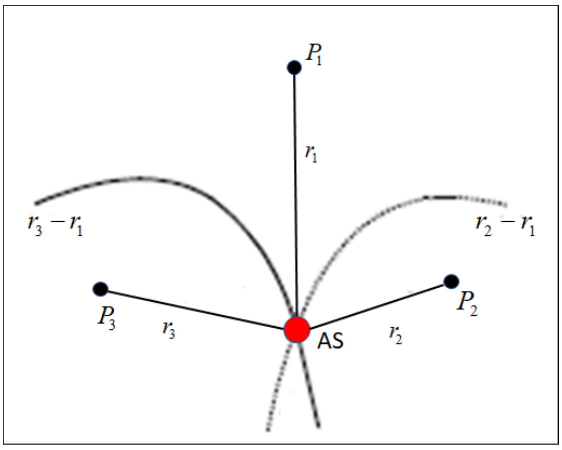

Figure 1.1: A graphical illustration of Hyperbolic positioning methods. The differences in time of arrival of wave-fronts (time-delays) between sensors define the differences in distances in the figure. They define hyperbola on the plane, whose intersection determines the AS location.

time delays. In non-dispersive context, efficient hyperbolic estimators were provided [12]. However, in a dispersive context, such as the GWs propagation, the wave packets spread over the time according to the wave velocity-frequency relation, i.e. the dispersion curve [13], of the GWs propagating mode. The larger the distance between the AS and the sensor, the more "dispersed" the signal. Therefore, each sensor acquires a different signal related to the same AS. Although signals can be compensated via efficient dispersion compensation procedures [14], it is necessary to know *a priori* the disperion curves, namely the material properties. Apart from that, the hyperbolic positioning methods require a large number of distant and well-synchronized sensors in order to reduce the estimation uncertainty. In [14] the lower bound in the AS estimation via the dispersion compensation and hyperbolic positioning methods was formally derived. It depends by the sensors number and displacement, the AS location and the “errors” which affect the measurements given by the differences in distance (see Fig. (1.1)). In practical cases the errors are independent identically distributed Gaussian random variables with zero mean and standard deviation σ_r. The last one can be estimated, for high Signal to Noise Ratio (SNR) values, as:

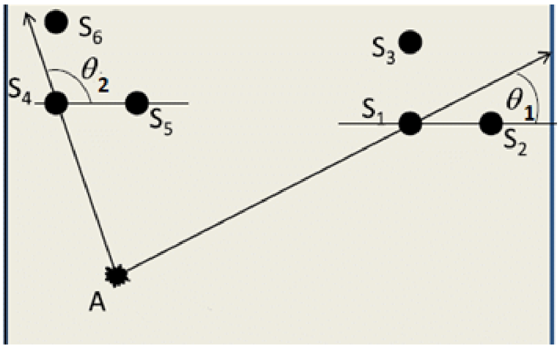

Figure 1.2: A graphical illustration of the AS localization via the DoAs estimation (see [16]). By estimating the DoAs of wave-front (the angles) on each cluster, the AS can be estimated via triangulation procedures by knowing the distance between two (or more) arrays. The DoAs are estimated via the time-delays between the sensors of each cluster.

$$\sigma_r = v_s \left(2/f_s + \delta t_{wf}\right) \tag{1.1}$$

Where v_s is the (constant) wave velocity of the compensated signals, f_s is the sampling frequency and, finally, δt_{wf} is the time uncertainty due to a wireless connection. Different methods have already been proposed to increase the WiFi synchronisation uncertainty (δt_{wf}) down to some microseconds [15]. Nevertheless, as illustrated in [14] via experimental results and considering different arrangements of 3-4 sensors, for certain impact locations the AS estimation error (which attains the lower bound, when the edge reflections don't effect the measurements error) can be already high without the supplementary δt_{wf} uncertainty. As result, the wireless connection can lead to an AS estimation error which is not tolerable.

1.2.3 Directions of Arrival (DoAs) on sensors-arrays

Arrays of closely located sensors can be used to estimate the AS location. In an isotropic or slightly anisotropic structure, by estimating the Direction of Arrivals (DoAs) of wave-front, i.e. the angles of arrival, on each sensor-cluster, the AS can be estimated via simple triangulation procedures by knowing the distance between two or more arrays (see Fig. (1.2)).

The DoA estimation performance of a simple cluster of three circular sensors placed on the vertices of an isosceles right triangle, with unknown wave velocity, was widely investigated by kundu et al. in [16, 17, 18]. The DoA estimation is performed by means of the Differences in Time of Arrival (DToAs) estimations, i.e. time-delays. They are estimated via Cross-Correlation (CC) procedures. Given two functions $f(t)$ and $g(t)$ (e.g. two acquired signals which are equal except for a time-shift and spurious components due to the noise), defined on two supports T_1 and T_2 over a domain $[t_0, t_0 + T] \subseteq \mathbb{R}$, the observation time, the CC procedure is defined by the product:

$$(f * g)(\tau) = \int\limits_{-\infty}^{\infty} f^*(t) g(t + \tau) dt \tag{1.2}$$

where the last integral can be computed just within $[t_0 - T, t_0 + T]$ and τ, called *displacement* or *lag* can be made to vary just between $t_0 - T$ and $t_0 + T$. It can be computed efficiently in the frequency domain. Indeed, similarly to the convolution theorem, the cross-correlation satisfies:

$$F\{f * g\} = F^*\{f\} F\{g\} \tag{1.3}$$

where F denotes the Fourier Transform. The time-delays are computed by determining the $(\tau_{max} - T)$ value which maximize the CC function (1.2). In [19], it was proved that the last method is a Maximum Likelihood (ML) estimator approximation in presence of Additive Uncorrelated Gaussian Noise (AUGN).

It is worth noting that the time-delays can be easily estimated also in the GWs propagation case, when the wave energy is concentrated in narrowband spectra. Laboratory tests have shown that the A_0 mode Acoustic Emissions (AEs) due to screwdriver low-speed impacts on an aluminium plate, are already narrowband. This kind of impacts typically are generated by tool drops during the off-line maintenance of aeronautical structures [20]. In the most general case, AEs due to different types of impact or to defects growth can be wideband. However, it is always possible to decompose the acquired signal, through filters bank, in multiple narrow-band signals and perform the time-delays estimation many times for a more robust estimation in presence of noise.

Furthermore, multiple clusters can be used to estimate the AS localization even

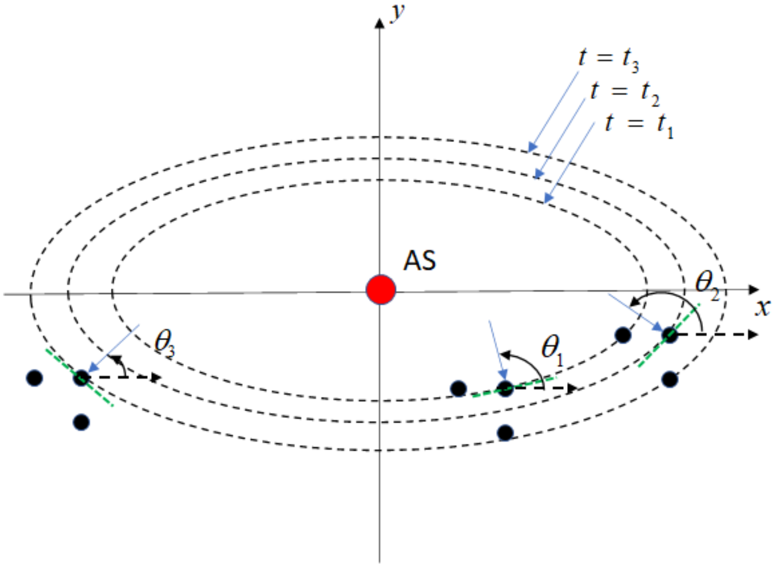

Figure 1.3: A graphical illustration of the AS localization in case of elliptic wave-fronts. By estimating the DoAs at each clusters and knowing their positioning, a three equations system can be solved to find the ellipsis center point coordinates, C_x and C_y, and the major axis/minor axis ratio, γ (see work [21]).

in case of highly anisotropic structures. For example, in Fig. (1.3) it is shown the case of elliptical wave-fronts. In [21], Park et al. estimated the ellipsis center point coordinates, C_x and C_y, and the major axis/minor axis ratio, γ, by estimating the DoAs at three clusters. Therefore, three equations are established to solve three unknowns (γ, C_x, C_y). In [22], Sen and Kundu addressed the cases of different wave-fronts shape by introducing others geometric parameters to be estimated.

Aljets et al. in [23] proposed a different approach for the AS localisation. In particular, only one three-sensors cluster was used to estimate both the angular coordinate and the radial one. For the last aim, two modes, i.e. A_0 and S_0, are to be firstly detected. By knowing their velocity and estimating their time difference, it is possible to estimate the AS distance. Grigg et al. in [24] proposed a second differential empirical method for modal analysis which appears effective also in complex structures. Although the last methods require just one cluster, they involve the additional complexity to separate two modes and compute their time difference on the sensors (see [23, 24]). Vice versa, the method which exploits the DoAs at two or more sensors-cluster can be used considering just the more energetic

AS Estimation Methods	***Wave velocity knowledge***	***Usability on anisotropic structures***	***Sensor wireless synchonisation***	***Power consumption***
Time Reversal [8, 9, 10, 11]	Requested	Yes	Not requested	High (due to the inverse modelling or to the wi-fi long-lasting signal transferring)
Hyperbolic Positioning [12, 14, 15]	Requested	A modified method is requested	Requested (order of [us])	High (due to the wi-fi long-lasting signals transferring)
Single Sensor Array [23, 24]	Requested	Yes (wave velocity knowledge as function of the DoA is requested)	Not requested	Low (short time delays estimation and double mode detection)
Multiple Sensor Arrays [16, 17, 18, 21, 22]	Not requested	Yes (different strategies have already been tested)	Requested (order of [s])	Low (short time delays estimation on each array)

Table 1.1: Comparison of AS estimation methods in terms of four different aspects which impact on their usability.

wave-signal parts (e.g. typically due to the A_0 mode) [16, 17, 18]. A comparison of the considered AS estimation methods in terms of the main aspects, which impact on their usability, is given in Tab. (1.1). As conclusion, the method based on multiple DoA estimations (i.e. multiple arrays), thanks to its low computational cost to perform CC products (1.3), and with the additional advantage of being agnostic to the material properties (i.e. unknown wave-velocity [16] which can vary with the DoA in anisotropic structures [21, 22]), was selected as the ground basis for the structural monitoring approaches investigated in this dissertation. In the following, the design paradigm of conventional sensors-arrays will be changed, as well as the classical estimation procedures, in order to address typical issues which arise in realistic scenarios, such as noise and reverberation.

Chapter 2

Guided Waves

2.1 Lamb waves Theory

In an infinite solide medium, elastic waves can propagate only in two basic modes: pressure (P) waves and shear (S) waves. In Fig. (2.1), the motion of the two modes is illustrated. However, if the medium is bounded, wave reflections accour and more complicated wave patterns emerge. Of particular interest are the Guided Waves (GWs), which remain contained in a wave guide and can travel at large distances.

In a thin-wall structure, namely when one dimension is small compared to the other two, guided waves propagate as Lamb waves [5]. Thanks to the coverage of large distances with a low attenuation, the Lamb waves result to be well suited for the SHM in many applications fields, such as industrial, automotive, nautical, aeronautical and aerospace.

In flat plates, Lamb waves can be symmetric or anti-symmetric with respect to the plate mid-plate. A brief outline of the main equations is presented in this dissertation, following [13, 7].

Let's start by considering the equation of motion for an isotropic elastic medium, given by:

$$\mu\nabla^2\mathbf{u}+(\lambda+\mu)\nabla\nabla\cdot\mathbf{u}\equiv\rho\frac{\partial^2\mathbf{u}}{\partial t^2} \tag{2.1}$$

where λ and μ are the Lamé constants, ρ is the mass density, and $\mathbf{u}$ is the displacement vector. By using the potentials method, the displacement $\mathbf{u}$ is written

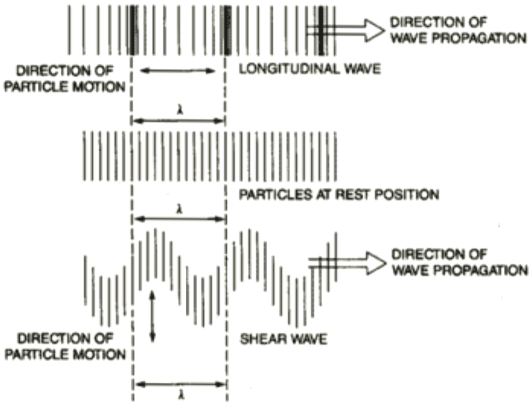

Figure 2.1: Pressure (P) waves (or longitudinal waves) and shear (S) (vertical) waves motion

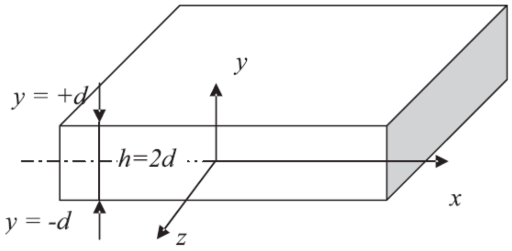

Figure 2.2: The setup plate considered to derive the Lamb waves solutions: an infinite plate along the direction x and y, with a $2d$ thickness (see [7]).

as:

$$\mathbf{u} = \nabla\Phi + \nabla \times \mathbf{H} \tag{2.2}$$

where Φ is the scalar potential and $\mathbf{H}$ the vector one.

The Eq. (2.2) re-written in terms of the potentials, provides:

$$\nabla^2\Phi = \frac{1}{c_p^2}\frac{\partial^2\Phi}{\partial t^2}\ ,\ \nabla^2\mathbf{H} = \frac{1}{c_S^2}\frac{\partial^2\mathbf{H}}{\partial t^2}\ ,\ \nabla\cdot\mathbf{H} = 0 \tag{2.3}$$

where $\mathrm{c}_\mathrm{p}^2 = (\lambda + 2\mu)/\rho$ and $\mathrm{c}_\mathrm{s}^2 = \mu/\rho$. We seek the potential solutions in the following form:

$$\begin{aligned} \Phi &= f(y)e^{j(kx-\omega t)} \\ \mathbf{H} &= (h_x(y)\mathbf{i} + h_y(y)\mathbf{j} + h_z(y)\mathbf{k})e^{j(kx-\omega t)} \end{aligned} \tag{2.4}$$

Note that the x axis corresponds to the propagation direction, in a thin-plate as in Fig. (2.2). Furthermore, a plain strain condition (z-invariant) is assumed. Therefore, the Eqs. (2.3) become:

$$\begin{aligned} f'' - k^2 f &= -\omega^2 f/c_p^2 \\ h_x'' - k^2 h_x &= -\omega^2 h_x/c_s^2 \\ h_y'' - k^2 h_y &= -\omega^2 h_y/c_s^2 \\ h_z'' - k^2 h_z &= -\omega^2 h_z/c_s^2 \end{aligned} \tag{2.5}$$

where $c_p^2 = (\lambda + 2\mu)/\rho$ and $c_s^2 = \mu/\rho$ are the pressure (longitudinal) and shear (transverse) wave speeds. Solution of Eqs. (2.5) is in the form:

$$\begin{aligned} \Phi &= (A\cos\alpha y + B\sin\alpha y)e^{i(kx-\omega t)} \\ H_x &= (C\cos\beta y + D\sin\beta y)e^{i(kx-\omega t)} \\ H_y &= (E\cos\beta y + F\sin\beta y)e^{i(kx-\omega t)} \\ H_z &= (G\cos\beta y + H\sin\beta y)e^{i(kx-\omega t)} \end{aligned} \tag{2.6}$$

where $\alpha^2 = (\omega^2/\mathrm{c}_\mathrm{p}^2) - k$ and $\beta^2 = (\omega^2/\mathrm{c}_\mathrm{s}^2) - k$. The constants $A - H$ can be found by applying the boundaries condition. It is assumed that the stress matrix has null terms (both normal and shear) on the top and bottom plate surfaces. Therefore, the following systems is obtained:

$$\begin{bmatrix} -c_3\sin\alpha d & c_4\sin\beta d & 0 & 0 & 0 & 0 & 0 & 0 & 0 \\ c_1\cos\alpha d & c_2\cos\beta d & 0 & 0 & 0 & 0 & 0 & 0 & 0 \\ 0 & 0 & c_1\sin\alpha d & -c_2\sin\beta d & 0 & 0 & 0 & 0 & 0 \\ 0 & 0 & c_3\cos\alpha d & c_4\cos\beta d & 0 & 0 & 0 & 0 & 0 \\ 0 & 0 & 0 & 0 & 0 & -c_5\sin\beta d & \beta^2\sin\beta d & 0 & 0 \\ 0 & 0 & 0 & 0 & 0 & -\beta\sin\beta d & jk\sin\beta d & 0 & 0 \\ 0 & 0 & 0 & 0 & 0 & 0 & 0 & \beta^2\cos\beta d & c_5\cos\beta d \\ 0 & 0 & 0 & 0 & 0 & 0 & 0 & jk\cos\beta d & \beta\cos\beta d \end{bmatrix} \begin{bmatrix} A \\ H \\ B \\ G \\ E \\ D \\ C \\ F \end{bmatrix} = 0 \tag{2.7}$$

with $c_1 = (\lambda + 2\mu)\alpha^2 + \lambda k^2, c_2 = 2j\mu k\beta, c_3 = 2jk\alpha, c_4 = k^2 - -\beta^2, c_5 = ik\beta.$

The system of Eqs. (2.7) admits a non trivial solution if and only if the determinant of coefficients matrix is equal to 0. It provides the characteristic

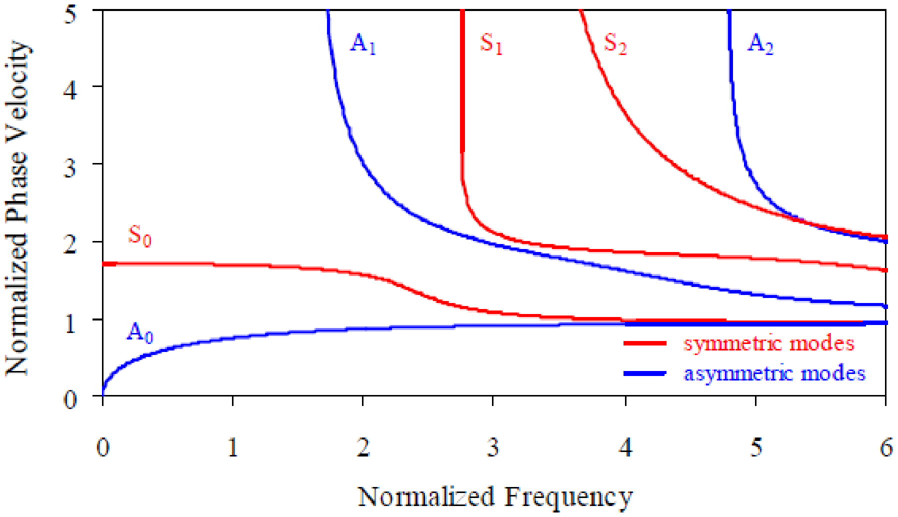

(a)

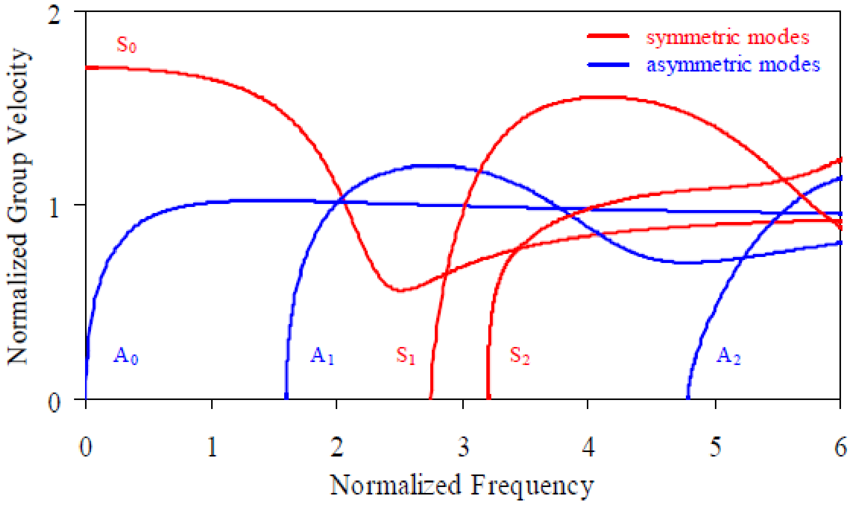

(b)

Figure 2.3: Lamb waves dispersion curves: (a) normalized phase velocities (c_p/c_s) as function of the normalized frequency-thickness product $(2\pi f 2d/c_s)$; (b) normalized group velocities (c_g/c_s) as function of the normalized frequency-thickness product (steel,$c_s = 3141[m/s]$).

equation. By observing the coefficients matrix of system (2.7), we note that it can be expressed as a product of four determinants of four smaller matrices related to the pairs (A,H), (B,G), (E,D) e (C,F). The first two pairs are related to the symmetric and anti-symmetric Lamb waves w.r.t. the mid-plane. The other ones are, again related to symmetric and anti-symmetric waves, which are Shear Horizontal (SH) waves. Therefore, four constitutive equations are provided. The first two ones, corresponding to the Lamb waves, are known as Rayleigh-Lamb's equations. These implicit transcendental equations can be solved numerically to determine the permissible guided waves solutions. The solutions of the characteristic equation determine a countable infinity of wave-number functions $k_n(\omega)$ and hence the wave phase and group velocities. The last two ones defines the, so called, dispersion curves of the Lamb waves. The dispersion trends as function of the frequency-thickness product, both normalized on the velocity c_s, are illustrated in Fig. (2.3). At lower frequency-thickness products, only two Lamb wave types exist: S_0, which is a symmetrical Lamb wave resembling the longitudinal waves, and A_0, which is an anti-symmetric Lamb wave resembling the flexural (or vertical Shear) waves.

2.1.1 Sensing Lamb waves via piezo-sensors

In this section the equations which describe the sensing of Lamb guided waves via a piezoelectric load are provided. Because, in the following chapters, they will be used extensively in order to design piezo-transducers both for the passive and active monitoring, their derivation is here given by following the work [2] of Senesi and Ruzzene. The case of a piezoelectric sensor arbitrarily shaped used in passive way is considered. However, the results can be extended to the case of transducer used in active way, on the basis of acoustic reciprocity principles.

Electric charge vector computation via the piezoelectric constitutive equations

Let's consider a mechanical structure (a thin plate), with the surface area Ω, and a bonded piezo-sensor with a domain Ω_P and thickness t_P. The reference system used for the analysis is located at the mid-surface of the structure, with x_1, x_2

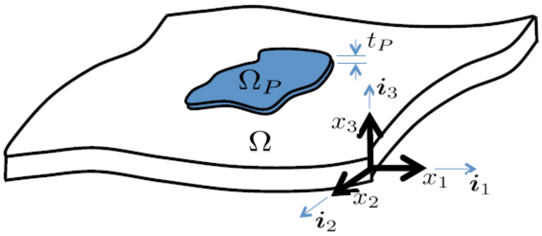

Figure 2.4: A (thin) plate with a piezo-sensor arbitrarily shaped, bonded on the top surface.

coordinates which define the structure plane. The considered system is illustrated in Fig. (2.4)

The constitutive equations of a piezoelectric sensor are given by:

$$\begin{cases} \sigma = \mathbf{C}^E \varepsilon - \mathbf{e}^T \mathbf{E} \\ \mathbf{D} = \mathbf{e}^\sigma \varepsilon + \varepsilon^\varepsilon \mathbf{E} \end{cases} \tag{2.8}$$

where

$$\begin{aligned} \sigma &= \left[\sigma_{11}, \sigma_{22}, \sigma_{33}, \tau_{13}, \tau_{23}, \tau_{12}\right]^T \\ \varepsilon &= \left[\varepsilon_{11}, \varepsilon_{22}, \varepsilon_{33}, \gamma_{13}, \gamma_{23}, \gamma_{12}\right]^T \end{aligned} \tag{2.9}$$

are respectively the mechanical stress and strain vectors. **D** and **E** are respectively the electric charge and the electric field vectors. Also, $\mathbf{e}^\sigma$ is the piezo-coupling matrix evaluated at constant stress, ε^ε is the permettivity matrix at constant strain and, finally, $\mathbf{C}^E$ is the stiffness matrix at constant electric field. In order to extend the validity of Eq. (2.8) from the piezo-domain Ω_P to the entire Ω plate domain, it is convenient to define a function $\phi(\mathbf{x})$ as:

$$\phi(\mathbf{x}) = \begin{cases} 1, & if \;\; \mathbf{x} \in \Omega_P \\ 0, & if \;\; \mathbf{x} \in \Omega - \Omega_P \end{cases} . \tag{2.10}$$

Without lack of generality, let's suppose that a single piezo-patch is characterized by a single polarization, $\psi(\mathbf{x}) = 1$. Particularly important is the second of Eq. (2.8), when an incoming wave is detected by a sensor. In order to derive a simple model the following two assumptions are made:

- the polaritazion is "through-the-thickness". Therefore $D_1 = D_2 = 0$.
- the sensor is assumed in a state of plain strain, i.e. the strain w.r.t. the

x_3-coordinate is negligible. Therefore, $[\varepsilon_{33}, \gamma_{13}, \gamma_{23}] \approx [0, 0, 0]$ and the strain vector is reduced to $\varepsilon = [\varepsilon_{11}, \varepsilon_{22}, \gamma_{12}]^T$.

The second of Eq. (2.8) is, then, re-writable as:

$$D_3 = \phi(\mathbf{x})\mathbf{b}^T\mathbf{D} = \phi(\mathbf{x})\mathbf{b}^T\left[\mathbf{e}^{\sigma}\varepsilon + \varepsilon^{\varepsilon}\mathbf{E}\right] \tag{2.11}$$

where $\mathbf{b} = [0, 0, 1]^T$. Now, let's consider the charge induced by the strain variation. The D_3 component becomes:

$$D_3 = \phi(\mathbf{x})\mathbf{b}^T\left[\mathbf{d}^{\sigma}\mathbf{C}^{E}\varepsilon + \left(\varepsilon^{\sigma} - \mathbf{d}^{\sigma}\mathbf{C}^{E}\mathbf{d}^{\sigma^T}\right)\mathbf{E}\right] \tag{2.12}$$

In the next subsection we will evaluate the electric field variation, in the form of measured voltage variation, for a mechanical strain ϵ variation.

Measured voltage in the Lamb waves piezo-sensing

In sensing mode, namely when a voltage is measured, the total charge within the piezo-volume is zero (whereas the charge induced on the top and bottom piezo-electrodes, supports the electric field). To proceed, let's model the piezo-load as a ideal capacitor, namely let's assume $E_1 = E_2 = 0$ and the voltage which varies linearly across the thickness (t_p):

$$\mathbf{E} = \frac{V}{t_p}\mathbf{b} \tag{2.13}$$

By multiplying the Eq. (2.12) for the unit vector $\mathbf{i}_3$ and integrating within the entire volume of the piezo-material, the left-side term provides 0 (null charge), via the 1^{st} Maxwell equation, $\nabla \cdot \mathbf{D} = \rho$. Then, the integrated right-side term provides a surface integral (for the divergence theorem). By using Eq. (2.13) and the integrated Eq. (2.12), the following equation for the measured voltage V is found:

$$V = \frac{t_p}{A_P\left[\mathbf{b}^T\left(\varepsilon^{\sigma} - \mathbf{d}^{\sigma}\mathbf{C}^{E}\mathbf{d}^{\sigma^T}\right)\mathbf{b}\right]}\mathbf{b}^T\mathbf{d}^{\sigma}\mathbf{C}^{E}\int\limits_{\Omega}\varepsilon\phi(\mathbf{x})d\mathbf{x} \tag{2.14}$$

where $A_P = \int\limits_{\Omega}\phi(\mathbf{x})d\mathbf{x}$ is the area of the top or bottom piezo-patch.

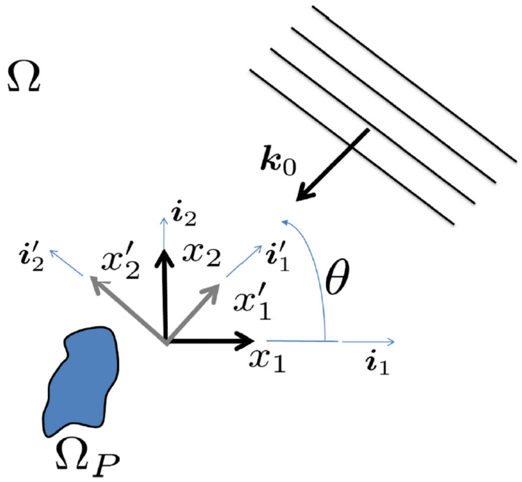

Figure 2.5: An illustration of a Guided wave impinging on a piezo-patch at direction $\mathbf{i'}_1$ (see [2]).

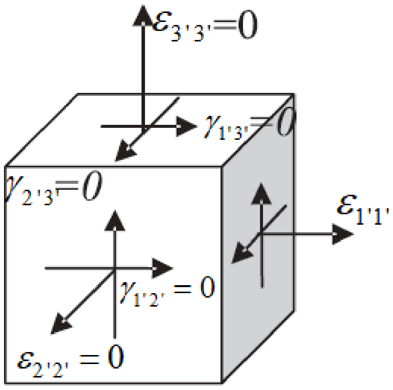

Figure 2.6: An infinitesimal volume extracted from the plate and the strain components in the reference systems $[\mathbf{i'}_1, \mathbf{i'}_2, \mathbf{i'}_3]$.

The Eq. (2.14) can be evaluated in the presence of a plane wave propagating in the plane of the structure at frequency ω. The out-of-plane displacement can in general expressed as:

$$\mathbf{u}(\mathbf{x}, \omega) = \mathbf{U}_0(\omega) e^{-j\mathbf{k}_0(\omega)\cdot\mathbf{x}} \tag{2.15}$$

where $\mathbf{U}_0(\omega)$ denotes the amplitude and the polarization of the wave at the considered frequency, and $\mathbf{k}_0(\omega) = k_0(\omega)\mathbf{i'}_1 = k_0(\omega)\left(\cos\theta\mathbf{i}_1 + \sin\theta\mathbf{i}_2\right)$ is the considered wave vector defining plane wave propagation at an angle θ. Assuming that the considered wave is characterized by a displacement field such that $\mathbf{u}(\mathbf{x}, \omega) \cdot \mathbf{i'}_2 = 0$ (i.e. there aren't shear components: $\varepsilon_{2'2'} = 0$, and $\gamma_{1'2'} = 0$), the only strain component relevant to the surface mounted sensor is given by:

$$\varepsilon_{1'1'} = \frac{du'_1}{dx'_1} = jU_{1'_0}(\omega)k_0(\omega)e^{-jk_0(\omega)x'} \tag{2.16}$$

According to the assumed model, the strain components of an infinitesimal volume extracted from the plate is illustrated in Fig. (2.6).

Observe that neglect the strain component $\varepsilon_{2'2'}$ [25] is legitimate when $\lambda/d >> 1$, being λ the wavelength and d the plate thickness. Therefore, in the following chapters where the piezo-response model being derived will use to do sensors design, only simulation setups which satisfy the last condition will be considered.

The plane strain of Eq. (2.14) can be written as:

$$\varepsilon = \varepsilon_{1'1'}\mathbf{r}(\theta) \tag{2.17}$$

where $\mathbf{r}(\theta) = \left[\cos^2\theta, \sin^2\theta, 0\right]$. Substituing Eqs. (2.17) and (2.16) into Eq. (2.14), the voltage $V(\omega)$ becomes:

$$V_P(\omega) = jU_{1'_0}(\omega)k_0(\omega)H_P(\theta)D_P(\omega, \theta) \tag{2.18}$$

where:

$$H_P(\theta) = \frac{t_p\mathbf{b}^T\mathbf{d}^\sigma\mathbf{C}^E\mathbf{r}(\theta)}{A_P\left[\mathbf{b}^T\left(\varepsilon^\sigma - \mathbf{d}^\sigma\mathbf{C}^E\mathbf{d}^{\sigma^T}\right)\mathbf{b}\right]} \tag{2.19}$$

and

$$D_P(k_0(\omega),\theta) = \int\limits_{\Omega_P} e^{-jk_0(\omega)(x_1\cos\theta + x_2\sin\theta)}\phi_P(\mathbf{x})d\mathbf{x} \tag{2.20}$$

define two different contributions to the frequency piezo-response. The first quantity. $H_P(\theta)$, is related only to the piezo-material properties and involves directional component only in the case of non-isotropic properties of the patch. For the case of monolithic PZT patch, for example, the quantity H_P is constant and no directionality is introduced.

Vice versa, the quantity D_P describes the effect of the piezo-load distribution, via the function $\phi_P(\mathbf{x})$ related to the sensor shape. Therefore, tha last one is referred to as *shape function*, instead the function D_P determines the directionality properties and allows to select specific piezo-distribution to achieve the desired sensor directivity properties. Therefore, it is referred to as *Directivity function.*

Noteworthy, the integration limits of Eq. (2.20) can be extended to infinity without affecting the value of the integral. Therefore, the Directivity function can be seen as the 2D-Fourier Transform (2D-FT) at angle θ. The last observation will be used in Ch. (3) to design opportunely the sensors shape to better localize impacts/defects in presence of noise. Furthermore, by rewriting the wave-vector in the form $\mathbf{k}_0(\omega) = k_0(\omega)\left(\cos\theta\mathbf{i}_1 + \sin\theta\mathbf{i}_2\right) = k_1\mathbf{i}_1 + k_2\mathbf{i}_2$, the Eq. (2.20) can be written as:

$$D_P(\mathbf{k}_0(\omega)) = \int\limits_{-\infty}^{\infty}\int\limits_{-\infty}^{\infty} e^{-j\mathbf{k}_0(\omega)\cdot\mathbf{x}}\phi_P(\mathbf{x})d\mathbf{x} \tag{2.21}$$

In this way, the Directivity is configured ad the 2D-FT of the shape function, in the variables k_1, k_2. The Eq. (2.21) suggests the possibility of evaluating the sensor directivity through Fast Fourier Transform (FFT) efficient algorithms in case of complex material distributions. At the same time, imposed a Directivity function in the k_1, k_2 plane, it is possible to obtain the correspondent sensor geometry by inverting the Eq. (2.21), i.e.:

$$\phi_P(\mathbf{x}) = 2D - F^{-1}\left\{D_P(\mathbf{k}_0(\omega))\right\} \tag{2.22}$$

where $2D - F^{-1}$ denotes the Inverse bi-dimensional FT. The Eq. (2.22) will be used in Chs. (5) and (6) to design transducers, respectively, suitable for the passive monitoring in reverberant environments and for the active monitoring to inspect a structure.

2.1.2 Green's Functions formalism for LW piezo-response

In order to numerically assess the sensors/transducers design procedures which will be defined in the following chapters, as well as the defects/impacts localization performance, the Lamb waves and the piezo-responses will be simulated using a Green's functions (GFs) formalism, adopted in [26, 27]. In sensing mode, the acquired signal is estimated as:

$$u_p(\omega) = \sum_{p=1}^{N_p} w_p(\mathbf{x}_p) u_{LW}(\mathbf{x}_p, \omega) \tag{2.23}$$

where $w_p(\mathbf{x}_p)$ takes into account, for each discrete point $\mathbf{x}_p$ belonging to the sensor, the polarity and the amplitude which can be imposed in acquisition phase. The wave-field $u_{LW}(\mathbf{x}_p, \omega)$ is computed as:

$$u_{LW}(\mathbf{x}_p, \omega) = g_0(\omega) \sum_{a=1}^{N_a} w_a(\mathbf{x}_a) G(\mathbf{x}_p, \mathbf{x}_a, \omega) \tag{2.24}$$

where, again, $w_a(\mathbf{x}_a)$ are weights to consider a different amplitude and polarization applied to a point source at location $\mathbf{x}_a$. $g_0(\omega)$ is the spectrum of the signal due, for example, to an impact or a defect growth. The Green's function G, defining the response to a unit source is expressed as:

$$G(\mathbf{x}_p, \mathbf{x}_a, \omega) = j\pi^2 H_0^{(1)}(k_0(\omega) R_{a-p}) \tag{2.25}$$

where, $H_0^{(1)}$ is the Hankel function of the first kind and order 0, and $R_{a-p} = |\mathbf{x}_p - \mathbf{x}_a|$ is the distance from the sensor points $\mathbf{x}_p$ and the location of the $a-th$ source point $\mathbf{x}_a$. Dispersion is included by taking into account the frequency dependence of the wavenumber, via the function $k_0(\omega)$ in (2.25), based on the dispersion relation for the considered propagation mode.

Observe that the GFs formalism can be used also when a transducer is used in a pulse-echo operation. The actuation phase can be simulated by impacting the excitation signal with a spectrum $g_0(\omega)$, at different plate location $\mathbf{x}_a$, namely at different angles and distances, and computing the corresponding piezo-responses via the Eq. (2.23). Then, the acquired signal can be re-impacted at the same location to simulate the sensing phase. The last procedure is allowed thanks to the acoustic reciprocity principle.

Chapter 3

Sensors design for noisy environments

3.1 Shaped Sensor arrays

Disclaimer: *The content of this Section is based upon the research work [28]: Marco Dibiase and Luca De Marchi. "Clusters of Shaped Ultrasonic Transducers for Lamb Waves' DoA Estimation". In: Applied Sciences 10.22 (2020), p. 8150.*

As previusly seen in Section (1.2.3), arrays of closely located sensors, able to estimate the DoA of guided waves, are very suitable for embedded monitoring systems for impacts/damages localization, increasingly requested for many applications, such as the aeronautical and aerospace ones.

Thanks to the low requested computational cost, passive sensors arrays systems allow to satisfy the constraints of the previously mentioned application fields, such as the capability to perform in-site signal processing, via wirelessly connected electronic devices, characterized by low power consumption and the consequent reduced cabling and weight.

Although simple clusters of disk-sensors have already investigated ([18, 21]) for impacts localization, both in isotropic and anisotropic structures, it is well-known that this task is quite complex due to the detrimental effect of noise. Typical noisy physical sources are given by: structural vibration (e.g., due to turbulence on an aircraft), scattered wavefield, interference of several edge reflections produced by

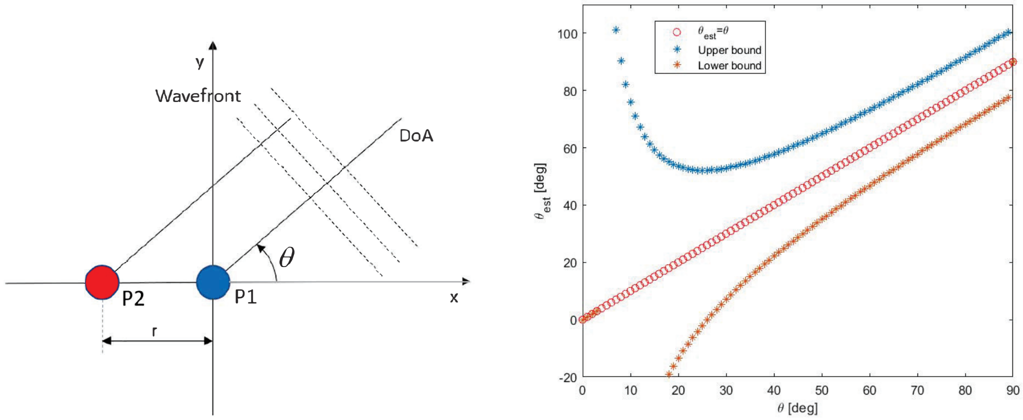

(a) (b)

Figure 3.1: (a) A basic cluster of two circular piezo-sensors spaced apart by a distance r; (b) upper and lower error bounds of the cluster illustrated in the Fig. (a). The error bounds were computed as the uncertainty $\sigma_{\widehat{\theta}}$, considering v = 2000[m/s] and the $\sigma_{\widehat{d}_{21}}$ equal to $1[us]$.

different acoustic events, noisy acquisition channels, or noisy electronic devices. When the noise level is comparable to the useful signal peak, given by the AEs due to an impact or a defect growth to be located, even if robust techniques for the time-delay estimation are used (i.e. Generalized Correlation methods [29]), the DoA estimation could fail.

Our aim is to tackle the noise issue at the sensors design level. In particular, sensors shaping procedures will be exploited to increase the DoA estimation performance. To this aim, the problem statement will be addressed with a 2-step procedure: firstly, two and three-sensors cluster configurations will be analysed to show how we can improve the DoA estimation performance. Then, a sensor shaping procedure, suitable for GWs detection, will be illustrated. Finally, the problem will be formalized in order to find the optimal shapes, for a cluster composed by three sensors and considering the wave velocity unknown.

Let us suppose to consider a cluster of two isotropic sensors, $P1$ and $P2$, ideally point-like. The impact/defect distance is assumed to be sufficiently large, so that the generated AEs wave-fronts can be considered locally planar at the cluster location (i.e. the cluster is in the Fraunhofer zone). The relationship between the DToA of wave-fronts between two sensors (see Fig. (3.1)(a)), d_{21}, and the DoA, θ, is given by:

$$d_{21} = \frac{r\cos\theta}{v} \tag{3.1}$$

where r is the distance between $P1$ and $P2$ and v is the wave velocity. Therefore, by estimating the DToA can be estimated the angle θ. The Minimum Mean Square Error (MMSE) is given by the following expression:

$$\widehat{\theta} = \arccos\left(\frac{v\widehat{d}_{21}}{r}\right) \tag{3.2}$$

where the hat symbol over an argument, "$\widehat{\cdot}$", indicates an estimator, namely a random variable.

The Propagation of Uncertainty theory [30] provides the variance of a quantity which is a function f of quantities directly measurable. In our case, the quantity is $\widehat{\theta}$, with variance $\sigma^2_{\widehat{\theta}}$, whereas the DToAs $\widehat{d}_{21}, \widehat{d}_{31}, ..., \widehat{d}_{(N-1)1}$ are the quantities directly measurable. According to the theory, $\sigma^2_{\widehat{\theta}}$ is given by:

$$\sigma^2_{\widehat{\theta}} = \left(\frac{\partial f}{\partial \widehat{d}_{21}}\right)^2 \sigma^2_{\widehat{d}_{21}} + \left(\frac{\partial f}{\partial \widehat{d}_{31}}\right)^2 \sigma^2_{\widehat{d}_{31}} + ... + \left(\frac{\partial f}{\partial \widehat{d}_{(N-1)1}}\right)^2 \sigma^2_{\widehat{d}_{(N-1)1}} \tag{3.3}$$

where $\sigma^2_{\widehat{d}_{j1}}$ are the variances of the quantities $\widehat{d}_{j1}$. Observe that Eq. (3.3) assumes the covariance elements equal to 0 and the first derivates are evaluated at the mean value of all components of vector $\left[\widehat{d}_{21}, \widehat{d}_{31}, ..., \widehat{d}_{(N-1)1}\right]$.

Eq. (3.3) applied to the function (3.2) reveals that the error can be very large for low values of θ, as shown in Fig. (3.1)(b). This is due to the non-linear characteristics of the arccos function. To counteract this problem, a sensor shaping procedure can be applied in order to achieve a linear dependence between the DToA and the DoA (see Fig. (3.2)(a)), so that:

$$d_{21} = \frac{\alpha\theta + \rho_0}{v} = \frac{\rho_{21}(\theta)}{v} \tag{3.4}$$

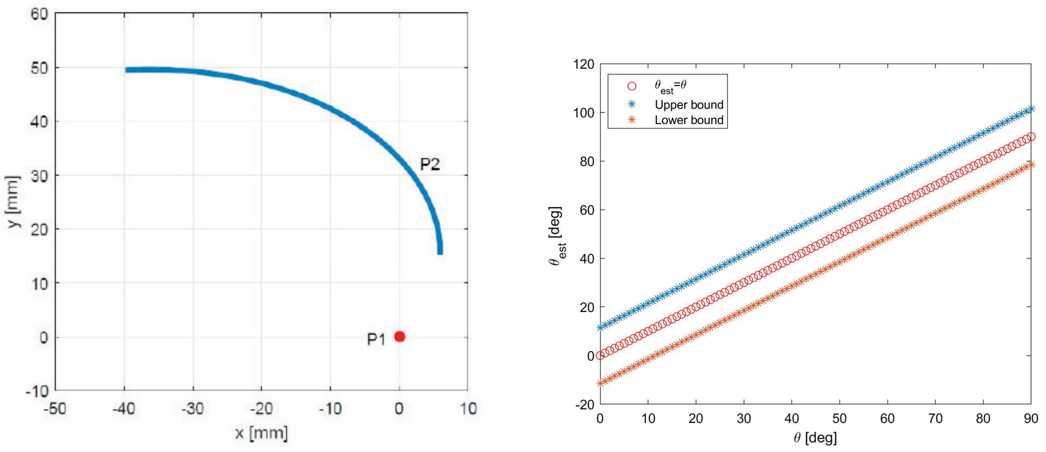

(a) (b)

Figure 3.2: (a) A cluster of two sensors with P2 shaped so that a linear relation between the DToA and DoA is geometrically achieved; (b) upper and lower error bounds of the cluster of Fig. (a) (considering $\alpha = 2[\text{cm}]/90°$, $\rho_0 = 0$ in the Eq. (3.4)). The error bounds were computed as the uncertainty $\sigma_{\widehat{\theta}}$, considering $\text{v} = 2000[\text{m/s}]$ and the $\sigma_{\widehat{d}_{21}}$ equal to $1[us]$.

where the parameter α value can be chosen by the designer. Thanks to the new linear relation, the worst-case error is constant over the considered range of angles and considerably lower than the maximum error achieved by using two conventional disks (Fig. (3.2)(b)). It is worth noting that the uncertainty $\sigma_{\widehat{\theta}}$ is inversely proportional to the selected value of α. For this reason, the larger α the lower is the error in the DoA estimation. However there is a trade off involved in the selection of α because, the larger is α, the larger is the maximum value of the DToA, which defines the time-window length of the acquired signal (i.e the information to be stored and processed). Furthermore, when GWs are acquired, higher is the maximum DToA value, higher is the dispersion effect between two sensors. It is also worth noting that a cluster composed by two sensors can be used to estimate θ only if the actual wave velocity v is assumed to be known. Therefore, if the velocity is not known a priori, a third sensor P3 is needed to estimate the DoA. In the work [28], a third sensor was added to establish a constant reference to estimate the wave velocity, i.e.:

$$d_{31} = \frac{\rho_{31}}{v} = \frac{\rho_{3C}}{v} \tag{3.5}$$

where ρ_{3C} is a constant. The relation between the DToAs ratio and the DoA is given by:

$$\frac{d_{21}}{d_{31}} = \frac{\alpha\theta + \rho_0}{\rho_{3C}} \tag{3.6}$$

Therefore, the MMSE estimator $\widehat{\theta}$ can be obtained by inverting the last one w.r.t. the ratio of the estimators $\widehat{d}_{21}, \widehat{d}_{31}$, which are random variables. Observe that in order to estimate the DoA, the knowledge of the wave propagation velocity is not necessary, because such quantity does not appear in the Eq. (3.6).

However, the third sensor P3 introduces an additional uncertainty in the DoA estimation due to $\sigma^2_{\widehat{d}_{31}}$. The values of the parameters α, ρ_0 and ρ_{3C} can be used to minimize the uncertainty in DoA estimation and by limiting the maximum value of $|d_{21}(\theta)|$ and $|d_{31}(\theta)|$. The last ones can be set to be equal to r/v, where r is the maximum distance for a disks-cluster. In this way, the performance comparison between a disks-cluster and a shaped sensors-cluster are provided with the same time-window lengths to be processed (i.e. same computational cost) and the same dispersion effect between sensors. By considering a monitored area of 90°, with the angles work-range given by [-45°,45°], the optimum parameters values are given by:

$$\alpha = r/45[\text{deg}];\ \rho_0 = 0;\ \rho_{3C} = r \tag{3.7}$$

By using the Eq. (3.3), the estimation performance comparison in terms of standard deviation, $\sqrt{\sigma^2_{\widehat{\theta}}}$, between a 3-disks-cluster and the considered 3-shaped sensors-cluster provides a theoretical average uncertainty reduction of 11% when the shaped sensors are used (see the Fig. (3.3)).

From the previous discussion, two important points are to be noticed:

- The transducer shaping procedure aim is to realize a desired function $d_{j1}(\theta)$ between the signals of two sensors. This requires that the two sensors have the same frequency response, apart from a phase shift equal to the desired time-delay function, when GWs impinging on the sensors. To achieve this goal, it must be considered that shaped sensors are generally characterized by

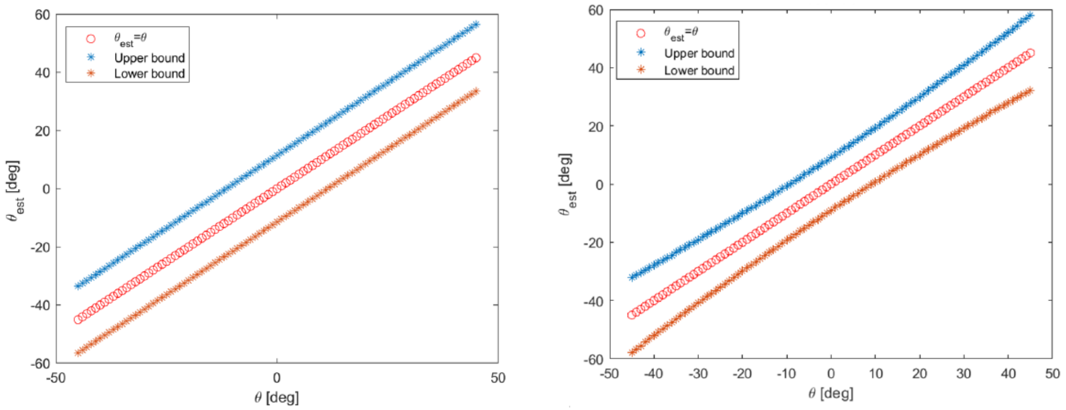

(a) (b)

Figure 3.3: (a) Upper and lower error bounds of a cluster of 3-disks sensors spaced apart by a distance r; (b) Upper and lower error bounds of the cluster of shaped sensors according to the Eqs. (3.4) and (3.5) with the parameters values (3.7). The error bounds were computed as the uncertainty $\sigma_{\widehat{\theta}}$, considering v $=$ 2000[m/s] and the $\sigma_{\widehat{d}_{21}}$ equal to $1[us]$.

an angle-dependent wavenumber tuning effect [31], i.e. the frequency response of the transducer depends on the direction of propagation of the incident wave. In turn, this effect may hamper the possibility to extract the time-delays via optimal estimators, namely generalized cross-correlation procedures [29], in which the response, among different transducers, is assumed to be equal unless a time-shift.

- The previous considered case of three shaped sensors cluster design was addressed by selecting suitable functions $d_{j1}(\theta)$ one by one. Therefore, a question arises: can we do better? In order to answer this question, an optimality criterion has to be defined to find the two functions $d_{j1}(\theta)$, with $j = 2, 3$, for a 3-sensors cluster, able to minimize the θ estimation lower bound. Furthermore, after defining a suitable cost function to be minimized, it is requested to find a solving technique. The case of an array composed by a generic number of sensors M, will be discussed in Ch. (4).

In the following two Sections, the previous issues will be respectively addressed.

3.1.1 Radon Transform (RT) shaping procedure

Disclaimer: *The content of this Section is based upon the research work [28]: Marco Dibiase and Luca De Marchi. "Clusters of Shaped Ultrasonic Transducers for Lamb Waves' DoA Estimation". In: Applied Sciences 10.22 (2020), p. 8150.*

Aim of this Section is to find a design procedure, so that, given the frequency response of a disk sensor $V_{P1}(\omega, \theta)$, the frequency response, $V_{P2}(\omega, \theta)$, of a shaped sensor P2, is linked to the previous one, in the following form:

$$V_{P2}(\omega, \theta) = V_{P1}(\omega) \exp(-jk_0(\omega)\rho_{21}(\theta)) \tag{3.8}$$

where $\rho_{21}(\theta)$, defined as the Difference in Distance of Propagation (DDoP), is related related to the DToA $d_{21}(\theta)$ via $d_{21}(\theta) = \rho_{21}(\theta)/v$. The term $k_0(\omega)$ is the wave-vector frequency relationship of a 0 order Lamb waves mode (or, more generally, any wave Lamb wave mode).

If the acquired signal is narrow-band, $k_0(\omega)$ can be approximated via a Taylor expansion, around the central frequency ω_c to the first order:

$$\begin{aligned} k_0(\omega) &\simeq k_0(\omega_c) + (\omega - \omega_c){k_0}'(\omega_c) \\ &= v_p(\omega_c)\omega_c - \omega_c {k_0}'(\omega_c) + \omega {k_0}'(\omega_c) \\ &= v_p(\omega_c)\omega_c - \omega_c {k_0}'(\omega_c) + \tfrac{\omega}{v_g(\omega_c)} \end{aligned} \tag{3.9}$$

Therefore, for a narrow-band signal, the expansion (3.9) well-approximates the curve $k_0(\omega)$ around the central (angular) frequency ω_c, and a phase shift in the frequency ω, equal to $d_{21}(\theta) = \rho_{21}(\theta)/v_g(\omega_c)$ is achieved and the wave velocity can be considered approximately constant. Noteworthy, closer the sensors are, smaller are the phase shift differences of each spectral components among all sensors, when second order terms arise in the Taylor's expansion (3.9). Observe that the assumption of a narrow-band signal can not always be satisfied. Indeed, in the most general case, AEs due to impacts or to defects growth can be wide-band. However, the acquired signal can be always decomposed, via a digital filter bank, in multiple narrow-band signals, within the bandwidth defined by $f_s/2$. Therefore, cross-correlation procedures can be computed many times to have a more robust time-delay estimation.

Noteworthy, the decomposition of the acquired signal in multiple narrow-band signals, can be detrimental for low Signal to Noise Ratio (SNR) values. In these contexts, efficient dispersion compensation procedures can be applied [32], but this requires the knowledge of the dispersion curves. However, if the distances between sensors are small, the dispersion effects are negligible in terms of envelope distortion. This property derives by the energy distribution in the Frequency-Time (FrT) domain, which follows the curve $t = \rho_{21}(\theta)/v_g(\omega)$. For a small DDoP, $\rho_{21}(\theta)$, two curves related to two near sensors, differ slightly, then the wave packet profiles, defined by all spectral components at different time, are very similar. However, envelopes cross-correlation (CC) is less effective than applying the cross correlation on the RF signals and doesn't allow to use the signal phase for the Generalized CC (GCC) with phase transform (GCC-PHAT) [33, 34], a suitable procedure in reverberant scenarios.

In the following, we will consider only time-delay estimation strategies which don't require to known the wave velocity $v_g(\omega)$, namely strategies in which v_g can be considered nearly constant, in order to design arrays suitable for any structure, with no *a priori* material properties knowledge.

In order to impose the relationships (3.8) three key elements can be exploited:
a) The model of the frequency response of a sensor in the presence of a Lamb wave mode.
b) The Radon Transform (RT) and its inverse (IRT).
c) The Projection Slice Theorem.

The key point a) has already seen in the Section (2.1.1). It is important to highlight that the wavenumber tuning effect, which influences the frequency responses of shaped sensors, is mainly due to the Directivity function $D_P(k_0(\omega), \theta)$ which is configured as a 2D-FT at angle θ of the shape function, $\phi_P(\mathbf{x})$, that describes the piezo-load geometrical distribution.

Element b), i.e. the Radon Transform [35, 36], can be defined in different ways. Given a continuous function $g : D \subseteq \mathbb{R}^2 \to \mathbb{R}$, defined on a compact support, its Radon Transform $RT(p, \tau)$ is found by integrating the value of g along slanted lines. Considering the lines equation in the explicit form, via the slope p and the offset τ, the RT is defined as:

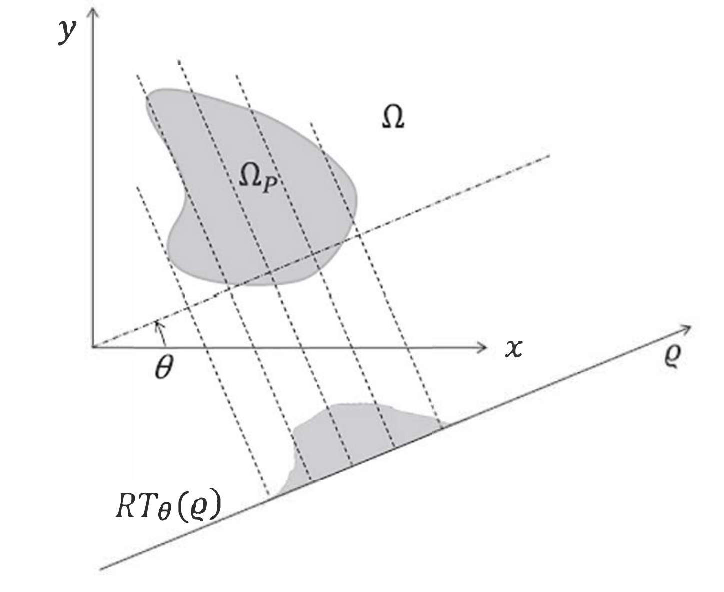

Figure 3.4: Representation of the Radon transform of the function $g(x, y)$ over the domain Ω_P.

$$RT(p,\tau) = \int_{-\infty}^{\infty} g(x, px + \tau)dx \tag{3.10}$$

By using the Dirac delta "function" $\delta(\cdot)$, the previous integral can be written as:

$$RT(p,\tau) = \int_{-\infty}^{\infty}\int_{-\infty}^{\infty} g(x,y)\delta(y - px - \tau)dxdy \tag{3.11}$$

Therefore, according to the definition, considering a fixed p slope value, the RT can be seen as a function of offset, τ, whose values are given by multiple integrals along lines of a set family, with the same slope p. Although the previous definition is very intuitive, another definition is used in many fields of science, e.g., tomography, astronomy and microscopy [35], where the transformed function $g(x, y)$ has no preferred orientation. In this case, and for our purpouse, it is more convenient to describe a line on its normal form:

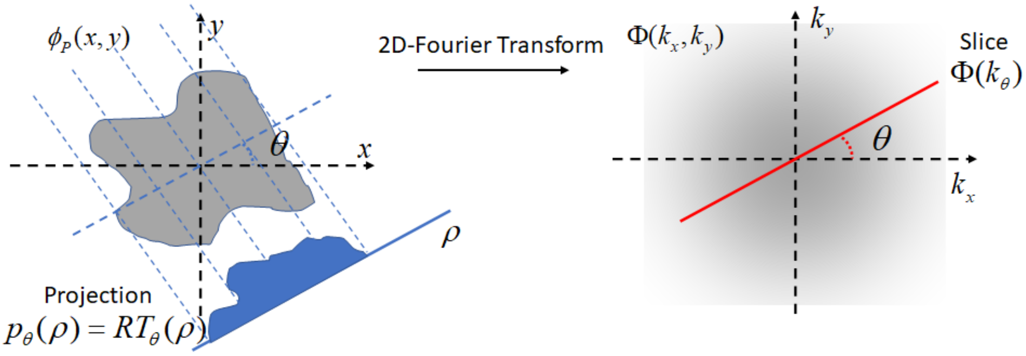

Figure 3.5: A graphical illustration of the Projection Slice Theorem. $\Phi(k_x, k_y)$ is the 2D-FT of $\phi(x, y)$. The projection given by the RT, $p_\theta(\rho)$, is given by multiple line-integrals along lines normal to θ direction. The slice $\Phi(k_\theta)$ on the 2D-Fourier plain is along the θ direction. The Projection Slice Theorem states that the slice $\Phi(k_\theta)$ is the 1D-FT of the projection $p_\theta(\rho)$.

$$\rho = x\cos\theta + y\sin\theta \tag{3.12}$$

where θ is the angle between the normal segment to the line, going through the reference system origin, whereas ρ is the length of the normal segment. By using the Eq. (3.12), the RT is given by:

$$RT_\theta(\rho)[g(x,y)] = \int\int g(x,y)\delta(\rho - x\cos\theta - y\sin\theta)dxdy \tag{3.13}$$

Again the RT consists of multiple integrals along lines shifted by ρ and normal to the direction θ. A graphic illustration is given in Fig. (3.4). It can be observed that the line-integrals are computed in the normal direction w.r.t. to the angle θ. This aspect will be useful for the key point c).

When a piezo-load is considered, described by a shape function $\phi_P(x, y)$, which is different to 0 over a Ω_P area, the "normal" RT is given by:

$$R_\theta(\rho)[\varphi(x,y)] = \int\int_{\Omega_P} \phi(x,y)\delta(\rho - x\cos\theta - y\sin\theta)dxdy \tag{3.14}$$

The RT admits inverse. It will be referred to as Inverse RT (IRT)

Finally (element c)), the Projection Slice Theorem [37] states that the bidimensional FT at the angle θ of a given function, is equal to the mono-dimensional FT of the Radon Transform of that function. A graphical illustration of the projection slice theorem in given in Fig. (3.5).

Therefore, the Directivity function, and, in turn, the frequency response, can simply be calculated as the monodimensional FT of the RT of the shape function and by evaluating into $k_0(\omega)$.

As a consequence, the desired time-delay $d_{21}(\theta) = \rho_{21}(\theta)/v$, i.e. the Eq. (3.8) in frequency, is obtained by imposing a suitable relation between the RT of a disk-sensor P1 and the RT of a shaped sensor P2:

$$RT_\theta(\rho)[\varphi_2] = RT_\theta(\rho - \rho_2(\theta))[\varphi_1] \tag{3.15}$$

In conclusion, the synthesis procedure of the shape function for a sensor P2, which realizes the desired DToA relation, can be summarized as follows: consider an isotropic circular reference sensor 1, then calculate its RT (constant over θ) and impose the RT of sensors P2 by using ((3.15)) with the desired $\rho_2(\theta)$ shift. As example, in Fig. (3.6)(a) is imposed a P2 sensor RT linearly shifted in θ w.r.t. the disk-RT, in the range [-45°,45°] (as the Eq. (3.4) and in the work [28]).

By inverting the RT, we obtain a shape function which is continuously modulated (Fig. (3.6)(b)). In order to obtain a step functions as in ((2.10)), a quantization procedure is imposed by setting all values greater than a certain threshold to 1 and the others to 0. In this way, the desired shape (step) function can be obtained (as illustrated in Fig. (3.6)(c)).

Fig. (3.6)(d) shows the actual RT (i.e. the RT computed by the post quantization shape function). It is worth noting that it differs from the imposed RT (subfigures (a)) due to the binary quantization procedure.

3.1.2 Average Variance and Calculus of Variations for the optimal shapes design

Disclaimer: *The content of this Section is based upon the research work: Marco Dibiase and Luca De Marchi. "An optimal shaped sensor array derivation". Submitted to Micromachines Journal (MDPI).*

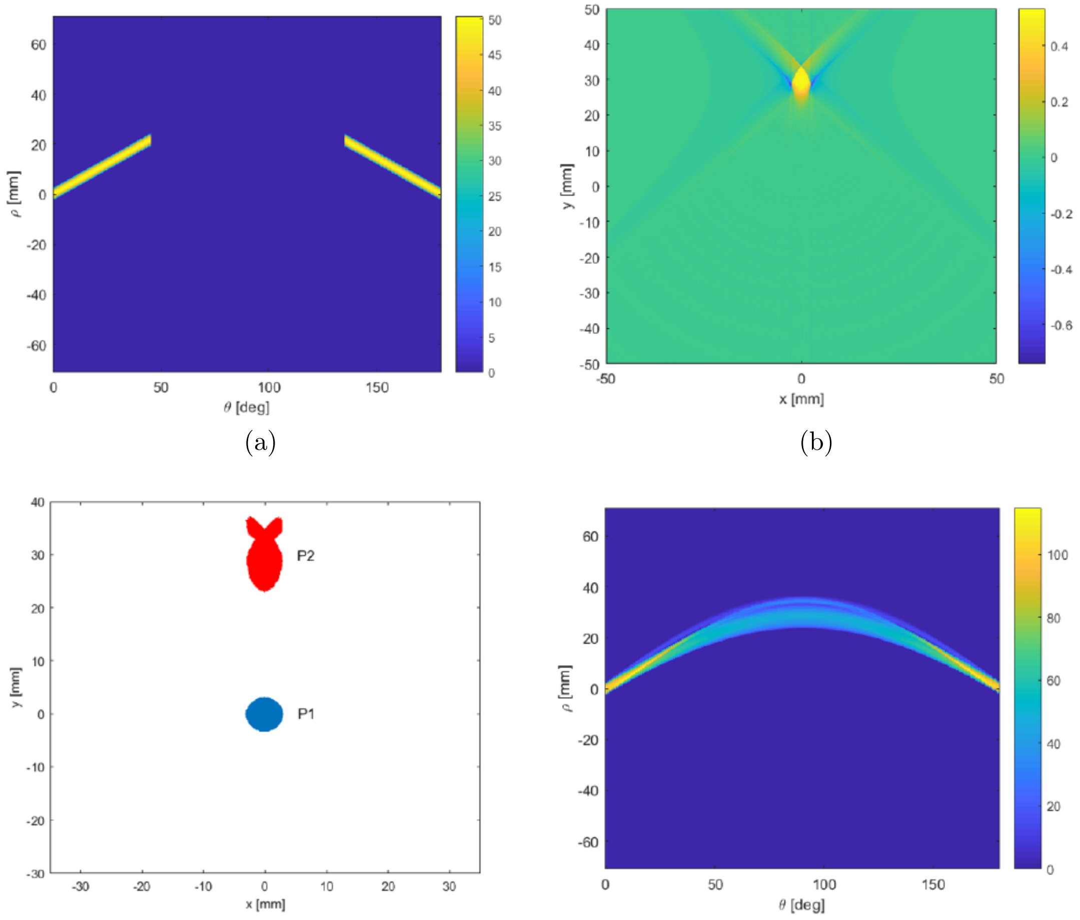

(a) (b)

(c) (d)

Figure 3.6: A graphical illustration of the re-shaping design procedure. (a) Imposed RT of sensor P2 (equal to disk-one in [-45°,45°], unless than a linear shift in θ; (b) IRT; (c) binary quantization of the IRT (P1 and P2 sensors); (d) actual RT (considering $d = 20[mm]$, Threshold values to binary quantization equal to 30% of maximum value of IRT).

In this Section, the problem to find the optimal arrangement and shapes of three sensors, composing an array, is addressed when the wave velocity is considered unknown. The last assumption allows to define the optimal sensor design, being agnostic on the structural material to be monitored. Furthermore, even if a design procedure can be specialised for a certain target material, it is worthy to note that the nominal wave-velocity can change due to temperature variations, tapered areas etc. which can lead to an accuracy loss in the DoA estimation. A more general problem statement for N-sensors-array will be considered in Chapter (4), in which some differences will be highlighted.

As a starting point, let us consider two arbitrary relationships between the DToAs (d_{21} and d_{31}) at a given wave direction of propagation θ:

$$d_{21}(\theta) = \frac{\rho_{21}(\theta)}{v} \ , \ d_{31}(\theta) = \frac{\rho_{31}(\theta)}{v} \tag{3.16}$$

where $\rho_{21}(\theta)$ and $\rho_{31}(\theta)$ are arbitrary functions and v is wave velocity[1]. Observe that the two functions $\rho_{21}(\theta)$ and $\rho_{31}(\theta)$, corresponding to a spatial-ρ shift in the RT domain, can be imposed via the procedure seen in the previous Section. The aim is thus to find the optimal estimator in the mandatory form:

$$\hat{\theta} = f\left(\frac{\hat{d}_{21}}{\hat{d}_{31}}\right) \tag{3.17}$$

which is necessary to estimate DoA θ without knowing the wave velocity v. When the measurements are affected by Additive Uncorrelated Gaussian Noise (AUGN), a cross-correlation procedure (see [19]) can be used to implement a Maximum Likelihood (ML) estimator approximation whose variance tends to the Cramér–Rao Lower Bound (CRLB) of the (uncorrelated) DToAs.

The optimal estimator, with estimation function of form ((3.17)), is the one that minimizes its variance, provided by the Theory of Uncertainty Propagation for measurements [30]. Neglecting the correlation between $\hat{d}_{21}, \hat{d}_{31}$, it can be written

---

[1] The wave velocity v can be approximately regarded as a constant parameter under the assumption of low dispersion.

as:

$$\begin{aligned}\mathrm{Var}(\hat{\theta}) &= e_{ms} = \mathrm{E}[\hat{\theta}^2] - \theta^2 = \\ &= \left(\frac{\partial f}{\partial \hat{d}_{21}}\right)^2 \Bigg|_{E[\hat{d}_{21}],E[\hat{d}_{31}]} \sigma^2_{\hat{d}_{21}} + \left(\frac{\partial f}{\partial \hat{d}_{31}}\right)^2 \Bigg|_{E[\hat{d}_{21}],E[\hat{d}_{31}]} \sigma^2_{\hat{d}_{31}}\end{aligned} \tag{3.18}$$

The variance value, $\mathrm{Var}(\hat{\theta})$, of worst case is given by:

$$\sigma^2_{\hat{\theta}-WorstCase} = \left(\left(\frac{\partial f}{\partial \hat{d}_{21}}\right)^2 + \left(\frac{\partial f}{\partial \hat{d}_{31}}\right)^2\right) \sigma^2_{d-Max} \tag{3.19}$$

where $\sigma^2_{d-Max} = \max[\sigma^2_{\hat{d}_{21}}, \sigma^2_{\hat{d}_{31}}]$. The aim is then to minimize ((3.19)) on average over all the expansion points $\mathrm{E}[\hat{d}_{21}] = d_{21}, \mathrm{E}[\hat{d}_{31}] = d_{31}$. Therefore we want to minimize the following integral:

$$J[f] = \frac{\sigma^2_{d-Max}}{\Omega} \int\int_{\Omega} \left(f^2_{d_{21}} + f^2_{d_{31}}\right) \mathrm{d}d_{21}\mathrm{d}d_{31} \tag{3.20}$$

where, to simplify the notation, $f_{d_{21}} = \frac{\partial f}{\partial d_{21}}, f_{d_{31}} = \frac{\partial f}{\partial d_{31}}$. The integral is computed over Ω, i.e. the variation range of $\mathrm{E}[\hat{d}_{21}], \mathrm{E}[\hat{d}_{31}]$. It can be observed that Eq. (3.20) is configured as a functional, $J[f]$ which can be minimize with the tools developed within the Calculus of Variations (CoV) theory, which is widely used in multiple Physics fields [38]: from classical Mechanics, with The Principle of Least Action, to Optics, with the Maupertuis's principle; from Quantum Mechanics, with Feynman integrals, to the advanced Physics of elementary particles interaction.

CoV allows to derive compact expressions, via the integrand function, namely the Lagrangian function. In our case, the Lagrangian function is simple expressed by $\sigma^2_{\hat{\theta}-WorstCase}$.

The CoV provides the means to find extremal functions, which are the candidate functions to be extremant, i.e. to minimize or maximize the generic functional $J[f]$. These means consist in the Euler-Lagrange differential equation for functionals [39].

It is worth noting that the functional (3.20) depends by a function f of two variables. Observe that the CoV requires that a functional J depends by functions of independent variables. Therefore, we will start by considering d_{21}, d_{31} as two independent variables. Then, the function f within the Euler-Lagrange equation will be written as a function of a single (independent) variable, i.e. the time-delays ratio. The time-delays d_{21},d_{31} dependence will be resumed *a posteriori* by selecting two appropriate functions providing the found extremal function f.

It is useful for a following analysis in the Chapter (4) to formal prove that the functional (3.20) can be rewritten the form $J[d_{21}(\theta), d_{31}(\theta)]$, namely depending by two functions of a single (independent) variable θ. To this aim, the Lagrangian function, neglecting the constant terms, is written as:

$$\begin{array}{l} \left(\frac{\partial f}{\partial d_{21}}\right)^2 + \left(\frac{\partial f}{\partial d_{31}}\right)^2 = \left(\frac{\partial f}{\partial \eta}\frac{1}{d_{31}}\right)^2 + \left(-\frac{\partial f}{\partial \eta}\frac{d_{21}}{d_{31}^2}\right)^2 = \\ = \left(\frac{\partial f}{\partial \eta}\right)^2 \left(\frac{d_{31}^2(\theta)+d_{21}^2(\theta)}{d_{31}^4(\theta)}\right) \end{array} \tag{3.21}$$

where $\eta = d_{21}/d_{31}$ was posed. By using the theorem of the inverse function derivative, the term $\partial f/\partial \eta$ can be rewritten as:

$$\frac{\partial f}{\partial \eta} = \frac{1}{\frac{d\left(\frac{d_{21}(\theta)}{d_{31}(\theta)}\right)}{d\theta}} = \frac{d_{31}^2(\theta)}{d_{21}'(\theta)d_{31}(\theta) - d_{21}(\theta)d_{31}'(\theta)} \tag{3.22}$$

Therefore:

$$J[d_{21}, d_{31}] = \frac{2\sigma_{d-Max}^2}{\theta_0} \int_{-\theta_0}^{\theta_0} \frac{d_{31}^2(\theta) + d_{21}^2(\theta)}{\left(d_{21}'(\theta)d_{31}(\theta) - d_{21}(\theta)d_{31}'(\theta)\right)^2} d\theta \tag{3.23}$$

Observe that the last functional proved the equivalence with Eq. (3.20) and, at the same time, allows to select a prior probability function $f(\theta)$ which differs by a uniform density function (implicit in (3.23)). However, the functional in Eq. (3.23) involves an Euler-Lagrange equation more complicated w.r.t. functional (3.20). Therefore, to proceed we consider the functional in the previous form (3.20).

Given an integrand function for a functional of form $F(x, y, f(x, y), f_x, f_y)$, the Euler's equation is given by:

$$F_f = \frac{\partial F_{f_x}}{\partial x} + \frac{\partial F_{f_y}}{\partial y} \tag{3.24}$$

where $F_f = \frac{\partial F}{\partial f}$, $F_{f_x} = \frac{\partial F}{\partial f_x}$ and $F_{f_y} = \frac{\partial F}{\partial f_y}$. It follows that the following system must be solved:

$$\begin{cases} f_{d_{21}d_{21}} + f_{d_{31}d_{31}} = 0 \\ +\text{boundary conditions} : f = g(d_{21}, d_{31})|_{\partial\Omega} \end{cases} \tag{3.25}$$

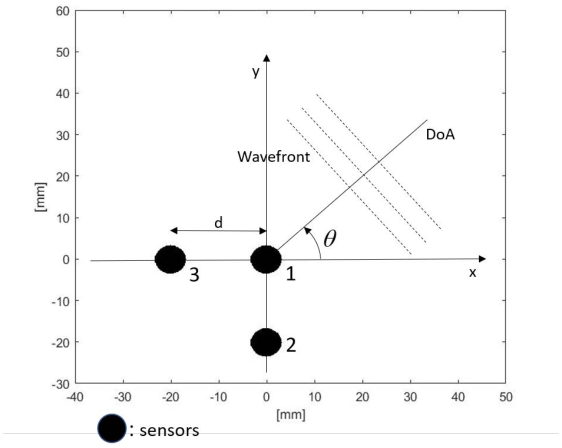

Figure 3.7: Standard Cluster (SC) of circular sensors

The first of ((3.25)) is the Laplace equation which is solved by harmonic functions. More specifically, we seek solutions in the form $f(d_{21}/d_{31})$ which limits[2] the possible set of admissible domains for Ω.

By posing again $\eta = d_{21}/d_{31}$ the two terms of Eq. (3.25) can be written as:

$$\begin{aligned} f_{d_{21}d_{21}} &= \frac{\partial^2 f}{\partial \eta^2}\frac{1}{{d_{31}}^2} \\ f_{d_{31}d_{31}} &= \frac{1}{{d_{31}}^2}\left(\frac{\partial^2 f}{\partial \eta^2}\eta^2 + \frac{\partial f}{\partial \eta}2\eta\right) \end{aligned} \tag{3.26}$$

Then, the first equation of ((3.25)) becomes:

$$\frac{f''(1+\eta^2)+f'2\eta}{\hat{d}_{31}^2} = 0 \tag{3.27}$$

where $f' = \frac{\partial f}{\partial \eta}$ and $f'' = \frac{\partial^2 f}{\partial \eta^2}$. We can assume that $d_{31} \neq 0$.Then, by integrating equation ((3.27)), we obtain:

$$\theta = f\left(\frac{d_{21}}{d_{31}}\right) = c_1 \text{atan}\left(\frac{d_{21}}{d_{31}}\right) + c_2 \tag{3.28}$$

---

[2] Such limitation allows to associate the the ratio between the DToAs to the ratio between the difference in distances among the senors along the different directions and neglect the propagation velocity.

where c_1 and c_2 are constants to be determined by taking into account the range of θ. Eq. ((3.28)) is the extremal function, candidate to minimize the functional ((3.20)). It allows to select the Mean Square Error (MSE) estimator in the form:

$$\hat{\theta} = f\left(\frac{\hat{d}_{21}}{\hat{d}_{31}}\right) = c_1 \text{atan}\left(\frac{\hat{d}_{21}}{\hat{d}_{31}}\right) + c_2 \tag{3.29}$$

Observe that the CoV, when is applied to realistic physics problem, typically provides an extremant function. In our context, the aim is related to the physics of waves and to find their DoA with minimum uncertainty, for this reason, function (3.28) is an extremant function for the functional (3.20). Furthermore, by selecting any other function, it can be observed that (3.29) is the optimal estimation function, in terms of minimum variance of worst case. Our goal is to find the two function $d_{21}(\theta)$ and $d_{31}(\theta)$ which minimize the functional (3.23). By computing the $\sigma^2_{\hat{\theta}}$ and $\sigma^2_{\hat{\theta}-WorstCase}$, considering the estimator (3.29), the followings results are obtained:

$$\begin{aligned} \sigma^2_{\hat{\theta}} &= \frac{1}{c_1^2} \frac{\hat{d}_{21}^2 \sigma^2_{\hat{d}_{31}} + \hat{d}_{31}^2 \sigma^2_{\hat{d}_{21}}}{\left(\hat{d}_{21}^2 + \hat{d}_{31}^2\right)^2} \Bigg|_{E[d_{21}],E[d_{31}]} \\ \sigma^2_{\hat{\theta}-WorstCase} &= \frac{1}{c_1^2} \frac{\sigma^2_{d-Max}}{\left(d_{21}^2 + d_{31}^2\right)^2} \Bigg|_{E[d_{21}],E[d_{31}]} \end{aligned} \tag{3.30}$$

It must be noticed that, considering two functions $E[\hat{d}_{21}(\theta)] = d_{21}(\theta)$, $E[\hat{d}_{31}(\theta)] = d_{31}(\theta)$ with an upper and lower bounds, the two functions which minimize the $\sigma^2_{\hat{\theta}-WorstCase}$ are a sine and cosine function with the same upper and lower bounds, i.e. r/v.

A Standard Cluster (SC) of 3 disk-sensors is shown in Fig. (3.7)(a)), corresponding to the MSE estimator in (3.29), with the values of the constants $c_1 = 1$, $c_2 = 0$. This cluster configuration was validated by Kundu et al. [17]. In this case we have that:

$$d_{21}(\theta) = \frac{r \sin\theta}{v} \quad d_{31}(\theta) = \frac{r \cos\theta}{v} \tag{3.31}$$

where r is the distance between the sensors. Using (3.18), we can calculate the variance (and its value of worst case) of the SC corresponding estimator as:

$$
\begin{aligned}
\sigma^2_{\hat\theta} &= \left.\frac{\hat d_{21}^2\sigma^2_{\hat d_{31}}+\hat d_{31}^2\sigma^2_{\hat d_{21}}}{\left(\hat d_{21}^2+\hat d_{31}^2\right)^2}\right|_{E[d_{21}],E[d_{31}]}\\
&= \left(\tfrac{v}{d}\right)^2\left(\sin^2(\theta)\sigma^2_{\hat d_{31}}+\cos^2(\theta)\sigma^2_{\hat d_{21}}\right)\\
\sigma^2_{\hat\theta-WorstCase} &= \left(\tfrac{v}{d}\right)^2\sigma^2_{d-Max}
\end{aligned}
\tag{3.32}
$$

Although the SC already provides the optimal solution, it can be observed that it is optimal when an area of 360° is monitored. However, in many realistic scenarios, just a DoAs sector has to be monitor, e.g. a quadrant of 90°. In this case, the two constant can be set to $c_1 = 1/2$ and $c_2 = 0$. The pair of optimal functions $d_{21}(\theta)$,$d_{31}(\theta)$ are given by:

$$
d_{21}(\theta) = \frac{r\sin 2\theta}{v} \quad d_{31}(\theta) = \frac{r\cos 2\theta}{v} \tag{3.33}
$$

The functions ((3.33)) define our *Optimal Cluster of Shaped Sensors* (SS-OC). Again, by applying the (3.18), the $\sigma^2_{\hat\theta}$ and $\sigma^2_{\hat\theta-WorstCase}$ can be computed:

$$
\begin{aligned}
\sigma^2_{\hat\theta} &= \left.\frac{\hat d_{21}^2\sigma^2_{\hat d_{31}}+\hat d_{31}^2\sigma^2_{\hat d_{21}}}{\left(\hat d_{21}^2+\hat d_{31}^2\right)^2}\right|_{E[d_{21}],E[d_{31}]}\\
&= \tfrac{1}{4}\left(\tfrac{v}{d}\right)^2\left(\sin^2(2\theta)\sigma^2_{\hat d_{31}}+\cos^2(2\theta)\sigma^2_{\hat d_{21}}\right)\\
\sigma^2_{\hat\theta-WorstCase} &= \tfrac{1}{4}\left(\tfrac{v}{d}\right)^2\sigma^2_{d-Max}
\end{aligned}
\tag{3.34}
$$

Note that it is possible to reduce the uncertainty of the estimation by acting on the trade-off uncertainty-work-range of DoA. The reduction factor of the square root of the variance of worst case $\sigma_{\hat\theta-WorstCase}$, is equal to the reduction factor of the work-range (for the SS-OC it is possible to work within $(-\pi/4, \pi/4)$ and in the dial diametrically opposite to this, evaluating the signs of the DToA given by ((3.33))).

The relation (3.33) can be realized through a cluster of shaped sensors with the functions $\rho_{21}(\theta), \rho_{31}(\theta)$ of ((3.16)) given by the numerators of ((3.33)). However, it can be observed that the last ones are strongly non linear. A simple step sensor-shape-function on a compact area, resulting by a binary quantization procedure, shows strong limits to get the desired non linear trends in the Radon domain.

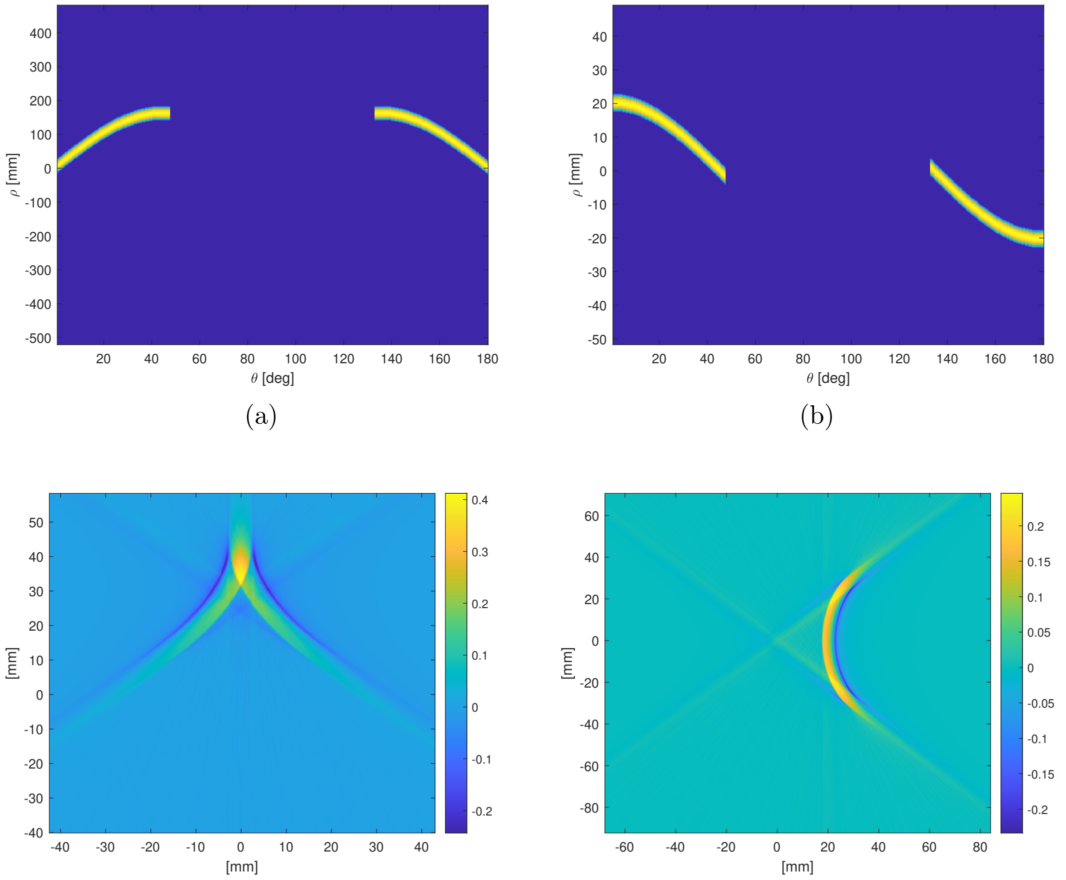

(a) (b)

(c) (d)

Figure 3.8: A graphical illustration of the SS-OC design procedure. P2 and P3 are related to first and second column respectively: (a)-(b) Imposed RTs (according to the numerators of the Eqs. (3.33); (c)-(d) IRTs: ideal shape functions

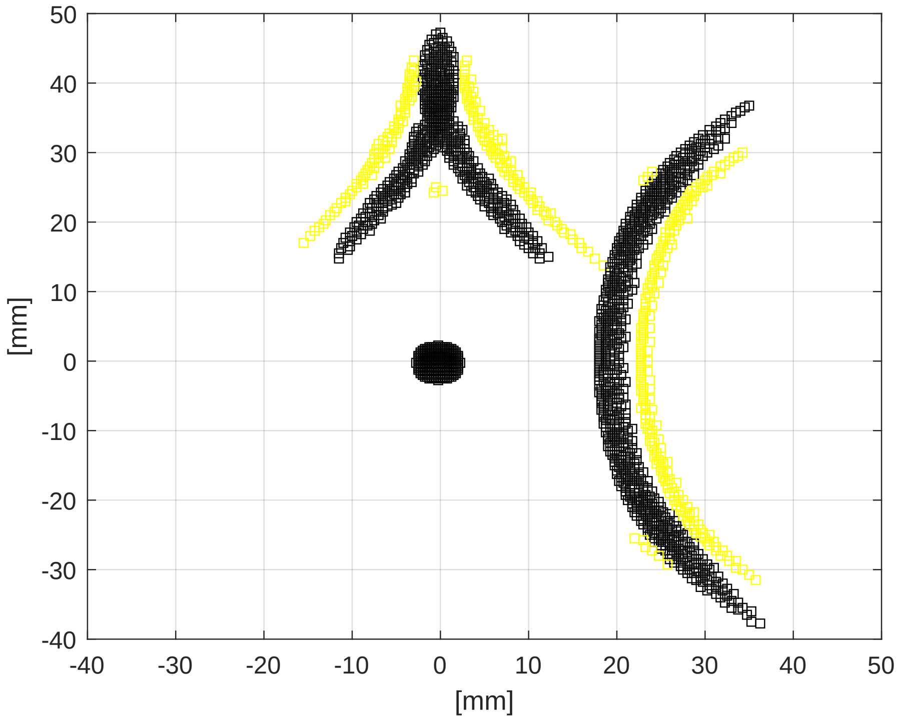

Figure 3.9: The Optimal Cluster of Shaped Sensors (SS-OC), after applying the *Error Diffusion* quantization technique (in black colour the positive sensors shape function parts, in yellow colour the negative sensors shape function parts).

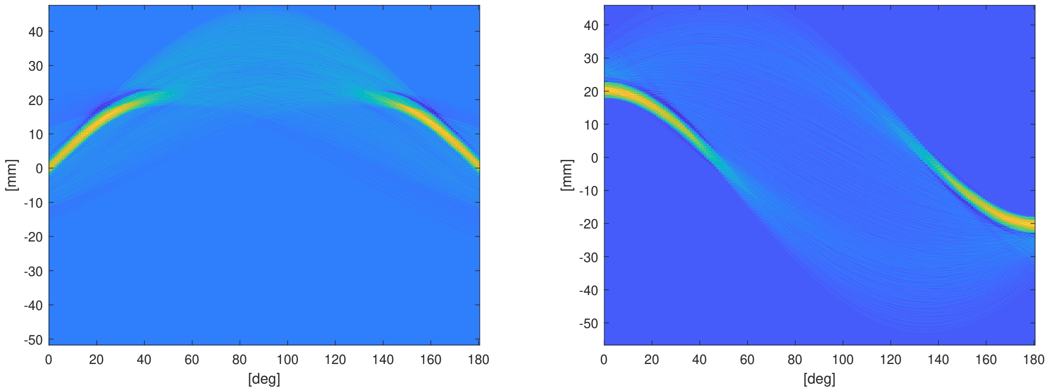

(a) (b)

Figure 3.10: The Radon Transform of the sensors after applying the *error diffusion* quantization technique: (a) Actual RT of P2; (b) Actual RT of P3.

In order to address this problem, it is necessary to define a sensor shape function which is continuously modulated in its values. Techniques developed in image processing to quantize grey scale images with a bit per pixel, can be fruitfully adopted for the transducer design purpose. In particular, the so called *dithering* or *half-toning* techniques can be used (see the works [40, 41]). Among these, the *Error Diffusion* technique is able to work on image sub-areas. Therefore, what the algorithm does at one location influences what happens at other locations. Other simpler techniques do not have these complications but have worse performance in terms of "similarity" parameters w.r.t. the starting image. In more detail, in the error diffusion approach, the image is scanned, the pixel is quantized and the quantization error is subtracted from the adjacent pixels on the basis of the coefficients of a predetermined filter (error filter). This technique will be exploited and adapted, in Chapter (6), to detect and excite waves just in one verso.

To proceed, by following the steps of the RT procedure, defined in the previous Section (3.1.1)), two continuously modulated shape functions are obtained. A graphical illustration of the RT procedure, for the actual case is given in Fig. (3.8). The *Error Diffusion* technique is then applied on the P2 and P3 sensors shape functions. In the Fig. (3.10) are shown the RTs of the quantized sensors.

Although the experimental validation of the shaping concept was not the main target of my research, some aspects were considered for a design relevant to the technological possibilities. It is worth mentioning that the proposed cluster of shaped sensors can be realized by relying on different piezoelectric materials and manufacturing techniques. E.g., metallized PVDF (polyvinylidene fluoride) sheets can be used by shaping the electrodes on the upper surface with a laser cut as in [42, 43]. Alternatively, the shaping strategy can be based on printing metallic electrodes on PVDF films or PZT (Lead Zirconate Titanate) piezo-sensors, in order to obtain the desired shape sensors as proposed in [44], or by using litographic procedures as in [45]. In [46], an experimental validation of a shaped PZT transducer, obtained via the screen-printing technique, is provided. In the practical adoption of these devices, a fundamental step is the definition of a well controlled bonding procedure, because it may heavily affect the sensor response [31].

Among the last techniques, the PVDF or PZT screen printing was considered for its relative good resolution, near to the 200/250[um], and, at the same time, to limit the manufacturing cost.

It is worthy to note that the cabling of SHM dithered sensors is another important issue to be considered. The main problem is to short-circuit the piezo-patch descrete locations. Some strategies are currently being investigated such as applying the dithering just to the lower electrode which must be grounded.

Therefore, the design procedure was computed to achieve a dots-shape functions with a resolution of 0.25[mm] to satisfy the limitations that are associated with patch manufacturing. Therefore, the half-toning technique was applied according to the following steps:

1. The sensors shape functions are divided in two parts: the positive values part and a negative values one.
2. In order to limit the physical sensors size, for each parts, the absolute values lower than the 25% of the maximum absolute value, are discarded.
3. The *Error Diffusion* imaging technique is applied on each parts. As result, each sensor is composed by two parts. However just a single differential acquisition channel is required, namely no additional hardware complexity is required.

The resulting SS-OC is illustrated in Fig. (3.9). It is worth noting that the increased performance is not due to higher distances between sensors. Indeed, the maximum distance between sensors, which defines the maximum time-window duration and how much the dispersive effect influences the acquired signals, can be defined just in the RT domain, via the maximum DDoP. Because in the RT domain, the same maximum distance of disks sensors is imposed, the comparison of two clusters is provided with the same computational cost (i.e. the same maximum duration of time-windows to be stored and processed) and with the same detrimental dispersion effect.

3.1.3 Numerical validation: performance and discussion

In order to validate the design procedure of the shaped sensors and the performance of the proposed DoA estimator, a numerical analysis was performed. The estimation functions of the two clusters of Fig. (3.7) are respectively:

$$\hat{\theta}_{SC} = f\left(\frac{\hat{d}_{21}}{\hat{d}_{31}}\right) = \text{atan}\left(\frac{\hat{d}_{21}}{\hat{d}_{31}}\right) \quad ; \quad \hat{\theta}_{SS-OC} = f\left(\frac{\hat{d}_{21}}{\hat{d}_{31}}\right) = \frac{1}{2}\text{atan}\left(\frac{\hat{d}_{21}}{\hat{d}_{31}}\right) \tag{3.35}$$

In particular, impact waves propagating in aluminium plate 1[mm] thick (Young's modulus 70 [GPa], Poisson's coefficient 0.3 and material density 2700 [Kg/m^3]) were simulated with the Green's functions formalism adopted in [26] (see Sec. (2.1.2)). The impulse response of a band pass Butterworth filter (10th order) with different bandwidths and center frequencies was used in order to simulate the impact signal. The two DToAs with respect to the first sensor d_2, d_3 were computed from the simulated acquired signals by locating the peaks of the cross-correlation ([19]) (an ML estimator approximation for uncorrelated time-delays)

Simulations were performed for multiple impact locations obtained by varying the true DoA with 5° steps ($\theta = -45°, -40°, -35°, ..., 45°$), the distance from the reference sensor P1 being 0.8 [m]. The results achieved by the clusters of Figs. (3.7) and (3.9) are given in Tables (3.1),(3.2) and (3.3), for different center frequencies and bandwidths of the impact signal and different Peak Signal to Noise Ratios (PSNR).

The selected bands were arbitrarily chosen as representative of three different cases of impact signals whose frequency content may vary due to different factors such as the impact energy and the material characteristics. The sensor performance itself is influenced by the wave velocities (both phase and group) which, in turn, depends on frequency and material characteristics. In fact, due to the wave number filtering effect, even if the same piezo sensor is used, its amplitude-frequency response (AFR) changes according to the wave vector dispersion function $k_0(\omega)$. Indeed, on the basis of model (2.18), the AFR of a piezo-disk, in the case of a piezo-material with single polarization and $H(\theta)$ constant, is simply given by the product of disk directivity $D(k_0(\omega), \theta)$ for $k_0(\omega)$. An approximated expression of the last one (see Sec. (5.1)), can be written as:

$$V_{Disk}(k_0(\omega), \theta) \approx jk_0(\omega)2\pi R^2\text{sinc}(Rk_0(\omega)) \tag{3.36}$$

As final result, the frequencies have not the same gain and the AFR will be

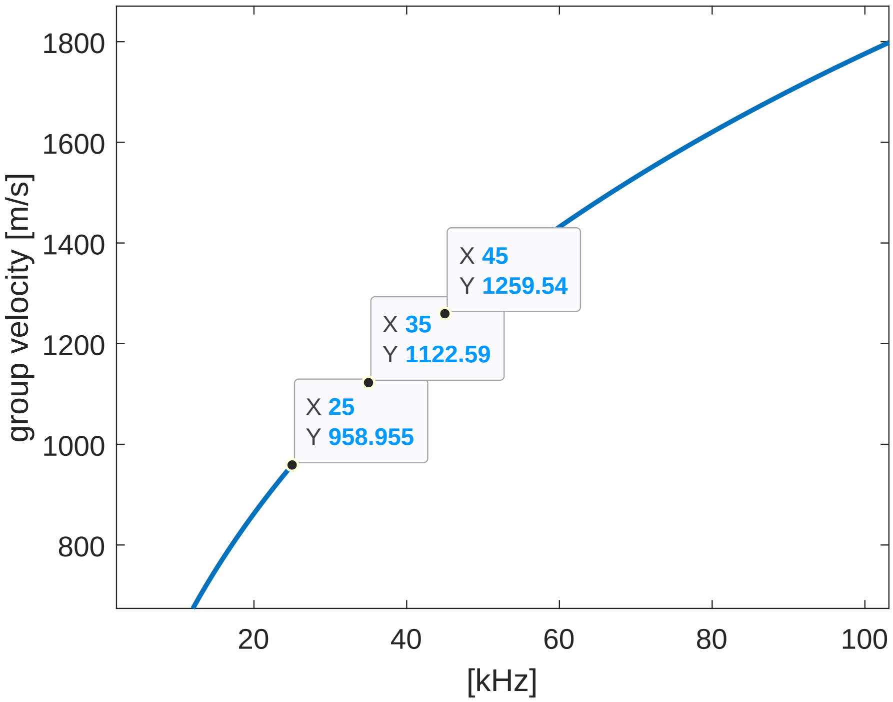

Figure 3.11: A_0 mode group velocity as function of frequency, in a aluminium plate (1[mm] thick). Its values at the center frequency of the bands considered for the numeric results (see Tabs. (3.1),(3.2) and (3.3)) are highlighted.

characterised by a sequence of peaks, corresponding to wavelengths which are more "tuned". To take into account this phenomenon, in the following, the DoA estimation performance will be given as PSNR varies.

To assess the Standard Deviation (SD) of DoA estimations, 100 simulations, on the entire 90° sector, were performed. Furthermore, the Maximum Error (ME) over all simulations was considered. The simulations were run simulating the propagation of the A0 Lamb mode, and considering: i) circular piezo sensors with radius equal to 2.5 [mm], ii) maximum DDoP between sensors d equal to 2 [cm], iii) sampling frequency (Fs) equal to 2 [MHz].

As shown in Tab. ((3.1), (3.2), (3.3)), the SD and ME values obtained with the shaped sensors are, as expected, smaller w.r.t. the SC, particularly when the PSNR value decreases. This behaviour can be interpreted in the following way. Due to the non-ideal calibration curve (i.e. which differs by ideal $1/2\arctan(\cdot)$, obtained via the Eqs. (3.33)) achieved by the shaped sensors, there is an error ($bias$), different

	Standard Cluster		**Optimal Cluster of Shaped Sensors**	
PSNR (dB)	SD [deg]	ME [deg]	SD [deg]	ME [deg]
60	1.13	1.95	**2.53**	**4.53**
40	1.38	4.09	**2.52**	**5.77**
35	1.77	5.75	**2.59**	**6.98**
30	2.75	8.37	**2.76**	**7.64**
28	3.16	10.8	**2.92**	**8.61**
27	3.51	12.2	**2.92**	**8.57**
26	3.88	13	**2.99**	**8.91**
24	4.91	17.7	**3.36**	**11.10**
22	5.88	20.1	**3.67**	**12.10**
20	7.25	23.7	**4.19**	**15.40**

Table 3.1: Comparison of Standard Deviation (SD) and Maximum Error (ME) values (in degrees) between the arrays of the Figs. (3.7), (3.9), for noise-affected measurements at different PSNR values. Actuated pulse band: [20-30][kHz].

	Standard Cluster		**Optimal Cluster of Shaped Sensors**	
PSNR (dB)	SD [deg]	ME [deg]	SD [deg]	ME [deg]
60	1.2	1.87	**1.86**	**3.46**
40	1.49	4.42	**1.86**	**4.99**
35	2.12	6.63	**2.04**	**5.58**
30	3.28	10.9	**2.44**	**7.88**
28	3.97	14	**2.59**	**9.11**
27	4.47	14	**2.89**	**9.22**
26	4.86	15.1	**3.04**	**10.30**
24	5.92	21	**3.55**	**12.80**
22	7.29	26.3	**4.20**	**14.50**
20	9.12	30	**4.90**	**17.10**

Table 3.2: Comparison of Standard Deviation (SD) and Maximum Error (ME) values (in degrees) between the arrays of the Figs. (3.7), (3.9), for noise-affected measurements at different PSNR values. Actuated pulse band: [30-40][kHz].

	Standard Cluster		**Optimal Cluster of Shaped Sensors**	
PSNR (dB)	SD [deg]	ME [deg]	SD [deg]	ME [deg]
60	1.14	2.35	**1.18**	**2.05**
40	1.13	2.65	**1.2**	**2.45**
35	1.25	3.43	**1.2**	**2.95**
30	1.61	4.9	**1.32**	**3.62**
28	1.84	5.95	**1.38**	**4.05**
27	1.99	6.34	**1.47**	**4.2**
26	2.17	7.41	**1.49**	**5.06**
24	2.59	8.43	**1.64**	**5.65**
22	3.06	10.8	**1.89**	**6.08**
20	3.63	13.4	**2.11**	**7.45**

Table 3.3: Comparison of Standard Deviation (SD) and Maximum Error (ME) values (in degrees) between the arrays of the Figs. (3.7), (3.9), for noise-affected measurements at different PSNR values. Actuated pulse band: [30-60][kHz].

for the considered band, in the estimation function. However, the last disadvantage is overcompensated when the noise increases, thanks to the achieved curve, more robust w.r.t. the uncertainties on the estimated time-delays (i.e thanks to the reduced *variance* (3.34)).

Due to the wave dispersion of the A0 mode, the higher is the considered center frequency, the higher is the wave (group) velocity v (see Fig. (3.11)). Therefore, according the the variances (3.32) and (3.34), which increase as v^2, worse performances are achieved by both clusters when the band center frequency increases. This behaviour appears in the SS-OC when the noise increases, for the above-mentioned reason.

Conversely, when the signal bandwidth increases, a more impulsive signal is detected and the time-delays uncertainties are smaller. The last implication, will be better clarified in Chapter (4) where the time-delays covariance matrix will be expressed as function of the signal and noise spectrum. Therefore, the two terms, wave velocity and central frequency have an opposite influence on the DoA estimation performance (compare Tab. (3.1) and (3.2), and Tab. (3.3) which are characterized by a 10 and 30 [kHz] Bandwidth, respectively).

3.1.4 A RT application: time-response computation

A RT method useful to compute the time-response of a piezo to take into account both the wave number tuning, due to the piezo-sensor, and the dispersion effect, due to the GWs propagation, was software implemented. The procedure can be summarized roughly in three steps:

1. The RT of a shape function is computed. Note that if a complex shape function is designed (see the Ch. (6)) to detect or excite directional waves, its Complex Radon Transform (CRT) is computed as the sum of the real part RT and the imaginary one. In the following, the CRT will be considered to cover both real shape functions and complex ones.
2. The CRT is shifted along the spatial coordinate ρ to take into account the distance between the transducer and the defect-target, when a signal is excited and conversely between the defect-target/impact point and the sensor, when a signal is acquired. The spatial FT domain (k_0-domain) of the RT (ρ-domain) is computed for each DoA θ. Therefore, in order to move from the spatial FT (k_0-domain) to the time-FT (ω-domain) a non-uniform sampling of the spatial 1D-FFT of each angle is computed (according to the dispersion curve). It is important to highlight that a zero-padding technique has to be applied to the CRT so that different discrete k_0 values of the dispersion curve refer to different spatial FT values (indexed by integers), also when the excitation signal has an high resolution in the ω discrete values. If the zero-padding technique is not applied appropriately, as result, spurious time signal components can arise. The computed time-FT is the Directivity as function of ω. According to the frequency response model (2.18), the Directivity is then multiplied for $k_0(\omega)$. In order to ensure the Hermitian property in the frequency domain, the two-sided spectrum is computed via the one-sided spectrum and its complex conjugate one. The last procedure provides the Frequency Impulse Response (f-IR) at each angle θ.
3. The f-IR, for each angle, is multiplied by the excitation signal spectrum $U(\omega)$ or the impact point spectrum, when the sensor is used in acquisition phase.

> The time response is computed via a simple 1D-IFFT. It is equal to the convolution product in the time domain.

As example, in Fig. (3.12) the time responses of a piezo-patch P2 of Fig. (3.9) (a sensor quantized via the *error diffusion* technique), provided by the previous RT procedure and by the GFs formalism simulation, are shown. They match quite-well and it can be observed that the larger the distance, the more wave packet spreads over the time due to dispersion effect. The responses are quite similar so that the analytical model can be used as a simulator with a negligible computation time. In the Ch. (6), Sec. (6.6.2), the explained technique will be used to compute the time response of a quantized complex shape function.

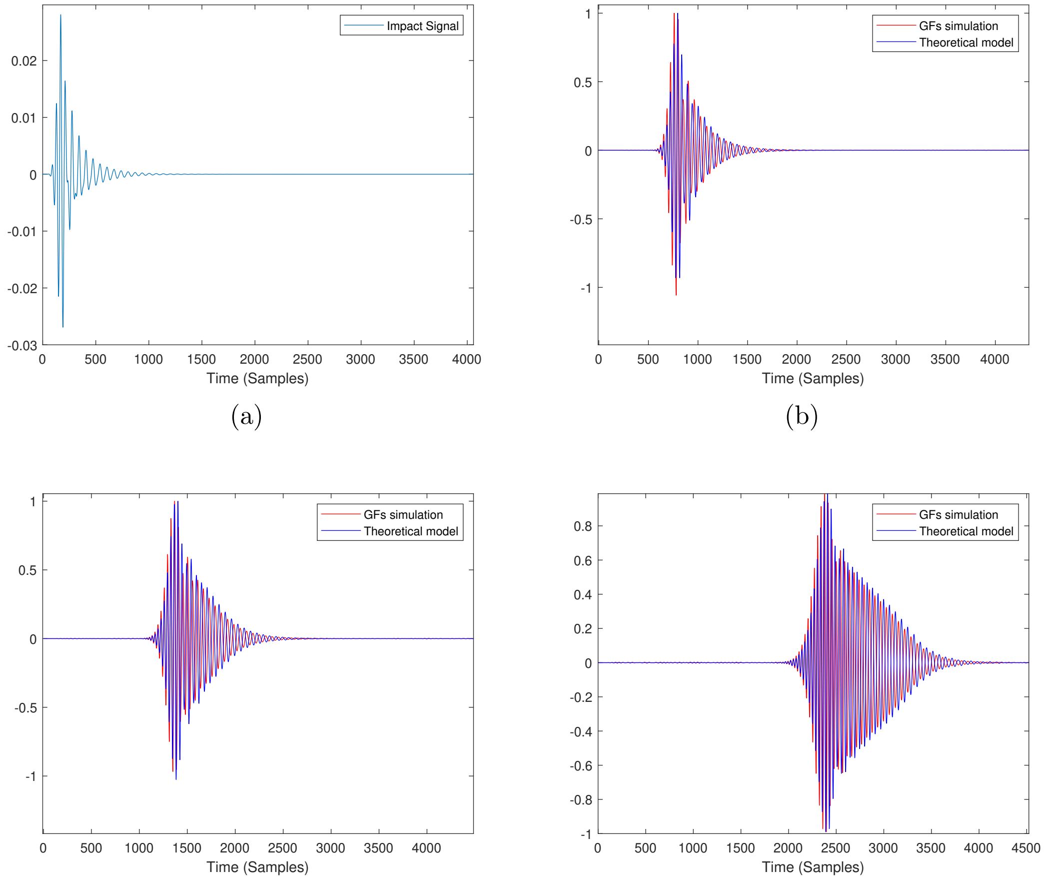

(a) (b)

(c) (d)

Figure 3.12: The comparison of time-responses provided by the GFs simulations and the RT procedure, when the sensor P2 of the Fig. (3.9) is used as example: (a) impact signal at angle 10[deg] (the impulse response of the Butterworth filter (10-th order) with cut-off frequencies equal to 30[kHz] and 60[kHz]; (b) P2 time responses with a 0.4[m] impact distance; (c) P2 time responses with a 0.8[m] impact distance; (d) P2 time responses with a 1.5[m] impact distance.

Chapter 4

Arrays Design for noisy environments

Disclaimer: *The content of this Chapter is based upon the research work [47]: Marco Dibiase, Masoud Mohammadgholiha, and Luca De Marchi. "Optimal Array Design and Directive Sensors for Guided Waves DoA Estimation". In: Sensors 22.3 (2022), p. 780.*

In the Chapter (3), the noisy measurements issue has been tackled by exploiting the sensors shape. The *Optimal Cluster of Shaped Sensors* was compared with the cluster of disk-sensors placed on the vertices of an isosceles right triangle [17], here, already referred to as *Standard Cluster* (SC). In the Sec. (3.1.2) was proved that the SC is the optimal solution when a 360° area is covered.

However, in many realistic cases only a restricted angular range is requested to be monitored, e.g. a quadrant of 90°. Therefore, the main aim of this Chapter is to define an optimality criterion to find the optimal displacement of disk-sensors composing a cluster, for a considered angles work-range and the wave-velocity being unknown.

Although, in principle, it is possible to use the Eq. (3.23) by simply considering the DToAs, $d_{j1}(\theta)$, as functions of disks coordinates, a more refined procedure will be defined to be suitable for a M-sensors cluster and to take into account also a noise model.

By assuming the Additive White Gaussian Noise model (AWGN), the time-delays variance-covariance matrix can be computed. Observe that the AWGN assumption is fully justified when the electrons thermal motion of the electronic devices circuitry is the main noise contribution.

Note that in the Eq. (3.18), namely the propagation of uncertainty formula, the variance-covariance matrix was assumed to be diagonal, i.e. with the covariance terms, $\sigma^2_{\hat{d}_{23}}$ and $\sigma^2_{\hat{d}_{32}}$, equal to 0 or negligible. Therfore, the SC can be considered the optimal solution for a 360° angles-work-range, only under the last assumption as well as the sensors shape of the SS-OC.

Unlike the procedure followed in the Sec. (3.23), where the variance of an estimator was minimized in average sense, we will release by a particular form of a DoA estimator, by using the Cramér–Rao (Lower) Bound (CRB), which defines the minimum variance achivable by any unbiased estimator.

It is worth noting that the last procedure is equal to minimize the variance of the estimator (3.17), when a cluster of three sensors is considered, because the form (3.17) is mandatory, wave velocity unknown being. Conversely, for an arbitrary number of sensors, M, the two procedures are equal if and only if a Maximum Likelihood (ML) estimation function $\hat{\theta} = f\left(\hat{d}_{21}, \hat{d}_{31}, ..., \hat{d}_{M1}\right)$ is provided, when the wave velocity v is considered unknown. Actually an ML estimator, is not known *a priori*. Then, the CRB will be used as cost function to be minimized in mean sense. This approach is also known as Bayesian CRB or *global*.

In [48], Oktel and Moses have already proposed the Bayesian approach of the Cramér Rao bound, which depends on the sensors positioning. However, in that work, the wave velocity is supposed to be known. Conversely, in many applications, such an assumption is not verified and results in a loss in accuracy.

Therefore, as new approach, firstly we will compute the Cramér Rao Matrix Bound (CRMB) of the unknown parameters θ and v, via the time-delays variance-covariance matrix, with a AWG Noise model. After that, the CRMB first element, related only to θ, will be minimized in mean sense.

In the following Sections the system model, the $\mathrm{CRMB}_{\theta-v}$ and the Bayesian $\mathrm{CRB}_{unknown-v}$ will be derived. The last one will be related also to the sensors shape finding problem. The optimal sensors positioning solution for a 3-disk-sensors cluster will be provided. An important link between the array beampattern and the Bayesian $\mathrm{CRB}_{unknown-v}$ will be shown. A DoA effcient estimator able to attain the $\mathrm{CRB}_{unknown-v}$ was found and used to numerically assess the improved performance in DoA estimation via the proposed 3-sensors designed array, referred to as *Disk*

Sensors Optimal Cluster (DS-OC).

4.1 System Model and Cramér-Rao Matrix Bound

Without lack of generality, let us assume that the sensors array consists of only three (identical) sensors: P1, P2, and P3. The sensors are located at $\mathbf{r}_i = [x_i, y_i]^T$ for $i \in [1, 2, 3]$. Following [12, 49], we adopt a model with a single co-planar far-field source which generates the wavefield impinging the 3 sensors array. The signal at the ith sensor is $s(t - d_i)$, where $s(t)$ is the signal at a reference point near the array and d_i is the delay at the ith sensor w.r.t. the reference point. Without loss of generality, the reference point is assumed to be coincident with the location of the first element in the array, P1, so that $d_1 = 0$. We assume also that the sensors are near enough so that the amplitude gradient across the array and the effect of wave dispersion are negligible. The output signal of the ith sensor can be expressed as:

$$x_i(t) = s(t - d_i) + n_i(t) \tag{4.1}$$

where $n_i(t)$ is the additive sensor noise at ith sensor. In order to estimate the DoA of wavefront, we first estimate the vector of DToAs, $\mathbf{d} = [d_2, d_3]^T$. In the discrete Fourier domain, the 3 × 1 measurements vector at kth frequency ω_k, is given by:

$$\mathbf{x}(\omega_k) = \mathbf{a}_\theta(\omega_k) s(\omega_k) + \mathbf{n}(\omega_k) \tag{4.2}$$

where $\mathbf{a}_\theta(\omega_k)$ is the steering vector, defined as:

$$\mathbf{a}_\theta(\omega_k) = \left[1, e^{j\omega_k d_2(\theta)}, e^{j\omega_k d_3(\theta)}\right]^T \tag{4.3}$$

where $d_i(\theta) = (\mathbf{u}^T(\theta) \cdot \mathbf{r}_i - \mathbf{u}^T(\theta) \cdot \mathbf{r}_1)/v$ is the DToA between the ith sensor and the reference sensor P1, v is the wave velocity and $\mathbf{u}(\theta) = [\cos(\theta), \sin(\theta)]^T$ is the unit vector pointing toward the signal source. The followings hypotheses are formulated:

1. The noises are stationary Gaussian processes with zero mean. The signal is a Gaussian process with zero means, approximately stationary. The last hypothesis assumes that, for a narrowband signal and for closely spaced sensors, the dispersion effect can be neglected;

2. The signal and noises are mutually uncorrelated and uncorrelated between themselves;

Under the previous hypotheses, Hahn and Tretter in [49], derived the Cramér-Rao Matrix Bound (CRMB), $\mathbf{Q}$, for the delays. Let $\mathbf{d} = [d_{21}, d_{31}, ..., d_{M1}]^T$ be the estimated $M-1$ DToAs vector from M sensors. The covariance matrix $\mathbf{Q}$ is given by [49]:

$$\mathbf{Q} = \left\{ \begin{array}{l} \frac{2T}{2\pi}\int_0^B \omega^2 \frac{S(\omega)^2}{1+S(\omega)\mathrm{tr}\left(\mathbf{N}(\omega)^{-1}\right)} \\ \times \left[\mathrm{tr}\left(\mathbf{N}(\omega)^{-1}\right)\mathbf{N}_p(\omega)^{-1} - \mathbf{N}_p(\omega)^{-1}\mathbf{1}\mathbf{1}^T\mathbf{N}_p(\omega)^{-1}\right] d\omega \end{array} \right\}^{-1} \tag{4.4}$$

where 0 to B is the frequency band processed and T is the observation time. $\mathrm{tr}(*)$ is the trace of the matrix $*$. $S(\omega)$ is the signal power spectrum, $\mathbf{N}(\omega) = \mathrm{diag}\left\{N_1(\omega), N_2(\omega), ..., N_M(\omega)\right\}$ is the noise power spectral matrix, $\mathbf{N}_p(\omega)$ is the lower right $M-1$ by $M-1$ partition of the matrix $\mathbf{N}(\omega)$ and $\mathbf{1}$ is a vector of unity which has the same size of $\mathbf{N}_p(\omega)$.

We suppose that an optimal estimator is used to estimate the DToAs, such as the Maximum Likelihood (ML) estimator proposed in [49], therefore the covariance matrix, (4.4), is equal to the CRMB. Moreover, we suppose that noises have identical covariance matrix. This means that the noises have identical spectrum and in case of white noises, they have the same noise level. Note that the last assumption is typically satisfied when the acquired signals are processed by the same device and the thermal electronic noise is prevalent. When the noises have same spectrum, the covariance matrix $\mathbf{Q}$ assumes the following simple form:

$$\mathbf{Q} = \sigma_{d_i}^2 \begin{bmatrix} 1 & 1/2 \\ 1/2 & 1 \end{bmatrix} \tag{4.5}$$

where the variance of time-delays, $\sigma_{d_i}^2$, is given by:

$$\sigma_{d_i}^2 = \frac{2}{3}\frac{2\pi}{T\int\limits_0^B 2\omega^2 \frac{S^2/N^2}{1+3(S/N)} d\omega} \tag{4.6}$$

Where $S(\omega)$ and $N(\omega)$ are the power spectra of signal and noise, which are the same for each sensor. Thanks to the asymptotically Gaussian property of a ML estimator, the conditional probability density function of $\mathbf{d}$ is:

$$f(\mathbf{d};\theta) = \frac{1}{(2\pi)^2\sqrt{\det \mathbf{Q}}} \exp\left\{-\frac{1}{2}\left(\mathbf{d} - \frac{\mathbf{r}}{v}\right)^T \mathbf{Q}^{-1}\left(\mathbf{d} - \frac{\mathbf{r}}{v}\right)\right\} \tag{4.7}$$

with $\mathbf{r} = [r_2(\theta), r_3(\theta)]^T$ the vector of Differences in Distance of Propagation (DDoPs) of the wavefront between the sensors and the reference sensor P1. Note that $r_i(\theta)$ $(i = 2, 3)$ are so that the “true” values of $d_i(\theta)$ are $d_i(\theta) = r_i(\theta)/v = (\mathbf{u}^T(\theta) \cdot \mathbf{r}_i - \mathbf{u}^T(\theta) \cdot \mathbf{r}_1)_i/v$. Let’s assume that the wave velocity is unknown. So, the unknown parameters are θ and v. In [50], Malagò and Pistone provided the Fisher information Matrix (FIM) for a Gaussian distribution when the vector of the means $\boldsymbol{\mu}$ and the covariance matrix $\mathbf{Q}$ are both functions of a set of parameters $\boldsymbol{\gamma} = (\gamma_1, \gamma_2, ..., \gamma_K)^T$. The expression, specialized in our case (with $\gamma_1 = \theta$ and $\gamma_2 = v$), is the following:

$$I_{m,n}(\boldsymbol{\gamma}) = \frac{\partial\left[r_2(\theta)/v, r_3(\theta)/v\right]}{\partial\gamma_m}\mathbf{Q}^{-1}\frac{\partial\begin{bmatrix} r_2(\theta)/v \\ r_3(\theta)/v \end{bmatrix}}{\partial\gamma_n} \tag{4.8}$$

with $\mathbf{Q}^{-1}$, from ((4.5)) is given by:

$$\mathbf{Q}^{-1} = \frac{4}{3\sigma_{d_i}^2}\begin{bmatrix} 1 & -\ 1/2 \\ -1/2 & 1 \end{bmatrix} \tag{4.9}$$

The inverse of the FIM provided in Equation (4.8) is the sought CRMB for unknown parameters θ and v, which defines a lower bound of the covariance matrix for any unbiased estimator of two parameters.

4.2 The Bayesian CRB Cost Function

The D-criterion (see [51]) uses the determinant of CRMB (equal to the inverse of FIM determinant, often called generalized covariance bound) as a cost function to be minimized to obtain the optimal design. However, in the current application domain, only the DoA estimation performance has to be optimized. Therefore, the following function has been considered:

$$\frac{\det(\text{FIM})}{I_{22}} = I_{11} - \frac{I_{12}I_{21}}{I_{22}} \tag{4.10}$$

It consists of two terms: the first one is related only to the Fisher Information (FI) on θ (when v is known) and the second one is related to information on θ and v, when they are simultaneously estimated, divided by the FI on v (when θ is known). Finally, adopting a Bayesian (or *global*) approach, similarly to [48], the following CRB$_{v-u}$ cost function is defined:

$$\begin{aligned} J_C(\mathbf{r}) &= \mathrm{E}\left[I_{22}\det(\text{CRMB})\right] = \mathrm{E}\left[\tfrac{I_{22}}{\det(\text{FIM})}\right] = \\ &= \tfrac{1}{2\theta_0}\int_{-\theta_0}^{\theta_0} \tfrac{I_{22}(\mathbf{r}(\theta))}{\det(\text{FIM}(\mathbf{r}(\theta)))} f(\theta)d\theta \end{aligned} \tag{4.11}$$

where $f(\theta)$ is the prior probability density function (pdf) of θ, thought as random variable and $[-\theta_0, \theta_0]$ is its domain, supposed compact. The column vector $\mathbf{r}(\theta)$ is function of sensors locations coordinates as:

$$\mathbf{r}(\theta) = \begin{bmatrix} (x_2 - x_1)\cos(\theta) + (y_2 - y_1)\sin(\theta) \\ (x_3 - x_1)\cos(\theta) + (y_3 - y_1)\sin(\theta) \end{bmatrix} \tag{4.12}$$

We define the CRB$_{u-v}$-optimal array $\mathbf{r}_C$ as the one whose elements location is given by:

$$\begin{aligned} &\mathbf{r}_C = \arg\min J_C(\mathbf{r}) \\ &\text{with} \begin{cases} \sqrt{x_1^2 + y_1^2} \leq \mathrm{r} \\ \sqrt{x_2^2 + y_2^2} \leq \mathrm{r} \\ \sqrt{x_3^2 + y_3^2} \leq \mathrm{r} \end{cases} \end{aligned} \tag{4.13}$$

where r is the radius of the circular domain where the sensor elements are constrained to lie in.

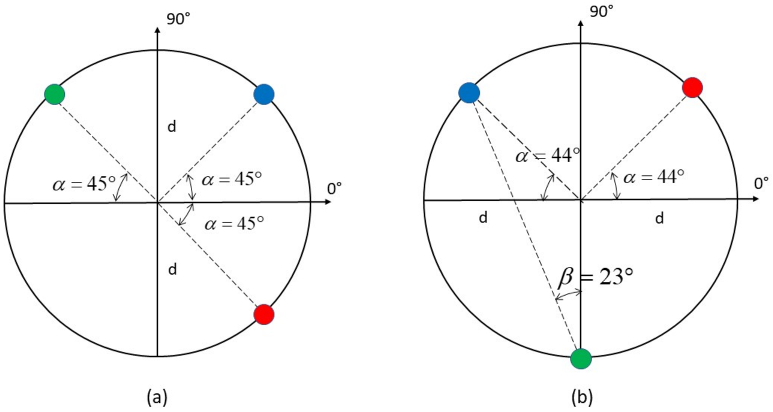

Figure 4.1: (**a**) Standard Cluster of three sensors (SC). (**b**) Disk-Sensors Optimal Cluster (DS-OC) of three sensors, optimized for DoA estimation in [−45°.45°] sector with unknown velocity v.

The general problem statement can be specified to the case of uniform pdf in a 90° sector, i.e., $[-\pi/4, \pi/4]$. Computing the terms $I_{m,n}$ of (4.8), the cost function (4.11) is:

$$J_C(\mathbf{r}) = \sigma_{d_i}^2 \frac{2v^2}{\pi} \int_{-\pi/4}^{\pi/4} \frac{r_2^2(\theta) + r_3^2(\theta) - r_2(\theta) r_3(\theta)}{\left(r_2'(\theta) r_3(\theta) - r_2(\theta) r_3'(\theta)\right)^2} d\theta \tag{4.14}$$

It is worth noting that in the last integral, the functions $r_i(\theta)$, with $i = 2, 3$, can be interpreted as generic functions of θ, if they are not prescribed in the form given by the (4.12). Therefore, by substituting $r_i(\theta) = \rho_i(\theta)$ and considering the integral (4.14) as a functional $J[\rho_2(\theta), \rho_3(\theta)]$, it can be minimized via the calculus of variations, as seen in the Sec. (3.1.2), to find the optimal sensors shape, i.e. the DDoPs functions $\rho_i(\theta)$, in presence of AWGN. Unfortunately, the Euler-Lagrange differential equation provided by (4.14) is very complicated and requires a suitable numerical solver. It can be observed that Eq. (4.14) differs by the functional (3.23) due the time-delays covariance terms which are non zero when the AWGN model is considered. As final note, the functional minimization strategy, used in the Sec. (3.1.2), applied considering the covariance matrix in the form (4.5), will be considered for future developments.

The minimization of integral (4.14) with $r_i(\theta)$ in the form (4.12) and the constraints of the (4.13), can be achieved via the Lagrange multipliers method [52]. The solution $\mathbf{r}_c$ provides a symmetric configuration with respect to 90°-axis (i.e., Y-axis), and a half-opening angle β equal to 23° (see Figure (4.1)(b)). Conversely, when the wave velocity is known, the optimized array would be symmetric w.r.t the X-axis [48]. This particular configuration is due to the minimization of the DoA accuracy loss due to the unknown wave velocity [53], via Equation (4.14). The obtained 3-sensor cluster will be referred to as *Disk Sensors Optimal Cluster* (DS-OC) while the configuration of Figure (4.1)(a), is the Standard Cluster, investigated by Kundu et al. in [18, 16].

Finally, it is worth noting that the previous design procedure of the optimal sensor positioning is still valid for a generic number M of sensors, with an appropriate covariance matrix (4.5).

4.2.1 Relationship with the array Beampattern

An important link is between the array beampattern of a conventional delay-and-sum (DAS) beamformer and the CRB. The array beampattern $G_{ij}(\omega)$, is defined as:

$$G_{ij}(\omega) = \frac{1}{M^2}\mathbf{a}^*(\theta_i, \omega)\mathbf{a}(\theta_j, \omega) \tag{4.15}$$

where $\mathbf{a}(\theta_i, \omega)$ is the steering vector, (4.3), of a source at direction θ_i, while θ_j is DoA of source and M is the number of sensors. Consider the function:

$$C(\omega, \theta) = -\left.\frac{\partial^2 G_{ij}(\omega)}{\partial\theta_i \partial\theta_j}\right|_{\theta_i=\theta_j=\theta} \tag{4.16}$$

it represents the curvature of mainlobe of array beampattern. Messer H. in [54] shows that for the case of a single far-field source, and when other parameters are known, the CRB of DoA is equal to:

$$\mathrm{CRB}(\theta) = \left(\frac{\mathrm{TW}}{\mathrm{BW}}\int\limits_{\mathrm{BW}} C(\omega, \theta)\frac{M^2\rho^2(\omega)}{1 + M\rho(\omega)}d\omega\right)^{-1} \tag{4.17}$$

where $\rho(\omega) = S(\omega)/N(\omega)$ is the Signal to Noise Ratio Factor (SNR), whereas TW/BW is the time-bandwidth ratio.

Traditionally, array performance are typically characterised in terms of the beamwidth of the beampattern rather than the mainlobe curvature value, as defined in Eq. (4.16). Although the beamwidth is a descending function of the curvature (4.16), i.e. larger the curvature is, narrower mainlobe is, the Eq. (4.17) tells us that minimising the CRB is equivalent to maximising the curvature of the mainlobe (its second derivative w.r.t. θ) for narrowband (or narrow-band-filtered) signals. In this case the ω-dependence of the function $C(\omega, \theta)$ can be neglected since the propagation velocity can be considered constant and the signal-to-noise ratio $\rho(\omega)$ can be considered approximately constant (under the approximation of nearly flat signal and noise spectra).

Then, the CRB cost function, defined as $\mathrm{E}[\mathrm{CRB}(\theta)] = \mathrm{E}[1/\mathrm{I}_{11}(\theta)]$ (see also [48]) can be thought as the average mainlobe inverse curvature of the array (averaged over the steering angle) and the optimal array provides the minimum average mainlobe inverse curvature. Whereas the defined cost function ((4.11)), i.e. $J_C(\mathbf{r}) = \mathrm{E}[1/(\mathrm{I}_{11} - \mathrm{I}_{12}\mathrm{I}_{21}/\mathrm{I}_{22})]$, is still related to the curvature with the term I_{11}, but also to the term of covariance bound, $\mathrm{I}_{12}\mathrm{I}_{21}/\mathrm{I}_{22}$, due to unknown, nuisance, velocity v parameter. A more extensive analysis might still link the defined cost function only to properties of the array beampattern.

It's worth noting that the DoA CRB (and also the CRMB for unknown v) is derived using a small perturbation analysis. Then, it represents a tight bound for DoA estimation only for DoA small-error region, namely until a certain SNR threshold value. For larger estimation error, the local tightest bound for parameters estimation is provided by the Barankin bound, BR (see [55, 56]). Messer in [54] shows that, for small SNR, the DoA Barankin bound is affected by only the higher sidelobe level. So, when the wave velocity is known, the DoA estimation performance bounds can be related only to beampattern properties. Large mainlobe curvature (i.e. narrower beamwidth) means good localization performance in the small error region (SNR higher than a threshold value). Whereas small sidelobe level is a sufficient condition for a good DoA estimation performance when large errors are involved (ambiguity due to high SNR). Because our optimization approach is related to DoA CRB, and so to the beamwidth of beampattern, better results are expected at medium-high SNR with respect to others positioning configurations.

Noteworthy, the previous discussion provides an important result: the array design via the Bayesian CRB approach is suitable both for the passive monitoring and the active one, when the defects radial and angular coordinates are to be estimated and the wave velocity knowledge, in each narrow-bands, is limited due to temperature variations, tapered monitored areas etc. Typically, in active monitoring, the sensors are excited with different phases to scan the entire round-angle. Such method is called *beam-forming* technique, also known as *delay-and-sum* technique. Observe that the sensor phase-shifts depend by the wave-velocity, whose accuracy, in turn, affects the angle accuracy. The acquired signals, for each scanned "nominal" angle, can be processed similarly to the case of the passive sensor array to estimate the DoA without using the wave-velocity knowledge, avoiding the angular accuracy loss due to the uncertainty on the previous one. The estimated angle and the nominal one can be compared to estimate the wave velocity variation w.r.t. its nominal value. Eventually, this information can be used to improve the estimation of the radial coordinate. The sensor array, in the active context, are often referred to as *Phased Array*. The state of the art of the phased arrays will be illustrated in Ch. (6).

4.3 An efficient DoA estimator

As anticipated, an efficient time delays estimator has to be used in order to match the DToAs covariance matrix with the CRMB (4.5). The Maximum Likelihood (ML) DToAs estimator, asymptotically efficient, was proposed by Hahn and Tretter in [49]. The technique consists of measuring the DToAs for all possible sensors pairs by Generalized Cross Correlation (GCC) and then calculating the Gauss-Markov (GM) (weighted) estimate of the DToAs with respect to the first sensor. The GCC procedure consists of computing the Cross-Correlation between the acquired signals, filtered first by an appropriate filter. The Optimal Filtering to attain the time delays CRMB is defined by:

$$\left|F_{OPT(\omega)}\right|^2 = \frac{S(\omega)/N^2(\omega)}{1 + M(S(\omega)/N(\omega))} \tag{4.18}$$

where M is the number of the sensor, whereas S and N are the power spectra of respectively no-noisy signal and noise. In practice, the optimal filter requires knowledge or estimation of the signal and noise spectra. A simple estimation method consists in measuring the noise spectrum and computing $S(\omega)$ by subtracting the noise spectrum from the noisy signal spectrum. However, due to random variations of noise, spectral subtraction can result in negative estimates of the short-time magnitude or power spectrum. Different methods for reducing and removing the distortions due to the rectification process are proposed in [57].

Under the hypothesis that the noises have the same spectrum for each sensors, the Gauss-Markov estimator coefficients, for the case of three sensors array (regardless of what filter is used for the GCC procedures), are given by:

$$\begin{bmatrix} d_{2GM} \\ d_{3GM} \end{bmatrix} = \frac{2}{3} \begin{bmatrix} 1 & 1/2 & -1/2 \\ 1/2 & 1 & 1/2 \end{bmatrix} \begin{bmatrix} d_{12GCC} \\ d_{13GCC} \\ d_{23GCC} \end{bmatrix} \tag{4.19}$$

where d_{ijGCC} are the DToAs between sensor i and j estimated by using the GCC procedure, whereas d_{iGM} are the time delays with respect to the reference sensor estimated with the GM estimator. The weights of the Gauss-Markov estimator have a more complex form (expressed by a ratio of time delays variances) only when the noise spectra for each sensor, N_i, are not all equal.

In this paper, for testing the DoA estimation performance with the two clusters of Figure (4.1), we assumed equal white noise spectra and a flat signal spectrum within a band B_s, to emulate the narrow-band impulsive signals due to an impact. In this case, the Optimum Filter ((4.18)) is equal to an arbitrary constant within the signal band B_s (the system performance is unaffected by filter gain constant), and 0 elsewhere:

$$|F_{OPT_{Flat}}(\omega)|^2 = \begin{cases} 1 & \omega \in B_s \\ 0 & \text{elsewhere} \end{cases} \tag{4.20}$$

The band B_s, is estimated by using the spectral subtraction technique, assuming to know the white noise level. The distortions induced by the rectification of negative values of the estimated power spectrum S are neglected. This assumption is justified when SNR values are sufficiently high, while the non-linear distortions are not negligible when the signal-to-noise ratio decreases.

Finally, an optimal DoA estimation function from the estimated time delays has to be found to attain the $\mathrm{CRB}_{unknown-v}$ (the inverse of (4.10)). Given the designed array geometry (DC in Figure (4.1)(b)), the following result is obtained:

$$d_2 = \frac{d}{v} 2\cos(\alpha)\cos(\theta) \quad , \quad d_3 = \frac{d}{v}\left(\cos(\alpha)\cos(\theta) - (1+\sin(\alpha))\sin(\theta)\right) \tag{4.21}$$

θ can be computed by using the ratio $\eta \doteq d_2/d_3$ and inverting with respect to θ. The "true" relation between θ and η can be used as estimation function:

$$\hat{\theta}_{DC} = \operatorname{atan}\left(\frac{\tan\beta(\eta-2)}{\eta}\right) , \qquad \text{with}\, \beta{=}\ 23^\circ \tag{4.22}$$

Note that the estimator $\hat{\theta}_{DC}$ is a function only the ratio d_2/d_3. From the Theory of Uncertainty Propagation [30], the mean square error and variance (when the time delays d_2, d_3 are random variables with covariance matrix (4.5)) can be computed by expanding the estimation function in the first order Taylor series:

$$e_{ms} = \sigma^2_{\hat{\theta}_{DC}} = \mathrm{E}[\hat{\theta}]{-}\theta{=}\left[\left(\frac{\partial f}{\partial d_2}\right)^2 + \left(\frac{\partial f}{\partial d_3}\right)^2 + \left(\frac{\partial f}{\partial d_2}\right)\left(\frac{\partial f}{\partial d_3}\right)\right]\sigma^2_{d_i} \tag{4.23}$$

this formula is valid around the point of expansion $(\mathrm{E}[d_2], \mathrm{E}[d_3])$ of function f in Taylor series. Expanding Equation (4.23), we have:

$$\begin{aligned} \sigma^2_{\hat{\theta}_{DC}} &{=} \left(\frac{\partial f}{\partial \eta}\right)^2 \left[\frac{d_2^2+d_3^2-d_2d_3}{d_3^4}\right]\sigma^2_{d_i} = \\ &= \frac{d_2^2(\theta)+d_3^2(\theta)-d_2(\theta)d_3(\theta)}{\left(d_2{}'(\theta)d_3(\theta)-d_2(\theta)d_3{}'(\theta)\right)^2}\sigma^2_{d_i} \end{aligned} \tag{4.24}$$

where the last equivalence is provided by the inverse function theorem. The function in (4.24) is precisely the integrand of (4.14), i.e., $I_{22}/\det(\mathrm{FIM})$, expressed in terms of DToAs $d_i(\theta)$, instead of elements $r_i(\theta)$, namely the Differences in Distance of Propagation (DDoPs).

4.4 An optimal designed three sensor-array numerical assessment

In order to validate the design procedure of the array geometry and the performance of the proposed DoA estimator, a numerical analysis was performed. The estimation functions of the two clusters of Figure (4.1) are respectively:

$$\hat{\theta}_{SC} = \text{atan}\left(\frac{d_2}{d_3}\right) \quad , \quad \hat{\theta}_{DC} = \text{atan}\left(\frac{\tan(23^\circ)(d_2/d_3 - 2)}{d_2/d_3}\right) \tag{4.25}$$

In particular, impact waves propagating in aluminium plate 1 [mm] thick (Young's modulus 70 [GPa], Poisson's coefficient 0.3 and material density 2700 [kg/m^3]) were simulated with the Greens function formalism adopted in [26]. The impulse response of a bandpass Butterworth filter (10th order) with different bandwidths and center frequencies was used in order to simulate the impact signal. The two DToAs with respect to the first sensor d_2, d_3 were computed from the simulated acquired signals by using three different estimation modalities:

1. locating the peaks of the cross-correlation ([19]);
2. by using the Gauss-Markov estimator (4.19) consisting in three cross-correlation procedures;
3. by combining the Gauss-Markov estimator (4.19) with three GCC procedures (filtering first the signals with the filter (4.20);

The last modality is the optimum one in the considered case which involves (additive) white (zero-mean Gaussian) noise (AWGN) and quasi-flat signal spectrum S in a fixed band. The power spectrum $S(\omega)$ and its band B_S for the filter (4.20) are estimated by the spectral subtraction technique.

Simulations were performed for multiple impact locations obtained by varying the true DoA with 5° steps ($\theta = -45^\circ, -40^\circ, -35^\circ, ..., 45^\circ$), the distance from the cluster center being 0.8 [m]. The results achieved by the clusters of Figure (4.1) are given in Tables (4.1)–(4.3), for different center frequencies and bandwidths of the impact signal and different peak signal to noise ratios (PSNR). To assess the Standard Deviation (SD) of DoA estimations, 200 simulations, on the entire 90°

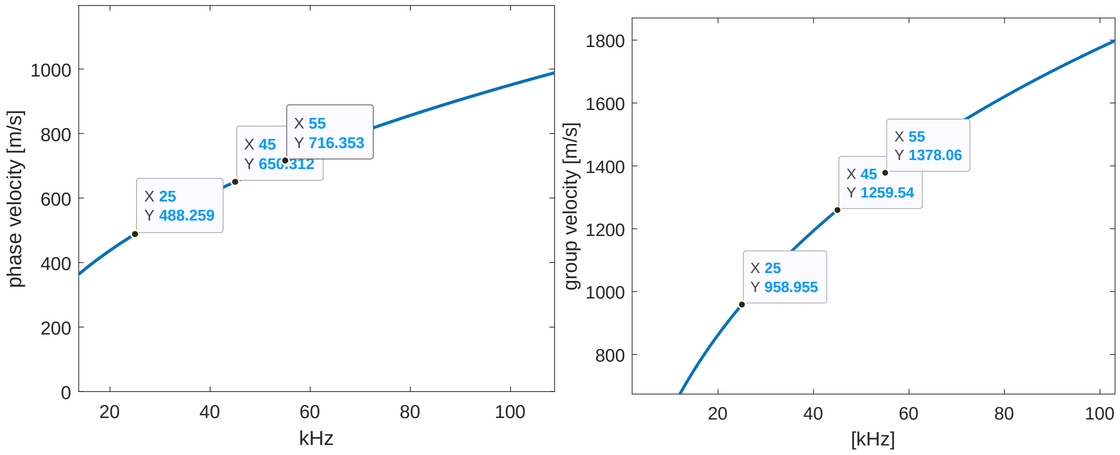

(a) (b)

Figure 4.2: A_0 mode velocities as function of frequency, in a aluminium plate (1[mm] thick). Their values at the center frequency of the bands considered for the numeric results (see Tabs. (4.1),(4.2) and (4.3)) are highlighted. (a) Phase velocity (b) Group velocity.

sector, were performed. Furthermore, the maximum error (ME) over all simulations was considered. The simulations were run simulating the propagation of the A0 Lamb mode, and considering: (i) circular piezo sensors with radius equal to 5 [mm], (ii) the radius of the array d equal to 2 [cm], (iii) sampling frequency (Fs) equal to 2 [MHz].

	Standard Cluster						**DS-Optimal Cluster**					
	CC		GM-CC		GM-GCC		CC		GM-CC		GM-GCC	
PSNR	SD	ME	SD	ME	SD	ME	SD	ME	SD	ME	SD	ME
60 dB	0.45	1.05	0.44	1.05	**0.43**	**1.05**	0.35	0.67	0.29	0.63	**0.29**	**0.63**
40 dB	0.94	3.14	0.80	3.30	**0.46**	**1.86**	0.84	2.94	0.59	1.84	**0.32**	**1.16**
35 dB	1.53	4.99	1.27	5.05	**0.52**	**1.86**	1.46	6.1	0.98	3.6	**0.37**	**1.19**
30 dB	2.50	8.13	2.14	7.50	**0.67**	**2.58**	2.35	8.8	1.62	5.82	**0.51**	**1.92**
28 dB	3.09	10.10	2.55	10.19	**0.79**	**3.48**	2.86	11.09	1.97	7.73	**0.59**	**2.25**
27 dB	3.50	12.41	2.90	12.46	**1.80**	**8.31**	3.24	10.82	2.25	7.79	**1.73**	**6.02**
26 dB	3.85	12.30	3.18	11.20	**2.74**	**10.47**	3.68	12.78	2.52	9.45	**2.09**	**7.88**
24 dB	4.78	15.30	3.98	14.44	**3.64**	**12.85**	4.57	20.67	3.1	11.17	**2.83**	**9.87**

Table 4.1: Comparison of Standard Deviation (SD) and Maximum Error (ME) values (in [Deg]) between the arrays of Figure (4.1) for noise-affected measurements at different PSNR values. Actuated pulse band: [30–40][kHz].

	Standard Cluster						**DS-Optimal Cluster**					
	CC		GM-CC		GM-GCC		CC		GM-CC		GM-GCC	
PSNR	SD	ME	SD	ME	SD	ME	SD	ME	SD	ME	SD	ME
60 dB	0.58	1.05	0.52	1.05	**0.52**	**1.05**	0.44	0.92	0.28	0.83	**0.26**	**0.83**
40 dB	1.22	4.09	1.02	4.03	**0.55**	**1.97**	1.1	4.31	0.77	2.49	**0.37**	**1.26**
35 dB	1.93	6.99	1.61	6.95	**0.63**	**2.91**	1.83	8.7	1.26	4.31	**0.44**	**2.06**
30 dB	3.31	11.22	2.72	11.05	**0.84**	**3.03**	3.03	13.41	2.11	8.58	**0.62**	**2.31**
28 dB	4.14	14.2	3.41	13.05	**1**	**4.88**	3.76	14.42	2.58	9.6	**0.93**	**3.51**
27 dB	4.52	16.04	3.72	14.96	**2.01**	**8.77**	4.26	15.55	2.93	12.2	**2.52**	**9.18**
26 dB	5.08	16.14	4.23	15.77	**3.92**	**15.97**	4.79	16.89	3.23	12.34	**2.86**	**9.79**
24 dB	6.36	21.69	5.28	20.28	**4.86**	**20.9**	5.84	20.7	4.01	15.1	**3.78**	**12.78**

Table 4.2: Comparison of Standard Deviation (SD) and Maximum Error (ME) values (in degrees) between the arrays of Figure (4.1) for noise-affected measurements at different PSNR values. Actuated pulse band: [50–60][kHz].

As shown by the Tables (4.1)–(4.3), the SD and the ME values obtained with the designed cluster are, as expected, smaller w.r.t. the SC, for PSNR values higher than 24 dB. In particular, the best performances are achieved when the optimal DoA estimator, based on the GM-GCC time delays estimator, is used. In this case, the variances almost equate to the $\mathrm{CRB}_{unknown-v}$. Due to the wave dispersion of the A0 mode, the higher is the considered center frequency, the higher is the wave (group) velocity v (see Fig. (4.2)). It is important to consider this fact because the DoA CRB in Equation (4.14) and the variance of the DoA estimator in Equation (4.24) increase as v^2. Conversely, for the case of quasi-flat signal spectrum in a given band B_S, the DToA variance term σ_d^2 of the Covariance Matrix (the CRMB in Equation ((4.5)) for an optimal estimator) decreases as B_S^2 (see (4.6)). Therefore, the two terms, wave velocity and central frequency have an opposite influence on the DoA estimation performance (see the SD values of Tables (4.1) and (4.2)). Furthermore, it can be noted that the higher is the bandwidth, the smaller is the DToA and DoA variance (compare Tables (4.1)–(4.3) which are characterized by a 10 and 30 [kHz] Bandwidth, respectively).

Finally, observe that the distance between the disk-sensors differs by the maximum radius r. This aspect has to be consider in DoA estimation performance achieved by the clusters of the Figs. (3.7),(3.9) and the clusters of the Figs. (4.1)(a)-(b). In fact, by making explicit the distance r dependence in the variance of the DoA estimator in the Eq. (4.24), observe that it decreases as r^2. The same dependence is for the variance of the DoA estimator of a SC, as it can be easily verified. Therefore, with the same other parameters values, better performance are achieved with the clusters of Figs. (4.1)(a)-(b), as expected. However, the distance r can not be arbitrarily increased for two main motivations. The first is related to the assumption that the wave-fronts impinging on the sensors cluster are to about locally planar. The farther the sensors are, the less the last assumption is satisfied. The second motivation is related to the hypothesis of low dispersion: the farther the sensors are, the more the dispersion effect negatively affects the cross-correlation procedures for the time-delays estimation.

	Standard Cluster						**DS-Optimal Cluster**					
	CC		GM-CC		GM-GCC		CC		GM-CC		GM-GCC	
PSNR	SD	ME	SD	ME	SD	ME	SD	ME	SD	ME	SD	ME
60 dB	0.35	0.85	0.34	0.85	**0.34**	**0.85**	0.45	0.72	0.4	0.72	**0.4**	**0.72**
40 dB	0.48	1.87	0.45	1.87	**0.37**	**1.42**	0.46	1.62	0.37	1.08	**0.38**	**0.72**
35 dB	0.73	2.28	0.64	2.3	**0.41**	**1.87**	0.63	2.31	0.46	1.76	**0.37**	**1.08**
30 dB	1.14	4.05	0.96	4.16	**0.48**	**1.87**	1.04	4.03	0.72	3.11	**0.38**	**1.08**
28 dB	1.35	5.1	1.15	4.83	**0.49**	**1.87**	1.25	4.69	0.87	3.15	**0.39**	**1.12**
27 dB	1.5	5.07	1.25	5.2	**0.54**	**2.14**	1.39	4.92	0.96	4.35	**0.51**	**2.08**
26 dB	1.67	5.53	1.4	5.46	**1.1**	**4.53**	1.54	6.08	1.07	3.75	**0.82**	**3.75**
24 dB	2.05	6.61	1.69	6.61	**1.59**	**6.21**	1.88	7.09	1.3	4.67	**1.2**	**4.57**

Table 4.3: Comparison of Standard Deviation (SD) and Maximum Error (ME) values (in degrees) between the arrays of Figure (4.1) for noise-affected measurements at different PSNR values. Actuated pulse band: [30–60][kHz].

Chapter 5

Directive Sensors for reverberant environments

Disclaimer: *The content of this Chapter is based upon the research work [47]: Marco Dibiase, Masoud Mohammadgholiha, and Luca De Marchi. "Optimal Array Design and Directive Sensors for Guided Waves DoA Estimation". In: Sensors 22.3 (2022), p. 780.*

In the previous last two Chapters, the problem of designing the shape and the arrangement of acoustical sensors were considered for improved performance in the DoA estimation for noise affected measurements. However, in realistic scenarios, another well-known issue arise, namely reflections and reverberation. The last ones are due to fact that the monitored structures are finite and limited by mechanical boundaries. The reverberation phenomenon is also known as multi-path propagation. In particular, reflected directive waves can be distinguished in coherent interference w.r.t the signal to be detected and incoherent signals. The first ones are due to edge-reflections of the impact/defect AE to be detected. The second ones are due to reflections produced by different impacts or acoustic events.

It is important to note forthwith that for the clusters design in the previous chapters, a restricted angles range, subset of the round angle, was considered, namely a quadrant of 90°, thanks to the structure finite size. Therefore, a sensors cluster can be placed near a plate corner. Unfortunately, in this way the sensors measurements are affected by the reflections due to the nearby edges. However, the design procedures, optimized for a DoA estimation more robust to the noise, do not lose their validity. Indeed, the used time delay estimation procedures can still rely on the cross-correlation between the pure acquired signals or the filtered ones, just exploiting the phase transform (PHAT), namely the GCC-PHAT. The last one has been shown to be a suitable alternative in reverberant scenarios [33, 34]. However, its performance can only be considered optimal for medium-high signal-to-noise ratio (SNR) values (as shown in [58]).

A different DoA estimation method, the Multiple Signal Classification (MUSIC) [59], is able to estimate up to N-1 DoAs due to different sources with N-sensor arrays. Originally designed to estimate the number and DoAs of uncorrelated signals, modified versions [60, 61] have been proposed to estimate also the DoAs of coherent signals for the multipath environment. However, with a simple 3-sensor cluster, just 2 coherent signals can be detected. This means that other directional interference may cause wrong estimations. A more robust MUSIC algorithm for reverberant scenarios is proposed in [62]. MUSIC algorithms are also limited by the assumption of accurate knowledge or estimation of wave velocity. Therefore, an additional iterative wave velocity estimation procedure is needed (as shown in [63]), which increases consistently the computational cost.

Machine Learning (M-L) algorithms [64], such as Deep Learning (DL) algorithms or Artificial Neural Networks (ANN), and sparse sensor networks can be used to better estimate the Acoustic Sources by exploiting the multiple reflections from boundaries as a supplementary information. In [65] a network of ten sparse sensors and a DL approach are employed for the damages detection from signals that are acquired over a long-time interval, where multi-modal dispersion and reverberations effects are present. Nevertheless, it is important to note that:

1. several sparse sensors are to be linked via cables or long-lasting signals are to be transferred wirelessly. As result, they are not suitable for embedded applications.

2. Supervised DL and ANN algorithms require a time consuming training phase in order to define the features which improve the estimation performance and to derive the minimum size layered structure.

3. ML estimation techniques can be onerous from computational point of view.

Despite the last two points, ML algorithms will be considered in future developments in order to understand if and when they can be considered suitable for the AS localization via multiple GWs DoA estimations on sensor arrays and embedded electronic devices.

In the work [47], Dibiase et al. provided an unconventional solution to tackle the detrimental effect of directional interference, allowing to use GCC procedures without the PHAT. Both coherent and incoherent directional interference were tackled by means of a novel directive piezo-sensor, suitable for guided propagation structures. If in the work [28], the shaping of piezoelectric transducers has already been used as a powerful means to detect DoA in non-reverberant contexts, in [47], the shaping is used to filter all undesired directional interference. Again, it is worth noting that the usage of these transducers is beneficial whenever a limited angular sector has to be monitored. Therefore, a cluster of directive-sensors was designed so that when it is placed near a plate-corner, it is able to filter the reflections of edges close to it.

The design procedure for the directive transducer proposed in the paper [47] draws inspiration from the work of Senesi and Ruzzene [2] which showed how to relate the transducer shape to its directivity. However, the transducers considered in [2] are characterized by symmetric beam patterns which are unsuited to distinguish sources related to opposite directions. To achieve this capability, a *novel complex (i.e., multi-phase) transducer* was implemented [3]. The proposed *Directive Complex Sensor* (DCS) consists of five piezoelectric patches and allows to suppress the lobes out of a 90° monitoring sector. The details of the novel directional transducer concept, a double numerical validation via GFs simulations and Finite Elements Method (FEM) simulations in terms of directivity properties and the DoA estimation performance by means of a DCSs cluster, are thoroughly illustrated in the following sections.

5.1 Directive Complex Sensor (DCS) Design

In this Section, the steps used in the work [47], to design a directive base sensor, are shown. Let pose a base sensor beam pattern is ideally equal to 1 in a given range and 0 elsewhere. Without lack of generality, we refer to the [0°,90°] range as the one where the beampattern is equal to 1. When Lamb waves are detected, the beampattern of a sensor is linked to its shape as described by the model (2.18), proposed in [66] and [2]. More specifically, the directivity properties, namely the sensor beampattern, are defined only by the Directivity function (2.20), which, in turn, is related to the geometrical distribution of the piezo-load $\phi_P(x, y)$, i.e. the *shape function*, as:

$$D_P(\omega, \theta) = \int\limits_{\Omega_P} e^{-jk_0(\omega)(x\cos\theta + y\sin\theta)} \phi_P(x, y) dx dy \tag{5.1}$$

It defines, unless than other scale factor functions (i.e., the signal spectrum $U(\omega)$, the wave-vector $k_0(\omega)$ of a Lamb wave mode and $H(\theta)$ which, without lack of generality, can be set 1), the sensor frequency response (2.18) for all possible angles of arrival θ, hence the name of Directivity function. Defining Ω_P the area of the piezoelectric path, a step shape function is equal to 1 when $(x, y) \in \Omega_P$ and 0 elsewhere.

Considering as an example a circular piezo-sensor of radius R, the (5.1) provides:

$$D_P(\omega, \theta) = 2\pi R^2 \frac{J_1(Rk_0(\omega))}{Rk_0(\omega)} \approx 2\pi R^2 \mathrm{sinc}(Rk_0(\omega)) \tag{5.2}$$

where $J_1(\cdot)$ is the first kind Bessel function of first order and $k_0(\omega)$ is the wave vector of the propagation mode of Lamb waves (e.g., A0 or S0 mode). Observe that the (5.2) doesn't depend by θ but only by frequency, so the directive properties of a piezo-disk are the same for all angles, i.e., the disk is omnidirectional. We define the base sensor beampattern at frequency ω as;

$$d(\omega, \theta) = \frac{|D_P(\omega, \theta)|}{\max_\theta \left[|D_P(\omega, \theta)|\right]} \tag{5.3}$$

For a circular sensor then $d(\omega, \theta) = 1$. As already seen in the previous Chs. (2) and (3), the Directivity function $D_P(\omega, \theta)$ (5.1) is equal to the bi-dimensional spatial Fourier Transform (2D-FT) at angle θ of the shape function. Then, the shape function which corresponds to a given desired directivity can be determined with an Inverse Fourier Transform. In our approach, we impose the same Directivity function (and so the same frequency response) of a piezo-disk of given radius in

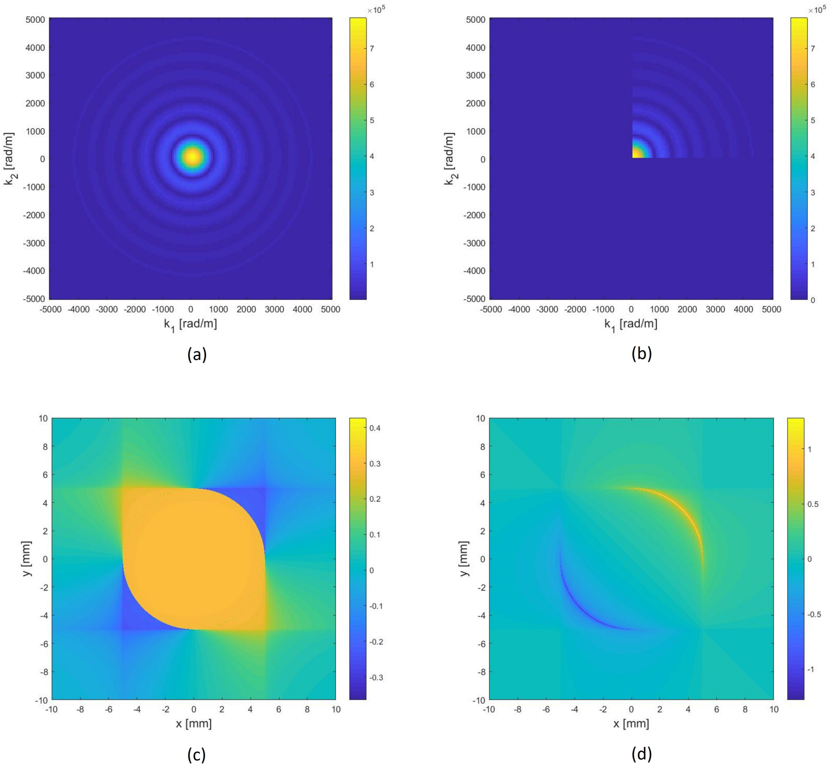

(a) (b)

(c) (d)

Figure 5.1: (**a**) Disk Directivity in k−space (|2D−FT|) (5.0 [mm] radius). (**b**) Imposed Directivity equal to that of a disk in [0°,90°] and 0 elsewhere. (**c**,**d**) Real part and imaginary part of 2D-IFT: the ideal shape functions continuously modulated.

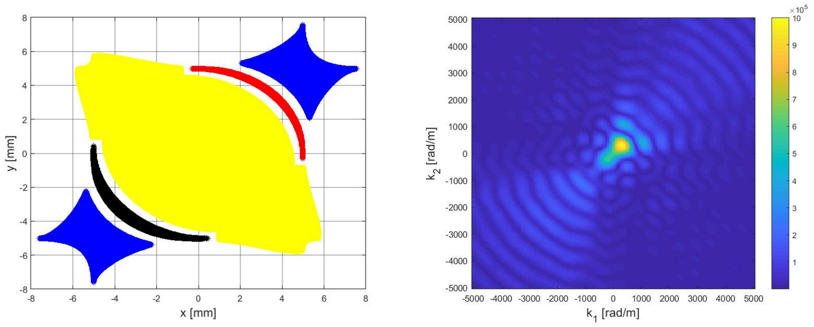

(a)

(b)

Figure 5.2: Directive Complex Sensor (DCS) designed to priviledge the [0°–90°] angular sector (**a**). The geometry of the piezopatches is generated by a quaternary phase quantization and a subsequent binary amplitude quantization of the continuously modulated shape functions illustrated in Figure (5.1). (**b**) 2D-FT of the complex quantized shape function: due to quantization procedure, it is not perfectly matched to the desired one depicted in Figure (5.1)b but it is clearly asymmetrical.

the [0–90]° angles-sector and 0 elsewhere. Therefore, we compute the 2D-FT of a disk, set to 0 all values of 2D-FT in the k-space domain between [90;360]°, and finally get back in the space-domain, via the 2D-Inverse FT (IFT) to obtain the desired shape function (see Figure (5.1)).

Note that a real shape function is achieved if and only if the Directivity function is Hermitian with respect to the origin, i.e. its amplitude is symmetric and its phase is anti-symmetric. Instead, our procedure tolerates the generation of a complex shape function, with a real part and an imaginary part, both having positive and negative values (Figure (5.1)c,d). This higher complexity allows us to have a beam pattern that is not symmetrical, i.e., without lobes in the [180:270]° range.

It is important to highlight that a complex shape function in math sense is admitted when a sensor is used for the passive monitoring, when a digital multiplication for the imaginary unit, $+j$, is allowed. Therefore, in this context, it is legitimate to refer the generated two parts as real part and imaginary one. In the following Ch. (6), because a transducer will be designed for the active monitoring, the meanings or real and imaginary terms will be clarified in detail.

Note that, as already seen for the shaped sensors in the Ch. (3), the described procedure produces a continuously modulated shape function. So, a quantization

Phase Interval	Quantized Value	Patch Color in Fig. (5.2)a
$[-\pi/4 + \pi/4)$	0	Yellow
$[\pi/4 + 3/4\pi)$	$\pi/2$	Red
$[3/4\pi + 5/4\pi)$	π	Blue
$[5/4\pi + 7/4\pi)$	$3/2\pi$	Black

Table 5.1: Phase quantization scheme used in the complex shape function implementation

procedure has to be applied to the computed shape function. In particular, firstly, the phase of the complex shape function is quantized, as detailed in the Tab. (5.1).

Then, the absolute values greater than a certain positive threshold are set to 1 and others to 0 (see Figure (5.2)). Areas associated with the same quantized values define the shape of the electrodes of the piezo patches used as sensors. A distance gap of at least 0.5 [mm] between the patches has been imposed to be compliant with the typical geometrical limitations that are associated with patch manufacturing.

Such a procedure generates the Directive Complex Sensor (DCS). As can be seen in Figure (5.2)a, such a sensor consists of five piezo patches each one depicted with a different color. It is worth noting that the two blue patches related to the quantized phase π can be short-circuited. Moreover, the three patches corresponding to the opposite phases 0 and π, i.e. the *real part*, correspond to regions where the computed shape function has almost equal absolute average value. The same applies for the two patches related to phases $\pi/2$ and $3/2\pi$ (the *imaginary part*). This implies that piezo-patches related to the real part require just one differential acquisition channel and a second differential channel is required by the patches related to the imaginary part. In order to generate the complex time-signal, a weighted sum of the two acquired differential signals has to be performed, in which the signal related to the imaginary part is multiplied by the factor $j \cdot W_{Im}$, where j is the imaginary unit and W_{Im} is a suitable weight. Finally, observe that the imposed directivity is zero in third quadrant. Therefore, for each angle θ, the frequency response is zero for the negative values of the scalar part of the wave-vector. Because the model (5.1), for an incoming Lamb wave, associates the negative wave-vector value to the positive frequency ω values and vice versa, the negative one-sided spectrum in ω has to be selected from the complex acquired signal, which is related to the positive k values. Therefore, the anti-analytic signal of the complex acquired signal is computed and used to feed the DToA estimator.

Figure (5.2)b shows the actual 2D-FT (absolute value) in the k-space domain, i.e., the 2D-FT computed after the quantization of the shape function. Due to quantization, the values of the 2D-FT, out of [0°,90°], are not 0, but are still smaller than values in the monitored angular sector.

By using Equation (5.3), the DCS sensor theoretical beampatterns were computed at different values of frequency, considering the wave vector values of A0 mode when propagating in an aluminum plate with 1[mm] thickness (i.e., for a known dispersion curve $k_0(\omega)$). As shown in Figure (5.3), useful directive beampatterns are achieved in the [10–60] [kHz] frequencies band. However, the best directional behavior is achieved in the [30–60] [kHz] frequency range.

The directivity properties at each frequency can be expressed by the Average Directional Attenuation (ADA) parameter. It is computed by the beampatterns values, as the ratio between the average beampattern value in the monitored angular sector (i.e., [0–90]°) and out of that one. In Figure (5.3), the ADA values for different frequency values are shown. The ADA value is above 8.3dB in the [10–60] [kHz] band, and 13.0dB in the [30–60] [kHz] band.

Regarding the W_{Im} parameter, in order to find an optimal value a suitable cost function $J_{W_{\mathrm{Im}}}$ was defined:

$$J_{W_{\mathrm{Im}}}(W) = \frac{1}{N}\sum_{i=1}^{N} \frac{\varsigma(W, k_i)}{DA_{\alpha}^{\beta}(W, k_i)} \tag{5.4}$$

where k_i are N wave-numbers in the considered (spatial) spectral region, $DA_{\varphi}^{\gamma}(W, k_i)$ is the directional attenuation at angle φ w.r.t the one at angle γ and $\varsigma(W, k_i)$ is equal to highest sidelobe level of beampatterns at each frequency k_i. By minimizing $J_{W_{\mathrm{Im}}}$ for $k_i = 353, 409, 459, 505[rad/m]$ (corresponding to the frequencies $f_i = 30, 40, 50, 60[kHz]$ of the A0 mode in the considered setup plate), $\varphi = 120°$ and $\gamma = 90°$, the value $W_{\mathrm{Im}-Opt} = 6.81$ is obtained. It is worth noting that the DA of the proposed DCS is sufficiently high to mask directional interference in a given angular range $[\psi_1, \psi_2]$, subset of [90°,360°]. For example, the DA is above 11.3 dB within [30–60] [kHz], for all undesired DoAs within [130–320]deg. This is due to DCS beampattern non-idealities, in particular to the non-sharp mainlobe cut-off near 0° and 90°. The DCS DA is also limited by the highest sidelobe level. The previous facts justified the cost function (5.4).

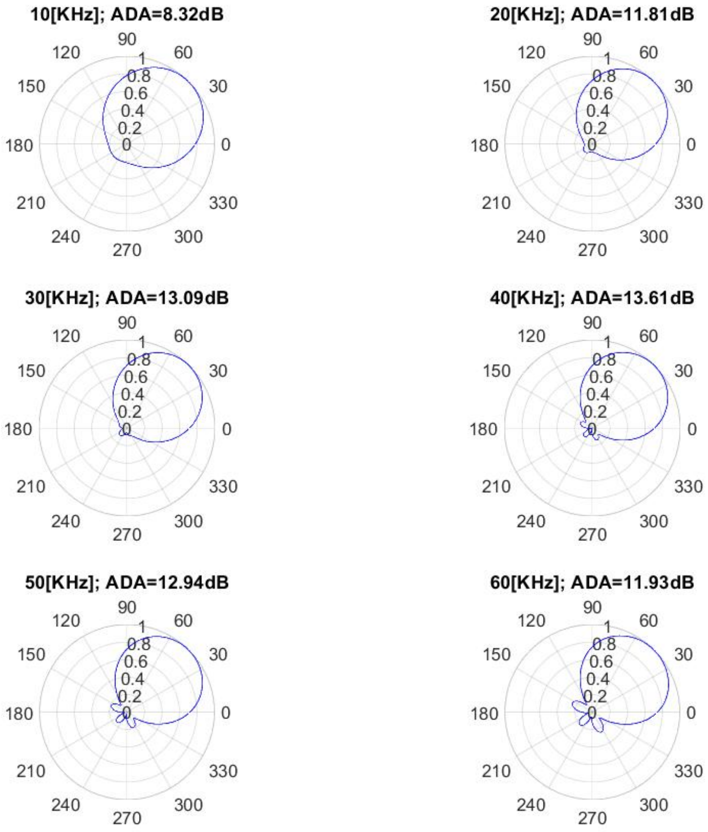
10[KHz]; ADA=8.32dB

20[KHz]; ADA=11.81dB

30[KHz]; ADA=13.09dB

40[KHz]; ADA=13.61dB

50[KHz]; ADA=12.94dB

60[KHz]; ADA=11.93dB

Figure 5.3: The DCS beampatterns computed at 6 different values of frequency when A0 mode propagating an aluminium plate (1 [mm] thick) and corresponding Average Directional Attenuation (ADA) values.

Such non-idealities can be attributed to the detrimental effect of binary quantization. More specifically, the DCS shows the better directivity properties in the wave vector k values range [353–505] [rad/m] (corresponding to the 30–60 [kHz] beampatterns shown in Figure (5.3)). It is worth noting that the relationship between wave vector function and frequency $k_0(\omega)$ depends on the monitored structure characteristics (material, thickness, etc.). In other words, the optimal frequency range of the DCS can be found by taking into account the dispersion curves of the monitored medium.

5.1.1 Green's functions and FEM simulations assessment

In order to validate the design procedure and the directivity properties of the DCS, in the following subsections, the beampatterns obtained from the GFs formalism and FEM simulations are shown and compared with the theoretical ones (see Figure (5.3)).

Beampattern assessment via GFs simulations

As first, Gfs simulations, already used to assess numerically the DoA estimation performance via the optimized shaped sensors (Sec. (3.1.3)) and the cluster of optimized displacement disk-sensors (Sec. (4.4)), were performed on an Aluminium plate, 1[mm] thick. The GFs numeric model was ran on the Matlab software [67]. Multiple impact locations were used by varying the DoA with 5° steps and by covering the entire round angle. An impact distance from the sensor equal to 0.8[m] was considered. The impulse response of the Butterworth filter (10° order) with the cut-off frequencies equal to 10[kHz] and 80[kHz] was used in order to compute the beampatterns to any desired frequency within the filter band. A sampling frequency equal to 1[MHz] was used. Therefore, the simulated signals, acquired by each single DCS patch were summed according to the theoretical model: the two differential signals acquired by the real part and the imaginary one were summed after multiplying the last one by the factor $j \cdot W_{Im}$. Therefore, the one-sided amplitude spectrum of the complex signal was used to generate the beamptterns at different frequencies, according to Eq. (5.3). Observe that only the spectrum of the negative frequencies has to be selected, according to Directivity model (2.20), which associates the positive frequencies ω to the negative wave vector $-\mathbf{k}_0(\omega)$. The GFs simulations beampattern and the theoretical ones at 4 different frequencies are shown in Fig. (5.4).

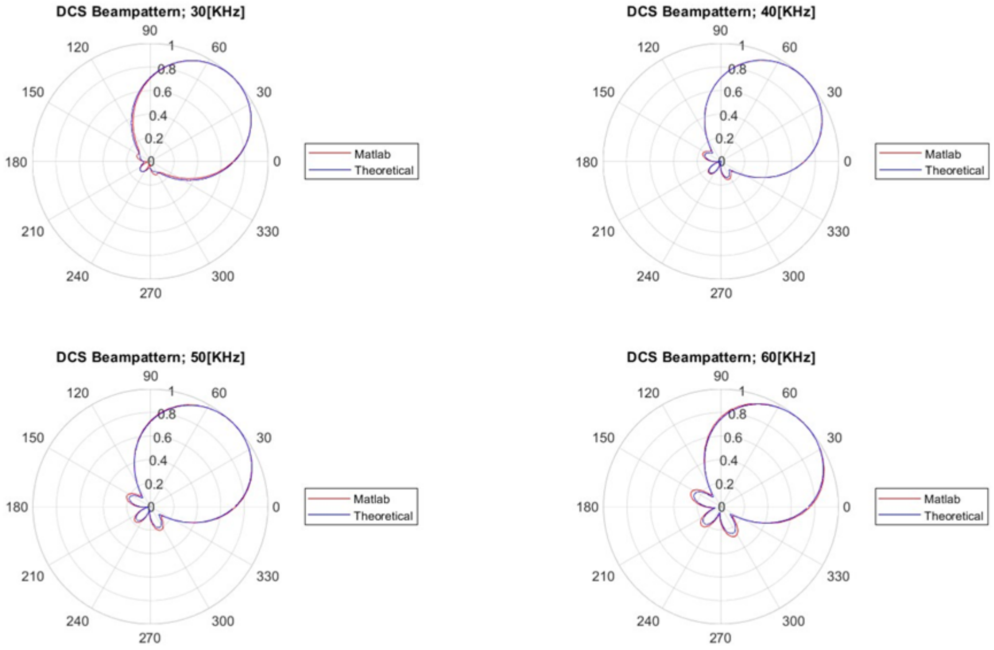

Figure 5.4: Comparison of the GFs simulations and theoretical beampatterns computed at 4 different frequencies.

Finite Element Simulation using COMSOL Multiphysics

To further validate the DSC performance, the theoretical beampatterns predicted by the model have been compared with the ones resulting from finite element (FE) simulations. The last ones were performed particularly by the PhD candidate Masoud Mohammadgholiha, in the context of joint research efforts, conducted step by step, in order to achieve the desired beampatterns matching. Therefore, the designed DCS was transposed in a three dimensional Comsol FE model. In the numerical model, an aluminum plate with dimensions of 500 [mm] × 60 [mm] and thickness 1 [mm] was chosen as the propagation medium. Since it is sufficient to shape just one metalization of the DCS (top or bottom) to achieve the desired directive behavior, the DCS was modeled using the geometry obtained in the design procedure, below which a small disk of piezoelectric material with a radius of 6 [mm] was defined. Then, the DCS was attached to the plate as shown in Figure (5.5).

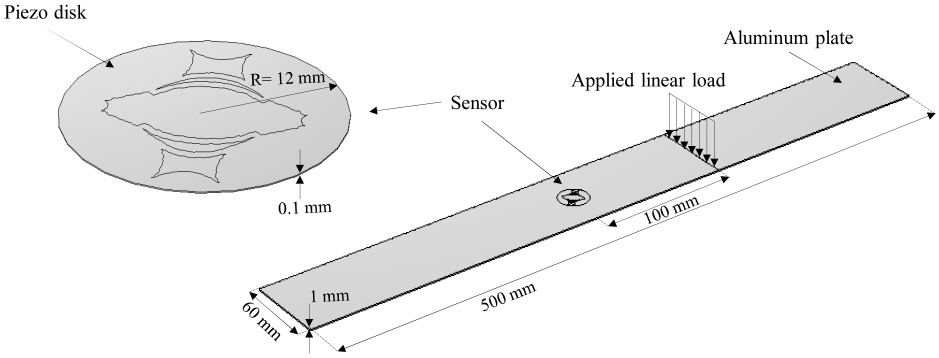

Figure 5.5: Three-dimensional geometry of the model.

The excitation for the A0 mode was simulated using a line load in a way that a plane wave is generated within the plate. It should be noted that the excitation signal is considered as a sine-wave with a combination of four different frequencies of 30, 40, 50 and 60 kHz. Unlike the common procedure to compute the directivity pattern, which includes a number of point sources around a fixed transducer, a different approach was utilized here: at each simulation run, the sensor was rotated of 5 degrees, while the excitation load was fixed, as depicted in Figure (5.5). The motivation of using such a method was to reduce the computational cost of the numerical model. Furthermore, in order to prevent wave back-reflection at side boundaries, the Low-Reflecting Boundary option was utilized. Two physics, Structural Mechanics and Electrostatics were coupled by the Multiphysics-Piezoelectric Effect to take the solid mechanics of the aluminum plate and the electrical feature of the piezoelectric sensor into consideration.

The simulation results including the sensor response and the generated wavefield at different times for $\theta = 0$ are given in Figures (5.6) and (5.7), respectively. The beam patterns obtained from the FE simulation are compared to that of the theoretical model in Figure (5.8). A notably good agreement between them is observed, indicating the effectiveness of the proposed complex sensor.

Furthermore, the matching of the beampatterns provided by the theoretical model and by both the GFs simulations and FEM simulations, involves that the two simulations methods provides the same results at least in terms of beampatterns. As result, the time required to perform

simulations of piezo-sensors response, when GWs propagate, can be drastically reduced thanks to the GFs simulator. It is important to highlight that the key point to achieve the previous result was to consider each shaped patch as a capacitor, whose voltage, in the COMSOL software [68], can be computed as the integral of the charge density, divided for the capacitance. Therefore, just the shaped electrodes can be considered for the voltage measure.

In practical terms, for piezoelectric sensors voltage reading, analog charge amplifiers (namely, current integrator circuits), such as those proposed in the works [69, 70], can be used. Theoretically, it is possible to use voltage amplifiers, but in many cases it's not the preferred solution. The problem is given by the stray capacitances. Indeed, the input impedance of a charge amplifier circuit is almost zero because of the Miller effect. Hence all the stray capacitances (the cable capacitance, the amplifier input capacitance, etc.) are virtually grounded and they have no influence on the output signal.

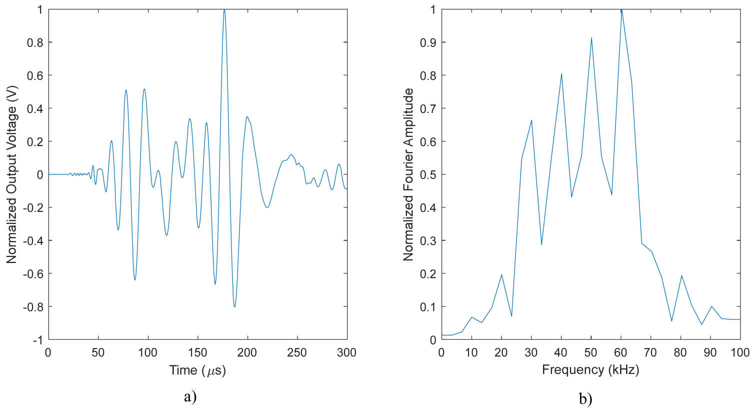

Figure 5.6: Sensor response for $\theta = 0$: (**a**) time plot and (**b**) frequency spectrum.

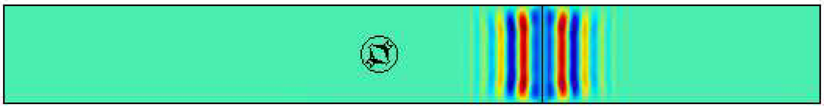

t= 20 µs

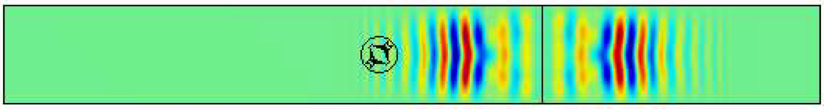

t= 50 µs

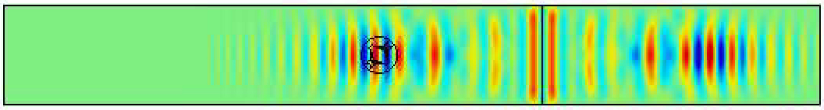

t= 90 µs

Figure 5.7: The generated wave field at different times for $\theta = 0$.

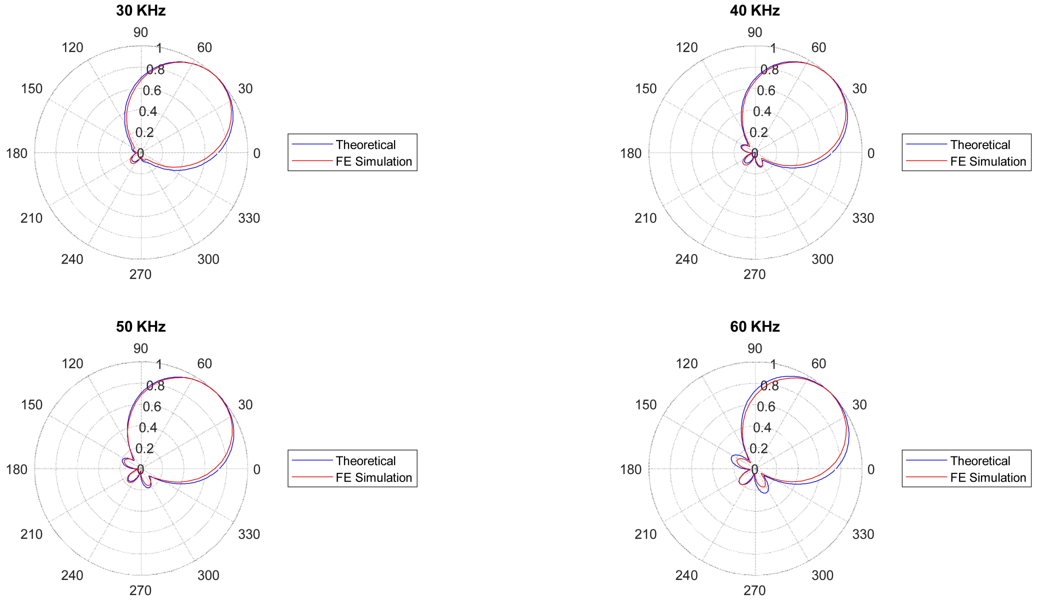

Figure 5.8: Comparison of the FE simulation and theoretical beampatterns computed at 4 different frequencies.

5.1.2 DoA estimation performance in reverberant environments

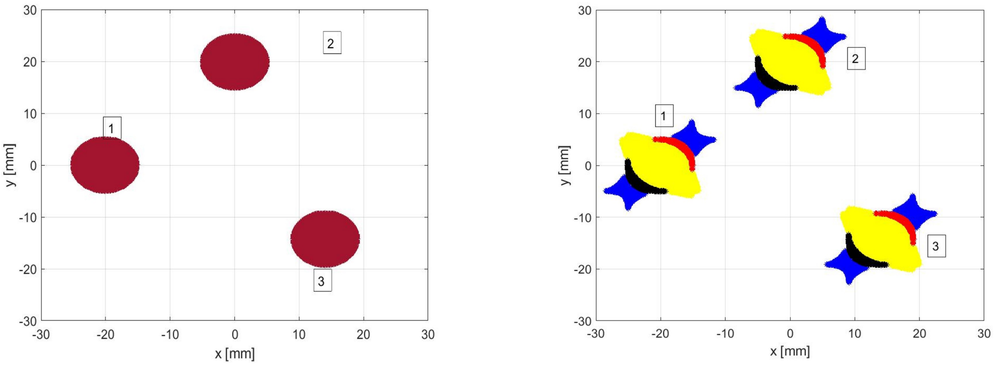

(a) (b)

Figure 5.9: The Designed Clusters (DC) of Disk sensors (**a**) and of DCSensors (**b**) (rotated by 45º compared to Figure (4.1)b) for an optimal DoA estimation in [0–90]°.

As already discussed, in realistic reverberant environments, coherent reflections and incoherent reflections may hamper the DoA estimation. This interference can be viewed as waves generated by virtual *Image Sources (ISs)*, due to the mirroring produced by the boundaries of the monitored structure [71]. In the most general case, undesired AE is given by multiple ISs. Let us suppose that the AS signal is corrupted by undesired reflections due to an edge closely spaced w.r.t. the sensor cluster, as shown in Figure (5.10). In this example, the AS is placed in the position specified by the blue circle (DoA equal to 90°), while Edge 1 generates an IS (IS_1) which, in turn, generates coherent interference on the signal acquired by the DCS cluster.

Additional incoherent interference may be generated by ISs of previous acoustic events. Both coherent and incoherent directional interference could have a detrimental effect on DoA estimation. Improved DoA estimation performance is achieved when the DoAs of ISs occur in angular ranges $[\psi_1, \psi_2]$ filtered by the beampattern of the DCS, which ensures a minimum DA level.

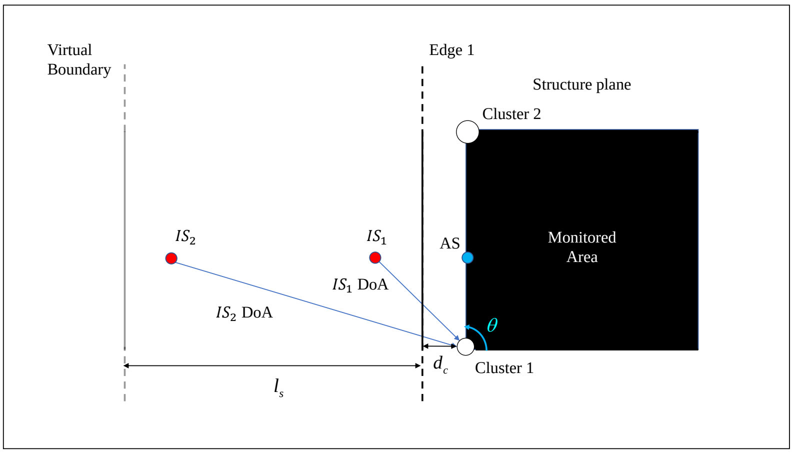

Figure 5.10: Example of directional interference due to edges reflections. IS_1 represents a coherent interference due to the edge reflection of the AS to be detected, whereas IS_2 represents an incoherent interference due to another acoustic source.

In order to evaluate the DoA estimation performance of DCS clusters in realistic simulation setups, the cases of coherent and incoherent reflection interferences are considered. For both cases, in the [0–90]° angular-sector, the wave to be detected were simulated by changing their orientation with a step of 5°.

At first, coherent interference was simulated, the cluster was placed at $d_c = 17$ [cm] from the edge, whereas the AS location distance was set equal to 40 [cm]. The directional interference IS_1 is produced by the mirroring of the AS induced by edge reflections (see the Figure (5.10): the AS DoA is equal to 90°, whereas the corresponding IS_1 DoA is equal to 130.36°). Considering a sampling frequency f_s equal to 2 [MHz], a 200 samples Tukey window (i.e., a rectangular window with the first and last 47.5 percent of the samples equal to parts of a cosine) filtered by using a Butterworth filter (10th order) with a bandpass equal to [30–40] [kHz] was used as impact signal and as IS.

Considering the Design Array configuration depicted in Figure (5.9), the DoAs estimated by the processing of the simulate response (via the GM-GCC time delays estimator) of piezo disk-sensors and DCSs, together the actual AS DoA and the corresponding IS DoA for 19 different simulated angles cases are reported in Table (5.2). In these conditions, the Standard Deviation and the Maximum Error values are equal to 18.48 deg and 70.76 deg for the piezo-disk cluster, and 1.47 deg and 3.33 deg for the DCSs cluster, respectively.

Two examples of acquired time signals, distinguishing the signal component related to the wave to be detected and the reflection, on a piezo Disk and on a DCS for the same DoAs are illustrated in Figure (5.11) (more specifically, for the DCS, the anti-analytic real part of the complex time signal is plotted). As can be seen, the AS signal and the IS signal are overlapped in time, hence a very unfavorable condition for DoA estimation. However, the DCS clearly shows the capability to strongly attenuate the spurious component.

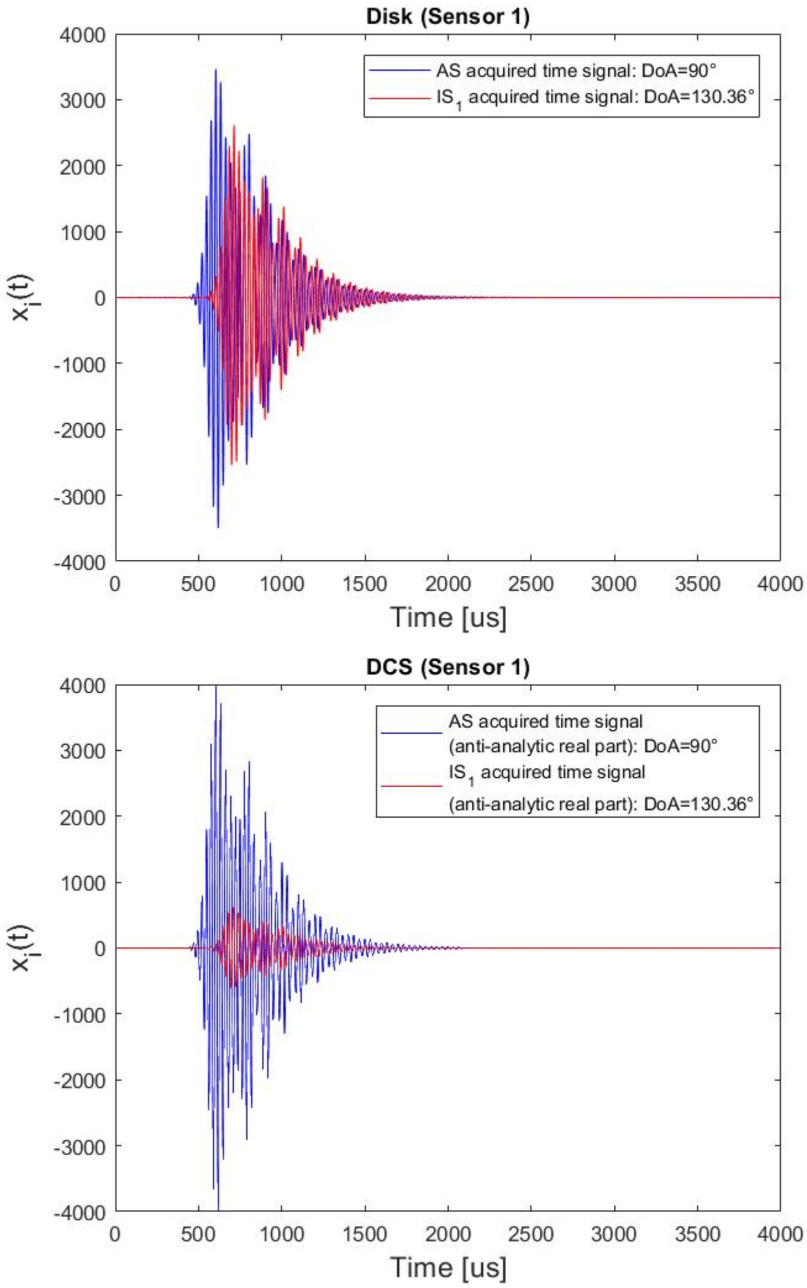

Figure 5.11: Superposition of two acquired signals: the AS to be detected, and the coherent edge-reflection due to an IS, when (top plot) the sensor is a Disk, and (bottom plot) a DCS. Impact distance d = 40 [cm]; Cluster distance from the edge $d_c = 17$ [cm].

In order to assess the DoA estimation performance in even more challenging conditions, the case of measurements affected both by directional interference and diffuse noise (AWGN) was considered. 200 simulations of AWGN, on the entire 90° sector, were performed for different PSNR values. The Standard Deviation and the Maximum values are given in Table (5.3).

Then, we considered the case of an additional incoherent interference with random DoA in the angular-sector ([169.69–180]°) (to simulate an undesired incoherent component due to an IS_2 of a previous impact/defect).

In particular, we have simulated AS and incoherent spurious waves impinging on the sensors simultaneously, because these are the most critical conditions to perform the DoA estimation. The impulse response of a [30–40] [kHz] band Chebyshev Type I filter (10th order with a passband ripple of 4 dB) with a 3dB amplification (to simulate a high energy impact) was used as actuating signal of the incoherent component.

The DoA estimation results in the presence both of a coherent and incoherent interference by means of the cluster of disk sensors and DCSs (Figure (5.9)), for 19 different simulated cases are reported in Table (5.4). The Standard Deviation and the Maximum Error values are equal to 31.4 deg and 67.3 deg for the piezo-disk cluster, and 2.03 deg and 5.22 deg for the DCSs cluster, respectively. Three examples of acquired time-signals, distinguishing the signal component related to the wave to be detected and the spurious ones, on a piezo Disk and on a DCS for the same DoAs are given in Figure (5.12). Also, in this case, the spurious components are strongly attenuated by the directional sensor.

		Disks	**DCSs**			**Disks**	**DCSs**
		GM-GCC	**GM-GCC**			**GM-GCC**	**GM-GCC**
AS	IS	Estimated	Estimated	AS	IS	Estimated	Estimated
DoA	DoA	DoA	DoA	DoA	DoA	DoA	DoA
0	180	2.71	$-\mathbf{0.93}$	**50**	160.27	60.14	**49.85**
5	178.24	3.93	**3.93**	**55**	157.7	46.95	**56.98**
10	176.48	11.01	**9.19**	**60**	154.91	53.05	**58.91**
15	174.68	16.14	**14.94**	**65**	151.87	66.43	**66.18**
20	172.86	22.81	**19.58**	**70**	148.51	72.26	**73.16**
25	170.98	27.23	**25.52**	**75**	144.77	97.54	**74.07**
30	169.04	28.96	**30.34**	**80**	140.56	91.82	**82.38**
35	167.02	30.71	**36.31**	**85**	135.8	14.23	**83.89**
40	164.9	37.06	**40.15**	**90**	130.36	104.67	**93.33**
45	162.66	47.31	**45.95**	-	-	SD 18.48	SD 1.47
						ME 70.76	ME 3.33

Table 5.2: Comparison of DoA estimation performance between the two arrays depicted in Figure (5.9) for measurements affected by a coherent edge reflection due to an Image Source (see Figure (5.10)). In the table, the nominal DoA value, the direction of the interferring source, and the estimated values are reported in degrees (ASs band: [30–40] [kHz]; Impact distance d = 40 [cm]; Cluster distance from the edge $d_c = 17$ [cm]).

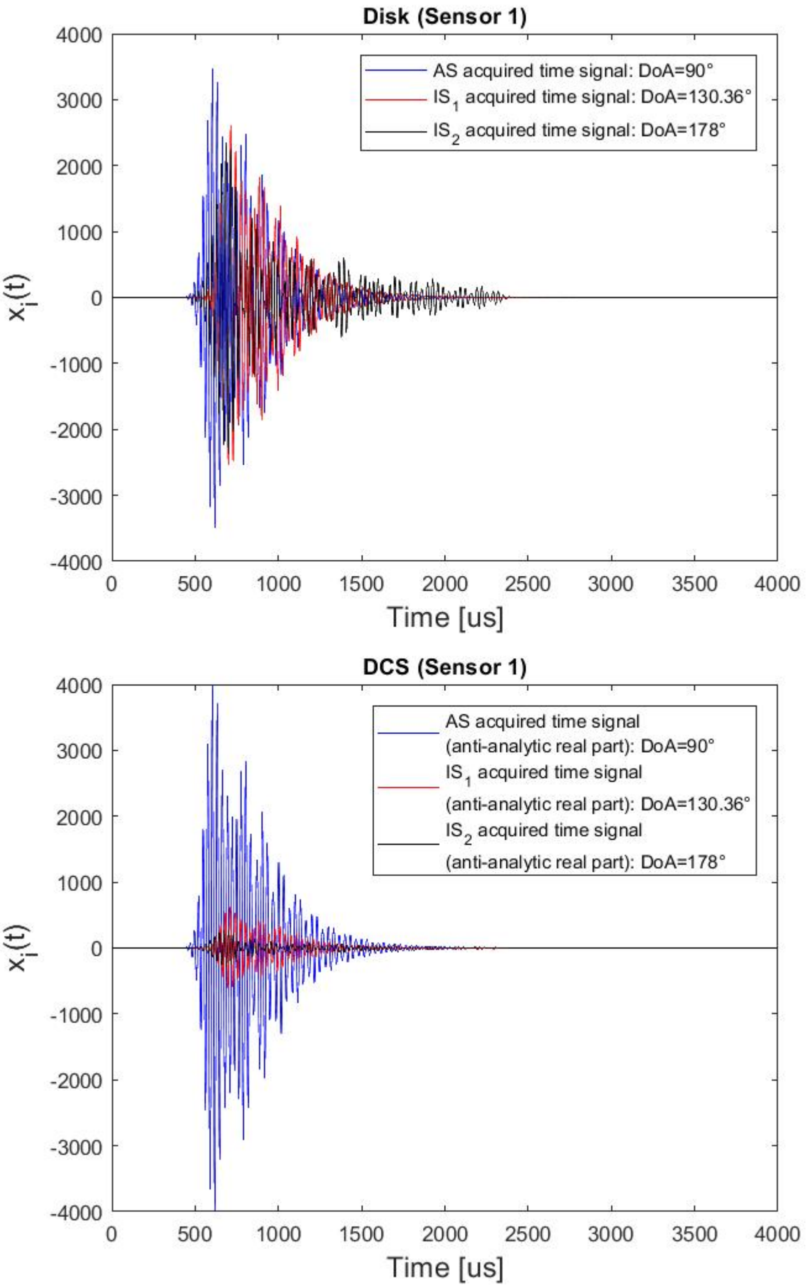

Figure 5.12: Superposition of three acquired signals, the AS to be detected and to two undesired components (coherent and incoherent interference due to two ISs of the current AS and the AS of a previous impact/defect), when the sensor is a Disk (top plot) and a DCS (bottom plot).

PSNR	60 dB	30 dB	20 dB	15 dB	10 dB	9 dB	8 dB	7 dB
SD	*1.5*	*1.52*	*1.65*	*1.9*	*2.47*	*2.63*	*2.85*	*3.11*
ME	*3.33*	*4.58*	*5.69*	*6.69*	*9.24*	*9.57*	*11.91*	*12.99*

Table 5.3: DoA estimation performance (SD and ME in degress) for the DCS cluster shown in Figure (5.9)) when the measurementes are affected by a coherent edge reflection (simulation setup of Table (5.2)) and diffuse noise (AWGN).

			Disks	**DCSs**				**Disks**	**DCSs**
			GM-GCC	**GM-GCC**				**GM-GCC**	**GM-GCC**
AS	IS	IS-2	Estimated	Estimated	AS	IS	IS-2	Estimated	Estimated
DoA	DoA	DoA	DoA	DoA	DoA	DoA	DOA	DoA	DoA
0	180	178	16.66	**−2.03**	**50**	160.27	171	69.3	**49.85**
5	178.24	179	7.62	**5.42**	**55**	157.7	179	28.44	**58.49**
10	176.48	171	17.76	**10.07**	**60**	154.91	179	116.24	**58.91**
15	174.68	179	32.01	**15.4**	**65**	151.87	175	20.26	**68**
20	172.86	176	29.71	**20.23**	**70**	148.51	178	83.38	**73.16**
25	170.98	171	30.2	**25.38**	**75**	144.77	171	83.52	**73.62**
30	169.04	172	23.41	**28.9**	**80**	140.56	174	27.38	**81.15**
35	167.02	175	25.85	**34.42**	**85**	135.8	179	17.65	**79.78**
40	164.9	179	61.1	**40.15**	**90**	130.36	178	110.89	**92.33**
45	162.66	179	92.82	**46.87**	-	-		SD 31.49 ME 67.35	**SD 2.03** **ME 5.22**

Table 5.4: Comparison of DoA (in degrees) estimation performance between two designed arrays (Figure (5.9)) for measurements affected by a coherent edge reflection due to an IS (see the IS_1 in the Figure (5.10)), and a incoherent spurious signal due to a second IS of a previous impact/defect with a random DoA within the range [169–180] (see the IS_2 in the Figure (5.10)). AS and ISs band: [30–40] [kHz]; (Impact distance d = 40 [cm]; Cluster distance from the edge d_c = 17 [cm]; Structure length l_s = 1.1 [m]).

Finally, the DoA estimation performance was evaluated when the measurements are affected also by diffuse noise (AWGN). 200 simulations of AWGN were performed for different PSNR values. The Standard Deviation and the Maximum values, shown in Table (5.5), clearly validate the ability of the DCS to cancel out *multiple* *spurious interferences.*

PSNR	60 dB	30 dB	20 dB	15 dB	10 dB	9 dB	8 dB	7 dB
SD	*2.04*	*2.04*	*2.13*	*2.53*	*3.38*	*3.54*	*4.26*	*4.04*
ME	*5.22*	*5.67*	*7.14*	*9.28*	*13.15*	*16.07*	*16.04*	*18.05*

Table 5.5: DoA estimation performance (SD and ME in degress) by means of a DCS designed cluster (Figure (5.9)) when the measurements are affected by a coherent edge reflection and an incoherent one (simulation setup of Table (5.5)) and diffuse noise (AWGN).

It is worth noting that the analyzed configuration is representative of many realistic scenarios. In all the considered cases, there is a clear advantage in the performance achieved by the DCS cluster with respect to the conventional piezo disks. The performance of the DCS is, however, degraded when the ISs and the AS to be detected are generated at closely spaced locations. This is due to the fact that the directional selectivity of the DCS is not perfect, and, in case of interferences whose direction of arrival is slightly larger than 90° or slightly less than 0°, the attenuation is poor.

It is also worth noting that the proposed DCS cluster provides good results in DoA estimation both for coherent and incoherent directional interference even for low PSNR values because the DoA estimator (4.25), based on the GM-GCC estimator, is the optimal estimator in presence of noise, for any SNR value. Viceversa, the GCC-PHAT signal processing is useful just for medium-high SNR values because is based uniquely on the signal phase information. Furthermore, the DCS sensors allow to work on all signal time-lapse, whereas the commonly-adopted selection of smaller time windows reduces the DoA estimation accuracy, in particular when the non-impulsive and long-lasting signal is to be detected.

5.1.3 DCS conclusions

In order to filter out directional interference, such as edge reflections, a novel directive passive sensor was designed to replace the piezo-disks which are conventionally adopted in this application field. The novel sensor exploits its shape as a means to attenuate spurious waves coming from directions that are not included in the monitored angular sector. It consists of five-piezo patches whose output is collected by two differential channels. The new sensor is able to filter directional interference in a known k wave vector bandwidth ([353–505] [rad/m]). In this band, the average attenuation for spurious waves is 12.89 dB. Future developments are aimed to use improved quantization procedures to achieve even better directivity properties in a larger bandwidth and to provide experimental results of the proposed DCS concept in different practical scenarios.

Chapter 6

Active Monitoring

6.1 Acoustic-Ultrasound techniques: Background

In the previous Chapters, some strategies and unconventional solutions were proposed and numerically validated in the passive SHM context in order to address typical issues, such as noise and reverberations. Passive SHM allows the real time monitoring to detect and localize impacts or damages growths, via Acoustic Emissions (AE). However, passive techniques may not detect all damages because defects growth could not generate AEs, if the strucuture is not subjected to loading or the AEs energy is not sufficient to be detected.

The complementary technique, namely, the active monitoring, allows to inspect a structure on-demand. In this way, undetected damages via passive techniques, can be identified and located. Observe that fixing a sharp dividing line between the two methods is erroneous. Indeed, they can be combined by using transducers in active way and, at the same time, sensors in passive one, to acquire the echoes due to potential defects.

As background of the active ultrasound SHM, in the next Sections will be illustrated two conventional solutions, which can use piezoelectric transducer, bonded to the monitored structure, to interrogate a structure and detect potential defects.

6.1.1 Interdigital Transducers

Interdigital piezoelectric transducers are used to generate ultrasonic waves and inspect metallic or composite plates. They can be used in the *pitch-catch* method, by using two transducers acting respectively as transmitter and receiver, or in the *pulse-echo* method, when an interdigital transducer is used both as transmitter and receiver. The interdigital transducers have a fixed operating frequency which is dictated by the interdigital spacing among multiple piezo-loads. GWs can be excited to cover large distances. Rectangular piezo-wafer active sensors can be used with their lengths oriented along the axis of a beam. This ensures that a Lamb waves were predominantly excited along the beam length, according to the directivity model (2.20) and a rectangular load shape function. In [72], Capineri L. and Bulletti A. showed that it's possible to control the mainlobe-width of Interdigital Transducers even via the inclination of the electrodes which compose an interdigital transducer. The ability to detect cracks was experimentally proved both in metallic plates [73] and in composite ones [74] by using both the A_0 mode at low frequency and the S_0 one, so that the wavelength is sufficiently smaller than the crack to be detected. However, the main limitation of interdigital transducer is related to its fixed directionality. In order to obtain a mobile detection directionality, phased arrays can be used, as shown in the following Section.

6.1.2 Phased Array

Phased Arrays are a well-known and investigated solution for radar, sonar and medical ultrasound systems, to excite directional waves. The beam steering is achieved through constructive/destructive interference between multiple emitting/receiving elements. The last physical behavior is obtained by exciting multiple elements with appropriate phases so that focused waves are transmitted. The previous procedure is commonly referred to as *beam-forming* or *delay-and-sum* technique. In the GW SHM context, Deutsch et al. [76] developed a phased-array self-focusing method, by which the delay times are adjusted to focus the beam exactly on the defect. However, for the multiple defects localization, the technique allows to focus just the defect that produces the largest backscattered signal. Additionally, phased-arrays can exploit tomography techniques. Schwartz et al. [77] proposed a Lamb wave

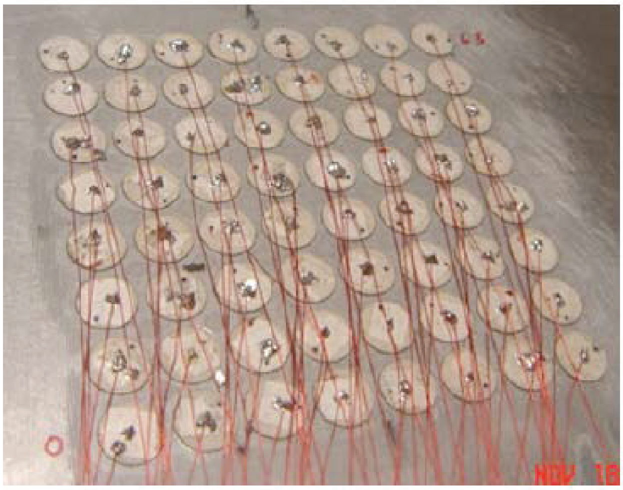

Figure 6.1: A SHM phased array setup example (it was investigated in [75])

ultrasonic tomography imaging system for aircraft structural health assessment. The simulated results showed that the method could accurately determine the dimension, shape, and location of defects. However, a higher computational cost is required. Giurgiutiu and Bao [78] proposed the Embedded Ultrasonic Structural Radar (EUSR) to avoid an heavy and complex multichannel phased excitation equipment. However, the proposed technique assumes that just a monochromatic signal is excited, to satisfy the non-dispersive hypothesis (i.e., a constant wave velocity). However, long-lasting sinusoidal waves using can implicate ambiguity issues in presence of multiple defects echoes. Vice versa short-time sinusoidal waves at high frequency can implicate a poor radial resolution due to the very high wave velocity. As shown in Fig. (6.1) (an experimental sensors-arrays investigated in [75]), in order to reduce the mainlobe beamwidth, phased arrays typically require a large number of sensors. This involves an wiring increasing as well as multiplexing circuitry one. Further issue is related to the intensive signal processing on a large amounts of recorded data. As conclusion, the phased array solution, due to the large number of requested sensors, the sensors-system weight, a high installation cost, the hardware complexity and a significant computational cost, is often unuseful for embedded applications, such as aeronautical or aerospace ones.

6.1.3 F-SAT: a single piezo-transducer for on-demand inspection

As already seen in the Chapter (5), the directivity model (2.20) for a piezo-sensor, provides the possibility to design a single piezo-load to obtain the desired directive properties. This chance can be used also to design Transducer for the active monitoring. Senesi and Ruzzene, in [2], used this opportunity to design a spiral Frequency Steerable Acoustic Transducer (F-SAT), in order to detect and localize cracks with a broadband acoustic behaviour. The Directivty function was designed so that at each wave-vector value and, via the dispersion curve, at each excited frequency, ideally, corresponds a scanning direction or angle. The basic idea is schematically illustrated in the Fig. (6.2). In [79], Senesi et al. achieved a feasible F-SAT constituted by two parts to consider both the negative and positive shape function values. In particular, a binary quantization procedure was used so that all piezo-values higher than a positive threshold are set to 1, and all ones lower than a negative threshold are set to -1. Furthermore, in [79], an experimental validation of the design procedure and the F-SAT ability to scan different directions was provided. However, the design criterion shows some limitations in the damages detection and localization tasks. In fact, an intrinsic trade-off between the distance and angle estimation accuracy can be observed: due to the fact that the beam steering is obtained as a simple function of the excited frequency, the broader is the frequency content of the excited pulse the wider is the uncertainty for angle estimation. Vice-versa, as will be shown better in the following Sections, the range evaluation requires broadband excitation signals to increase its estimation accuracy, as well known in Radar antennas Theory ([80]). Short sinusoidal waves (e.g. just one sinusoidal cycle) could be excited, in order to increase the distance resolution. However, if the condition $\tau >> 1/f_c$ is not satisfied (i.e. a signal filtered by $\delta(f_c)$), where τ is the signal time duration and f_c is the excited frequency, spurious frequencies are generated with a consequent undesired bandwidth increase, namely a wide mainlobe aperture. If the sinusoidal pulses are time-windowed, undesired spectral components are excited around the central excitation frequency.

In addition, it is important to observe that the angular accuracy is relatively poor even when long-lasting and narrowband pulses are actuated (not to mention

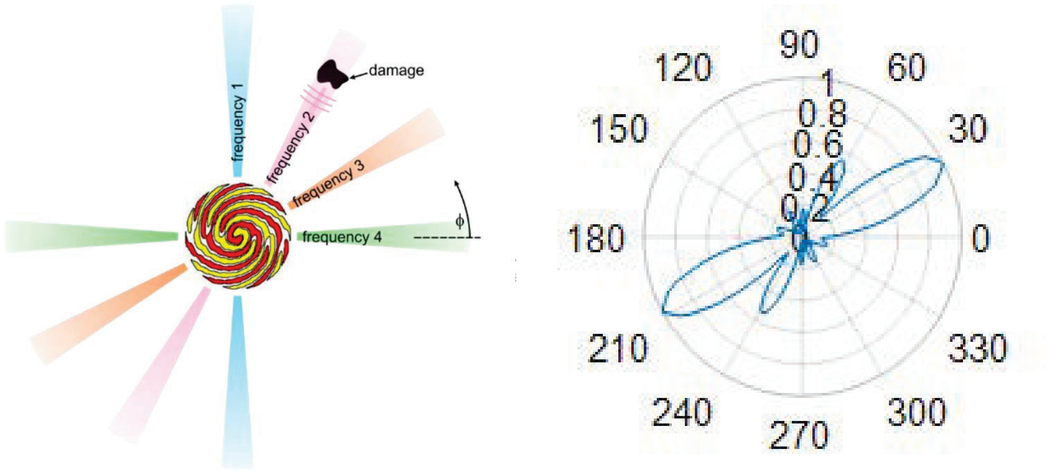

(a) (b)

Figure 6.2: (a) The basic idea of F-SAT Transducer (proposed in [2]): at each scan direction corresponds a different excitation frequency (b) A beampattern example: both the DoA 30° and the 30°+180° are scanned for an appropriate excitation frequency. Due to the wide mainlobe aperture, a poor angular resolution is achieved.

the associated issues in terms of ambiguity in presence of multiple defects). This is due to the fact that the achieved directivity, with a limited-size Transducer, associates at the same frequency multiple angles. Therefore, the mainlobe (half-power) aperture is wide and approximately equal to 18°, as shown in the work [81].

Finally, another issue is related to the 180° ambiguity in the DoA estimation: the F-SAT was designed so that it is impossible to determine whether a wave is received from angle θ or $\theta + 180°$. Similarly, in actuation waves are transmitted simultaneously in opposite directions. A suitable design procedure to avoid the 180° ambiguity, and a more convenient design criterion to overcome the limited localization performance is discussed in this Chapter.

In the next Section, the design procedure will be introduced and redefined to excite and acquire directional waves along just one direction. Then, in the subsequent Sections a novel Transducer will be illustrated.

6.2 A generalized shape design procedure for directional GWs

As previously seen in Chapter (5), a novel Sensor (proposed in the work [47], referred as DCS, was already designed to detect guided waves propagating along a single direction, avoiding the 180° ambiguity. This result was obtained by designing, thorough the Directivity model (2.20) a complex shape function. Because it was used for the passive monitoring, a complex shape function could be easily implemented by multiplying the imaginary part acquired signal for the imaginary unit $+j$. Then, only the one side spectrum was used: by considering the analytical or anti-analytical complex signal, the desired mainlobe orientation (i.e. a 180° rotation) was selected. In the context of active monitoring, with the aim to excite directional waves, it is mandatory to explain how the "complex shape function" can be interpreted. In the following, the last aim will be addressed in three steps:

- An intuitive mathematical-physical explanation of the directional waves excitation will be provided, in order to find the main points useful for the purpose.
- It will be shown how the main points can be achieved by using the Directivity model (2.20).
- An alternative design procedure to directly satisfy the key points will be detailed.

6.2.1 Step 1: Main points derivation via a simple model for directional GWs

As first stage, let consider a shape function constituted by two parts, referred to, without lack of generality, as *real* (Re) and *imaginary* (Im). Let us suppose they are super-directive in direction $\mathbf{k} = \pm\mathbf{k}_c$ (both ones represented as two dots in the

$\mathbf{k}$-plane, with different phases). Therefore, they are:

$$\begin{aligned} D\left\{\mathrm{Re}\left(\phi_P(\mathbf{x})\right)\right\} &\doteq D_{\mathrm{Re}} = \left|A_{D-\mathrm{Re}}\right| \left(e^{j\varphi_1(\mathbf{k}_c(\omega_c)}\delta\left(\mathbf{k}+\mathbf{k}_c\right) + e^{-j\varphi_1(\mathbf{k}_c(\omega_c)}\delta\left(\mathbf{k}-\mathbf{k}_c\right)\right) \\ D\left\{\mathrm{Im}\left(\phi_P(\mathbf{x})\right)\right\} &\doteq D_{\mathrm{Im}} = \left|A_{D-\mathrm{Im}}\right| \left(e^{j\varphi_2(\mathbf{k}_c(\omega_c)}\delta\left(\mathbf{k}+\mathbf{k}_c\right) + e^{-j\varphi_2(\mathbf{k}_c(\omega_c)}\delta\left(\mathbf{k}-\mathbf{k}_c\right)\right) \end{aligned} \tag{6.1}$$

For the convenience of notation, in the following $\varphi_1(\mathbf{k}_c(\omega_c)$ and $\varphi_2(\mathbf{k}_c(\omega_c)$ will be denoted as φ_1 and φ_2, assuming implicit they are the phases at $\mathbf{k}_c$ values. Let us suppose to excite a cosine wave on the real part with frequency ω_c, corresponding to the $\mathbf{k}_c$ value via the dispersion curve of a certain structure to be monitored. Then, let us suppose to excite on the imaginary part a signal given by the multiplication by $-j$ of the positive one-sided signal spectrum (observe that the last multiplication, except for the negative sign, was used also for the mono-directional DCS), and by the multiplication by $+j$ the negative spectrum of the signal actuated on the real part. Therefore the excitation signal in the frequency domain are given by:

$$\begin{aligned} U_{\mathrm{Re}}(\omega) &= A(\delta\left(\omega+\omega_c\right)e^{-j\varphi} + \delta\left(\omega-\omega_c\right)e^{+j\varphi}) \\ U_{\mathrm{Im}}(\omega) &= A(-j\delta\left(\omega+\omega_c\right)e^{-j\varphi} + j\delta\left(\omega-\omega_c\right)e^{+j\varphi}) \end{aligned} \tag{6.2}$$

It is worth noting that $u_{\mathrm{Im}}(t) = F^{-1}\left\{U_{\mathrm{Im}}(\omega)\right\}$ is still a real signal. The last property can be easily proved by considering the Hilbert Transform (HT), defined as:

$$H\left\{u(t)\right\} = \frac{1}{\pi t} * u(t) \tag{6.3}$$

where $*$ denotes the convolution product. Therefore, The HT provides a real signal. Thanks to the relationship between the Hilbert Transform and the Fourier Transform, given by:

$$\begin{aligned} &F\left\{H\left\{u(t)\right\}\right\}(\omega) = -i\mathrm{sign}(\omega)F\left\{u(t)\right\}(\omega) = \\ &= F(\omega)\cdot\begin{cases} j & for\ \omega<0 \\ 0 & for\ \omega=0 \\ -j & for\ \omega>0 \end{cases} \end{aligned} \tag{6.4}$$

the second equation of (6.2) is achieved by applying the -HT operator to the signal $u_{\mathrm{Re}}(t)$. The result is still a real signal. By using the model (2.18) for the piezo-sensor frequency response and, without lack of generality, discarding the constants and the known scale function factors (i.e $\pm j, k_0(\omega)$ and $H_P(\theta)$), the frequency responses (2.18) for $\omega > 0$ and $\omega < 0$ are given by:

$$\begin{aligned} V_{P(\omega>0)}(\omega) &= U_{\mathrm{Re}(\omega>0)}(\omega)D_{\mathrm{Re}}(\mathbf{k}(\omega)) + U_{\mathrm{Im}(\omega>0)}(\omega)D_{\mathrm{Im}}(\mathbf{k}(\omega)) \\ V_{P(\omega<0)}(\omega) &= U_{\mathrm{Re}(\omega<0)}(\omega)D_{\mathrm{Re}}(\mathbf{k}(\omega)) + U_{\mathrm{Im}(\omega<0)}(\omega)D_{\mathrm{Im}}(\mathbf{k}(\omega)) \end{aligned} \tag{6.5}$$

Therefore:

$$\begin{aligned} V_P(\mathbf{k},\omega) = & \left[\begin{array}{l} |AA_{D-\mathrm{Re}}|e^{+j\varphi}\left(e^{-j\varphi_1}\delta\left(\mathbf{k}+\mathbf{k}_c\right) + e^{+j\varphi_1}\delta\left(\mathbf{k}-\mathbf{k}_c\right)\right) + \\ +j|AA_{D-\mathrm{Im}}|e^{+j\varphi}\left(e^{-j\varphi_2}\delta\left(\mathbf{k}+\mathbf{k}_c\right) + e^{+j\varphi_2}\delta\left(\mathbf{k}-\mathbf{k}_c\right)\right) \end{array} \right] \delta\left(\omega-\omega_c\right) + \\ & + \left[\begin{array}{l} |AA_{D-\mathrm{Re}}|e^{-j\varphi}\left(e^{-j\varphi_1}\delta\left(\mathbf{k}+\mathbf{k}_c\right) + e^{+j\varphi_1}\delta\left(\mathbf{k}-\mathbf{k}_c\right)\right) + \\ -j|AA_{D-\mathrm{Im}}|e^{-j\varphi}\left(e^{-j\varphi_2}\delta\left(\mathbf{k}+\mathbf{k}_c\right) + e^{+j\varphi_2}\delta\left(\mathbf{k}-\mathbf{k}_c\right)\right) \end{array} \right] \delta\left(\omega+\omega_c\right) \end{aligned} \tag{6.6}$$

Finally, observe that if and only if the two parts of the shape function, $\phi_P(\mathbf{x})$, are designed so that:

$$\begin{cases} |A_{D-\mathrm{Re}}| = |A_{D-\mathrm{Im}}| \\ \varphi_2(\mathbf{k}_c(\omega_c)) = \varphi_1(\mathbf{k}_c(\omega_c)) - \pi/2 \end{cases} \tag{6.7}$$

here, referred to as *constitutive equations* for shape function able to excite directional waves, the $\mathbf{k} - \omega$ response is Hermitian. The corresponding excited Lamb wave is given by:

$$\begin{aligned} V_{p(\omega<0)}(\mathbf{k},\omega) &= |AA_{D-\mathrm{Re}}|e^{j(\varphi_1+\varphi)}\delta\left(\mathbf{k}+\mathbf{k}_c\right)\delta\left(\omega+\omega_c\right) \\ V_{p(\omega>0)}(\mathbf{k},\omega) &= |AA_{D-\mathrm{Re}}|e^{-j(\varphi_1+\varphi)}\delta\left(\mathbf{k}-\mathbf{k}_c\right)\delta\left(\omega-\omega_c\right) \end{aligned} \tag{6.8}$$

It is worth noting that the (real) solution for the Lamb waves equation (2.1), is postulated as a superposition of sinusoidal waves, having the out-of-plane displacement along the thickness z-coordinate components equal to:

$$\begin{aligned} Lw_{\sin}\left(z,\mathbf{k}(\omega)\right) &= A_z f(z)\left[\delta(\omega-\omega_c)\delta(\mathbf{k}+\mathbf{k}_c) + \delta(\omega+\omega_c)\delta(\mathbf{k}-\mathbf{k}_c)\right] \\ Lw_{\sin}\left(z,\mathbf{k}(\omega)\right) &= A_z f(z)\left[\delta(\omega+\omega_c)\delta(\mathbf{k}+\mathbf{k}_c) + \delta(\omega-\omega_c)\delta(\mathbf{k}-\mathbf{k}_c)\right] \end{aligned} \tag{6.9}$$

which are, respectively, a progressive and regressive wave. Therefore, the Eqs. (6.8) in $\omega - \mathbf{k}$-domain correspond to only one Lamb wave, excited in direction $\mathbf{k}_c$. It is a regressive wave (namely, the multiplied δ "functions" have the same signs in ω and $\mathbf{k}$). Conversely, progressive waves refer to incoming Lamb waves in direction $\mathbf{k}_c$.

The *physical explanation* is that: the two parts of the sensor are characterized by a phase shift equal to $pi/2$ in **k**-space , an additional $pi/2$ shift is generated by the different propagating waves, such that Lamb waves excited by the two parts interfere constructively and destructively, respectively, for $\omega > 0$, in direction $\mathbf{k}_c$ and $-\mathbf{k}_c$. Vice-versa for $\omega < 0$.

The alternative application of HT or -HT to the actuated or sensed pulse (on the imaginary part) allows to scan separately an angle θ and $\theta + 180°$.

A final important note is that if the operator -HT is used to scan the surface along $\mathbf{k}_c$, due to the fact that potential echoes propagate in the opposite direction, $-\mathbf{k}_c$, HT has to be used in the acquisition phase.

As conclusion, in order to excite or detect directional waves with a *real shape function*, three main points has to be achieved:

1. The shape function has to be constituted by two parts (i.e. 2 different acquisition channels are required)
2. The Directivity functions of the two parts have to be in quadrature (see the *constitutive equations* (6.7)).
3. The signal computed from the HT or -HT operator applied on the "real" part signal, has to be used as excitation signal on the "imaginary" part.

6.2.2 Step 2: A formal design procedure

The second step aim is to define a transducer design procedure which satisfies the 3 key points of Step 2, linked to the model (2.20), for the active monitoring. Let's start to design, as for the DCS, a transducer by inverting the Eq. (2.20) and imposing a Directivity function non-zero along certain directions (e.g. between 0° and 179.9°) and zero in the opposite ones (180°-359.9°). Subsequently, let us impose the Hermitian property on the Directivity function. The first procedure, as seen for DCS, results in a complex shape function $\phi_P(\mathbf{x})$. In the following, the wave-vector will be expressed as $\mathbf{k} = \kappa \mathbf{i}_k$, where κ is the wave-vector scalar part, which assumes both positive and negative values, while $\mathbf{i}_k$ is the unit vector so that all directions are covered (e.g. $\mathbf{i}_k$ points towards all angles between 0° and 179.9°).

The Directivity function can be decomposed as:

$$\begin{aligned} & D\left\{\phi_P(\mathbf{x})\right\}(\kappa) = D\left\{\operatorname{Re}\left(\phi_P(\mathbf{x})\right)\right\}(\kappa) + jD\left\{\operatorname{Im}\left(\phi_P(\mathbf{x})\right)\right\}(\kappa) = \\ & = \left(\left|D_{\mathrm{Re}}\right| e^{-j\varphi_{D_{\mathrm{Re}}}}\right)_{(\kappa<0)} + \left(\left|D_{\mathrm{Re}}\right| e^{+j\varphi_{D_{\mathrm{Re}}}}\right)_{(\kappa>0)} + \\ & +j\left[\left(\left|D_{\mathrm{Im}}\right| e^{-j\varphi_{D_{\mathrm{Im}}}}\right)_{(\kappa<0)} + \left(\left|D_{\mathrm{Im}}\right| e^{+j\varphi_{D_{\mathrm{Im}}}}\right)_{(\kappa>0)}\right] \end{aligned} \tag{6.10}$$

The design procedure is so that:

$$\begin{aligned} & D_{(\kappa<0)}\left\{\phi_P(\mathbf{x})\right\}(\kappa) = 0 \\ & D_{(\kappa>0)}\left\{\phi_P(\mathbf{x})\right\}(\kappa) = D_{Fixed}(\kappa) \end{aligned} \tag{6.11}$$

From the fact that $\operatorname{Re}\left(\phi_P(\mathbf{x})\right)$ and $\operatorname{Im}\left(\phi_P(\mathbf{x})\right)$ are not influenced by the sign of κ, and from the first equation of Eqs. (6.11), ti can be concluded that:

$$\begin{cases} \left|D_{\mathrm{Re}}\right| = \left|D_{\mathrm{Im}}\right| \\ \varphi_{D_{\mathrm{Im}}} = \varphi_{D_{\mathrm{Re}}} - \pi/2 \end{cases} \tag{6.12}$$

Furthermore, $D_{Fixed}(\kappa) = 2\left|D_{\mathrm{Re}}\right| e^{+j\varphi_{D_{\mathrm{Re}}}}$. Observe that the Eqs. (6.12) are the *constitutive equations* corresponding to ones derived in Step 1 (Eqs. (6.7)). Then, the Hermitian property of the Transducer Sensing in $\omega - \mathbf{k}$-domain has to be imposed to excite real signals. Therefore, $D_{P(\omega<0)}\left\{\phi_{P(\omega<0)}(\mathbf{x})\right\}(\kappa>0) = D^*_{P(\omega>0)}\left\{\phi_{P(\omega>0)}(\mathbf{x})\right\}(\kappa<0)$ is imposed. Furthermore, the last procedure has to preserve the properties in (6.12). Let us compute the complex conjugate of the Directivity:

$$\begin{aligned} & D^*_{P(\omega>0)}\left\{\phi_{P(\omega>0)}(\mathbf{x})\right\}(\kappa<0) = \left(\int e^{-j|\kappa|\mathbf{i}_k\cdot\mathbf{x}}\phi_{P(\omega>0)}(\mathbf{x})d\mathbf{x}\right)^* = \\ & = \int e^{+j|\kappa|\mathbf{i}_k\cdot\mathbf{x}}\phi^*_{P(\omega>0)}(\mathbf{x})d\mathbf{x} = D_{P(\omega<0)}\left\{\phi^*_{P(\omega>0)}(\mathbf{x})\right\}(\kappa>0) \end{aligned} \tag{6.13}$$

Note that just $-j\left|\kappa\right|$ in the first *exp* term is considered, due to the relation between $\kappa - \omega$: when a directional incoming progressive wave has to be detected, the positive frequencies are associated to the negative values of κ and vice-versa, as seen in the Eqs. (6.9). The last equivalence provides the necessary and sufficient condition to satisfy the Hermitian property:

$$\phi_{P(\omega<0)}(\mathbf{x}) = \phi^*_{P(\omega>0)}(\mathbf{x}) \tag{6.14}$$

Observe that, considering separately the cases for $\omega > 0$ and $\omega < 0$, a shape function which satisfies the last equation, preserves the *constitutive equations* (6.12), and it is equivalent to exciting a signal on the real part and its HT on the imaginary one. Finally, observe that the design procedure provides to use the HT, instead of -HT, because in Eq. (6.14) it was assumed to detect incoming Lamb waves which are progressive (namely with κ and ω with opposite signs). This choice is in accordance to the Directivity model (2.20) (for mono-channel shape function), which considers progressive the incoming Lamb waves. Therefore, as previously seen, to excite waves in the directions $|\kappa|\,\mathbf{i}_k$ -HT has to be used.

As conclusion, ***the procedure defined in this section will be used to design novel Transducers for active monitoring***. The *real* and *imaginary* terms for the piezo-parts have still meaning when they are considered just as the 2D-IFT of the Directivity in the first phase of the design procedure. Actually, after imposing the Hermitian property, the imaginary part is led back to a real one considering the HT (or -HT) of the real part signal as an excitation signal.

6.2.3 Step 3: A secondary design procedure and discussion

The last step wants to answer to the question: is it possible to design transducers without imposing *a posteriori* the Hermitian property on the Directivity function? In order to answer to this question and simplify the discussion, it is convenient to study the Directivity model by considering the 1D-FT of Radon Transform (RT) at angle θ (as previously seen in Chapter (3)). Therefore, the Directivity can be written as:

$$\begin{aligned} D_P(\mathbf{k}_0(\omega)) &= \int\limits_{\Omega_P} e^{-j\mathbf{k}_0(\omega)\cdot\mathbf{x}}\phi_P(\mathbf{x})d\mathbf{x} = \\ &= \int\limits_{\rho} e^{-j\kappa\rho}\mathrm{RT}_\theta\left\{\phi_P(\mathbf{x})\right\}(\rho)d\rho \end{aligned} \tag{6.15}$$

As any 1D-FT, the Directivity can be decomposed in the following way:

$$D_P(\kappa) = \begin{cases} \int\limits_{\rho} e^{-j|\kappa|\rho} \mathrm{RT}_\theta(\rho) d\rho \quad for \;\; k \geq 0 \\ \int\limits_{\rho} e^{+j|\kappa|\rho} \mathrm{RT}_\theta(\rho) d\rho \quad for \; k < 0 \end{cases} \tag{6.16}$$

The first part can be seen as the anti-analytic part of the FT, while the second part as the analytic part of the IFT. Let us consider a Hermitian Directivity function so that $D_P^*(\kappa) = D_P(-\kappa)$ and to compute its related shape function as the IFT of the anti-analytic Directivity part, when $\kappa \geq 0$, and the FT of the analytic Directivity part, when $\kappa < 0$, according to the previous Eq. (6.16). Observe that the FT and the IFT differ just for a sign change in the *exp* term. Therefore, $F\left\{\mathrm{RT}_\theta(\rho)\right\}(\kappa) = F^{-1}(-\kappa) = F^{-1}\left\{\mathrm{RT}_\theta(-\rho)\right\}$. Furthermore, the Real and Imaginary parts of the FT (or IFT) of a given function, can be related to even and odd parts of the same function:

$$\begin{aligned} &D_{\mathrm{Re}}(\kappa) = \tfrac{1}{2}\left[D(\kappa) + D^*(\kappa)\right] \\ &\Leftrightarrow \tfrac{1}{2}\left[\mathrm{RT}_\theta(\rho) + \mathrm{RT}_\theta{}^*(-\rho)\right] = RT_{\theta\ (Even)}(\rho) \\ &D_{\mathrm{Im}}(\kappa) = \tfrac{1}{2j}\left[D(\kappa) - D^*(\kappa)\right] \\ &\Leftrightarrow \tfrac{1}{2j}\left[\mathrm{RT}_\theta(\rho) - \mathrm{RT}_\theta{}^*(-\rho)\right] = -jRT_{\theta\ (Odd)}(\rho) \end{aligned} \tag{6.17}$$

Therefore, if the first equation of (6.16) provides $\mathrm{Re}\left\{\mathrm{RT}_\theta(\rho)\right\} + j\mathrm{Im}\left\{\mathrm{RT}_\theta(\rho)\right\}$, the second one will provide, thanks to FT and IFT relationship and the Even and Odd symmetry provided by the Real and Imaginary FT (or IFT) parts, $\mathrm{Re}\left\{\mathrm{RT}_\theta(\rho)\right\} - j\mathrm{Im}\left\{\mathrm{RT}_\theta(\rho)\right\}$. In this way, the Hermitian property is already satisfied (and corresponds to a multiplication for $\pm j$ multiplication of the imaginary part, respectively for $\kappa \geq 0$ and $\kappa < 0$. It is equivalent to use the HT on the signal acquired by the imaginary part, when an incoming progressive wave is detected.

It is interesting to observe that, overall, the discussed procedure doesn't set to zero the Directivity function for the negative and the positive wave-vector κ values, but suggests only how to select the shape functions for $\kappa \geq 0$ and $\kappa < 0$. In order to excite or detect directional waves, according to the sinusoidal Lamb waves postulated solutions, provided by the Eqs. (6.9), the shape function must change as the sign of ω changes. The obtained result is that just one time the design procedure can be executed: the second one-side spectrum in wave-vector domain can be restored by considering an apposite sign for the Imaginary part. This is exactly how works the design procedure in the Step 2.

As conclusion the last design procedure allows to achieve the 3 key points without imposing *a posteriori* the Hermitian property. As final note, it is very interesting to observe that the even and odd symmetry of the Real and Imaginary parts of the RT is mirrored on the symmetry of the Re and Im shape function parts, as already shown for the DCS shape function and as it will be seen for the novel transducer illustrated in the following sections. The symmetry properties could be used in future developments to design transducers with a reduced area occupation.

6.3 S-SAT: a Transducer for optimized damages localization performance

After well-formalizing the shape function design procedure for directional guided waves in *active monitoring*, in this Section and in the following ones, the design procedure is used to realize a novel transducer. The aim is to overcome the F-SAT limits in damages localization, seen in the Section (6.1.3), which are intrinsically related to the design criterion. Therefore, a different design approach was considered. The main idea is to discretize the considered angular range (180°), dividing it in multiple angular steps. For each discrete angular step, a different spectrum configuration is considered. Therefore, the transducer can be seen as an encoder: the acquired signal spectrum configuration is exploited for the DoA estimation. For this reason, the novel designed transducer is referred as Spectrum Scanning Acoustic Transducer (S-SAT). In the following Sections, the S-SAT design will be detailed according to the following scheme:

- The key points useful for the Directivity function design optmization.
- The Shape function synthesis: a more refined quantization procedure to get better results in terms of directive properties.
- A numerical validation in terms of matching of the frequency and time

responses provided by the Theoretical model and the Green's Functions simulations.

- The Signal Processing and estimation methods and performance for a considered excitation signal.

6.4 S-SAT: Directivity synthesis

As previously said, the novel Transducer is designed so that different spectral configurations are excited in different directions. To this aim, different *bit*-sequences are considered for different discrete angular steps. Therefore, on each step, the Directivity function is discretized in the wavenumber domain according to a predefined sequence of *Bins*. In each bin, the Directivity will be set to zero or non-zero values. Each *bin* in the k-domain corresponds to a bin in the ω-domain, via the relation $k_m = k_m(\omega)$ (i.e. the dispersion curve of a given Lamb wave m-mode). The Bin size and shape, the Directivity function in each bin and the Bins-configuration as a function of the angular step were selected, as follows:

6.4.1 Bin size and shape

First, the maximum sensor size has to be set. The sensor size influences the transducer impedance and, consequently, the specifications of the driving circuits. In the following, we will set the sensor size to be 10x10[cm].

The maximum transducer size defines the minimum Bin size in k-space. Let's start by considering a Bin with a rectangular shape. if a 2-D rect directivity function is considered over that domain, the sensor size can be defined, approximately, as the distance by the two first zeros of a 2-D sinc function, i.e. $2\,(1/a_{k_M})$, where a_{k_M} is the maximum length of the rectangular Bin sides, a_{k_1}, a_{k_2}. Conversely, by fixing the sensor size to 10x10[cm], the Bin side length is given by $2\,(1/10[cm]) \simeq 20[1/m]$. The last value defines the minimum side length of a Bin in k-space. As far as the Bin domain shape is concerned, considering that a sequence of Bins must cover an angular step, a candidate shape is given by a wedge with a cut-out. Such shape allows to fully cover a discrete angular step. When the two arches lengths difference of wedge-Bin is negligible, the Bin domain can be approximated as a rectangular domain. In this case, in order to have similar transducer dimensions along the radial coordinate and angular one, the length of two arches, l_θ, and the two radii, l_r, of a single wedge-Bin have to be comparable. Otherwise, the transducer would be elongated in one of two polar directions. For example, in Fig. (6.3)(a), it is illustrated a Bin in k-space, shaped as a wedge with a cut-out and with a Gaussian function over it, along the radial coordinate. In Fig. (6.3)(b), it is shown the corresponding shape function. It can be observed that, due to a slight difference of the l_θ, l_r lengths, the shape function is slightly elongated along a direction w.r.t. its perpendicular one. Therefore, if just one single bin is much more elongated along a polar coordinate, the entire transducer will be stretched along a physical dimension. However, it is important to observe that even if two or more bins are contiguous along the angular coordinate, they compose a unique Bins cluster in the k-space. Instead, the Bins clustering along the radial coordinate is avoided by considering a function over each $i-th$ Bin domain which falls to zero near the extremes, $k_{0B_i-\min}$, $k_{0B_i-\max}$, of the Bin k_0-values range $[k_{0B_i-\min}, k_{0B_i-\max}]$. In order to satisfy the hypothesis of planar wave fronts, independently by the DoA of wave-fronts, in the following, it will supposed that for a Bins cluster with the smallest arches lengths, other several rotated Bins, with the same size, are present in the Directivity function. They have to be rotated in $k_0\theta$-domain so that the transducer has the same radial dimension along all directions. In this way, the wave fronts can be considered planar for a certain defect distance which does not depend by the waves DoA.

6.4.2 Bin function selecting: ToF bound and signal patterns recognition as criteria.

Once the Bin domain shape is defined, the Directivity function in each Bin has to be selected appropriately. A *rect* function along the polar coordinate θ is selected in order to obtain the Directivity “building Bin” which fully covers an angular step in the same way along the angular unit vector of a polar reference system. Instead, the function along the radial coordinate has to be selected to optimize the damages localization accuracy.

Let’s start by finding the optimal Bin filter so that the estimation uncertainty of the time of flight (ToF), i.e. the time interval between the actuation and the echo reception, is minimized. The aim is to maximize the range estimation accuracy when the measurements are affected by noise and maximize the ability to distinguish signal patterns related to multiple defects, which are located at similar distances from the trasnducers.

The general formula for the CRLB of the ToF, namely δT^2, can be derived fomr the Theory of radar and sonar systems [82, 83, 84, 49]. In case of white noise, the time-delay estimation bound δT is given by:

$$\delta T = \frac{1}{\beta (2E/N_0)^{1/2}} \tag{6.18}$$

where E is the energy signal, N_0 is the power for unit frequency, E/N_0 is the signal-to-noise ratio (SNR) in energy and β is defined as:

$$\beta^2 = \frac{\int_{-\infty}^{\infty} (2\pi f)^2 |S(f)|^2 df}{\int_{-\infty}^{\infty} |S(f)|^2 df} = \frac{1}{E} \int_{-\infty}^{\infty} (2\pi f)^2 |S(f)|^2 df \tag{6.19}$$

$|S(f)|^2$ is the two-sided energy spectrum. Observe that Eqs. (6.18), (6.19) can be derivated from the Eq. (4.4), derived by Hahn and Tretter, for the DToA between sensors, considering the case of 2 sensors, the noise modeling as AWG, and considering the signals in energy, instead of in power. β is called *Effective Bandwidth* and it is equal to the second moment of the frequency energy distribution of $m-th$ transmitted signal, normalized on the energy signal. From the definition, observe that the larger is β value, the larger is the spreading of the energy distribution in frequency. From Eq. (6.19), it can be observed that the maximum value of β is given by πB_s, where B_s is the maximum value of the bandwidth of the transducer and it is obtained for a signal $s(t)$ so that $S(f)$ is equal to $\delta(f + B_{S/2}) + \delta(f - B_{S/2})$. This optimal solution corresponds to two sine waves (actually, two windowed sine waves so that their duration τ is $\tau >> 1/B$). By estimating the phase shift of two sine waves separated by a large band B, the ToA can be estimated optimally. However, this solution can be suboptimal when there are multiple damage-targets. Four or Five sinusoidal cycles are sufficient in radar applications to achieve a good accuracy [85]. However in the SHM context, due to the plurality of echoes generated by structural reflectors, the radar solution is unfeasible. Therefore, in order to avoid these problems, it is needed to increase the β value, by increasing the energy spread on frequency over each Bin.

Let's consider the case of exciting sine waves with central frequencies corresponding the one associate to a given Bin. In [80], it was proved that, when a stationary excitation signal is used, the optimal filter is given by the Gaussian filter which provides the maximum β value equal to $2.66B_{HP}$, where B_{HP} is the half-power bandwidth. This result is justified as the Gaussian filter allows to have a smoother frequency spectrum and, in dual way, sharper rise and fall time fronts. If a Gaussian pulse allows to minimize the ToF uncertainty, when an excitation stationary signal is used, at the same time it is characterized by two desired properties:

- the Gaussian pulse has the minimum time-frequency uncertainties product.
- the Gaussian shape is preserved also in a dispersive medium.

The first property allows to estimate, with reduced uncertainty, if a Gaussian Pulse (GP) is set to 0 or 1, by computing the integral of its amplitude spectrum in the frequency domain. The last procedure will be properly exploited to estimate the DoA of acoustic emissions. Note that this procedure is not affected by wave dispersion: the amplitude spectral integral is not influenced by the longer time-duration of a wave packet because even if the spectral components assume different phases, moving at different velocities, their amplitudes remain the same.

The second property allows to limit the signal processing computational cost required to estimate both the defects radial and distance coordinates, as will be detailed in Section (6.7). Finally, observe that Gaussian function in wave-vector domain allows to minimize the Transducer size.

The Directivity function for a "building Bin" rotated by an angle ξ (in counter-clockwise sense) and translated by k_{0c} is described as follows:

$$\begin{gathered} D(k_0(\omega),\theta) = \\ \exp\left(-\frac{1}{2}\frac{\left(k_0-k_{0c}\right)^2}{\sigma_k^2}\right) rect\left(\frac{\theta-\xi}{\Delta\theta}\right) \end{gathered} \tag{6.20}$$

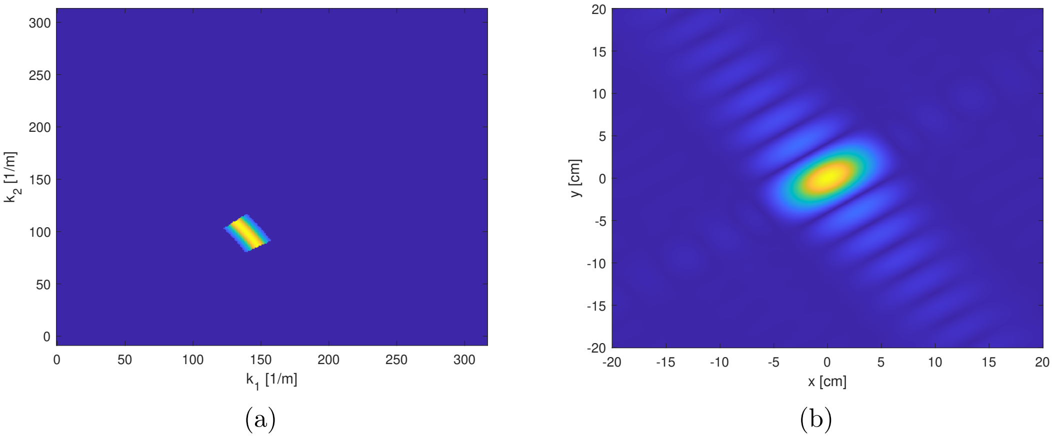

(a) (b)

Figure 6.3: (a) Example of a Gaussian function Bin over a wedge with a cut-out domain (radial length equal to 22[1/m]; angular range equal to [30°-40°]: $\sigma_k = 4.23[1/m]$; $k_{0min} = 160[1/m]$). (b) The Corresponding shape function in space domain.

The corrisponding shape function is the following:

$$\begin{aligned} &f(r,\alpha) = \\ &\sqrt{2\pi}\sigma_k \Delta\theta \exp\left(-\tfrac{1}{2}\tfrac{r^2}{\sigma_r^2}\right) \operatorname{sinc}\left(\Delta\theta(\alpha-\xi)\right) \\ &\simeq \sqrt{2\pi}\sigma_k l_k \exp\left(-\tfrac{1}{2}\tfrac{r^2}{\sigma_r^2}\right) \operatorname{sinc}\left(l_k r_{k_{0c}}(\alpha-\xi)\right) \end{aligned} \tag{6.21}$$

where l_k is the wedge arc length for $k_0 = k_{0c}$ and $\sigma_r^2 = 1/2\pi\sigma_k^2$. Fig. ((6.3))(a) and (b) show a Bin directivity function example and the corresponding shape function in the space domain, respectively

Observe that it is convenient to excite a train of Gaussian pulses with carrier frequencies matching those of each Bin.

In Eq. (6.19), $S(f)$ is the spectrum of a Gaussian functions train. If the acquired signal is composed by n_B Gaussian pulses, so that n_B Bins are set to 1, theoretically, it is possible to perform n_B cross-correlation procedures. When the signal envelopes are used, the δT uncertainty, for a same defect, is reduced to:

$$\begin{aligned} &\delta T = \tfrac{1}{\beta(2E/N_0)^{1/2}} \\ &\text{with } \beta = n_B 2.66 B_{HP} \end{aligned} \tag{6.22}$$

The ToF uncertainty δT is directly related to the defect-target range or distance R uncertainty, via the relation $\delta R = v_g(\delta T/2)$.

Although the previous discussion is well-validated for RADAR and SONAR systems [80], the peculiarities of dispersive propagation must be taken into account. Therefore, the uncertainty δR is different for each bin due to different wave propagation velocities, $v_g(f_{c_i})$. Moreover, conventional Cross-Correlation procedures, may partially lose effectiveness, due to dispersion which affects the pulses time-width.

In order to address these issues, efficient dispersion compensation procedures [32] allow to warp the frequencies axis so that a constant wave velocity is recovered and the signal-packets are *"re-compressed"*, holding constant the ability to resolve two different defects. Alternatively, in order to reduce the computational cost, the detrimental dispersion effect can be limited with the design strategies detailed in the following Section.

6.4.3 Bins configurations in wave vector space

The number of Bins for each configurations to be set to 1 or 0, in k-space, has to be selected with the aim to:

- satisfy the project specifications related to the minimum detectable defect size and the maximum frequency excitable via embedded units;
- limit the computational cost for defects localization;
- maximize the number of Bins-configurations, increasing the DoA resolution;
- limit the detrimental dispersion effect;
- address issues of transducer feasibility.

Let's start by considering the useful wave vector range for transducer design. The minimum value of wave-vector is fixed by the minimum detectable defect/damage size. Indeed, the inverse minimum k_0 value defines the maximum excited wavelength, which in turn defines the defects resolution. By fixing the maximum wave-length to 1[cm], namely considering detectable defects 1[cm] in size, the corresponding k value is equal to 100[1/m]. Instead, the maximum value of wave-vector is defined by the maximum frequency value which an micro-controller embedded unit is able to excite on the driven sensor load, fixed to 450[kHz]. An aluminium plate, 1[mm] thick was considered as setup structure to be monitored. However, the same directivity design criteria that are considered in the following, can be adopted when different structures/materials are considered. When A_0 is the excited wave mode, through the characteristic dispersion curve, the maximum k value 250[1/m] is found. The minimum frequency value, corresponding, via the same curve, to the minimum k_0 value, is equal to 90[kHz]. To summarize the previous results, the useful ranges, in k_0 and f, are given by $[100 - 250][1/m]$ (or $[624 - 1571][rad/m]$) and $[90 - 450][kHz]$, respectively.

Once defined the useful k_0 range, in order to limit the computational cost for the defects localization, the Bin with the highest central wave vector value, k_{0c}, namely at the highest corresponding central-frequency f_c, is set to 1 for all directions in [0-179°] range. It will be referred to as *range reference Bin.* The echo signal acquired in that range, properly filtered with a linear phase filter, can reveal the number of defects and their distances.

The *range reference Bin* involves to consider again a supplementary bin with the second highest central wave vector value, k_{0c}, which is to be set to 0. The motivation is related to the feasibility of the tranducer. In particular, the quantization procedure, which is defined in Section (6.5.1), shows limited capabilities to distinguish, in the dual domain, i.e. the k_0-space, single Bins near to a Bin cluster with high angular aperture. Therefore, the *range reference Bin*, overall, involves the negative aspect to reduce the k_0 available bandwidth but, in turn, it significantly reduces the computational cost in the defects detection and ranging. Further quantization procedure developments are aimed to avoid the secondary unnecessary Bin. It is important to note that, although the defects δR uncertainty is fixed by the *reference bin* (i.e. its effective bandwidth and its related group wave velocity), in order to estimate both the defect distance and the angle is necessary that all bins with the carrier frequencies f_{c_i}, do not overlap in time the bins, with the same f_{c_i}, related to another defect. In this way, the signals due to two different defects do not interfere and it is possible to assess what pulses, related to a defect and to the other one, are set to 1 or 0, providing the DoAs information.

The number of the Bins which can be set to 0 or 1, is to be found so that the number of binary sequence N_c is maximized, considering the constraints on the k_0-bandwidth. Similarly to the case of the F-SATransducer, a trade-off can be observed between the bandwidth of Bins in k_0, and, via the dispersion curve, in frequency f, and the angular accuracy. The lower is the number of Bins, the higher is their bandwidth and the ability to distinguish two Bins related to two different defects. Conversely, the higher is the number of Bins, the higher is the number of useful binary configurations and the DoA estimation accuracy. However, there is significant difference between the F-SAT and S-SAT design criteria. Indeed, in the F-SAT design, the Bins are displaced so that they describe a continuous function of θ in $k_0\theta$-space, for this reason the spectrum of a considered Bin is partially overlapped to the one of the nearest Bins. This involves a detrimental effect on the mainlobe aperture which is beyond the trade-off between the Bin bandwidth and the angular accuracy. Instead, thanks to the approach based on discrete Bins, the S-SAT transducer is characterized by a narrower mainlobe (and, consequently by a better angular resolution).

If we divide the available k_0 bandwidth into five equally spaced Bins, then $2^5 - 1$ binary configurations are available. In the following example, $N_c = 30$ binary configurations were considered to achieve a discrete angular step equal to 6[deg]. Considering the k_0 bandwidth equal to $150[1/m]$ and by dividing it into 7 Bins (5 for DoA estimation and the other two ones for detection and ranging), the bandwidth of each Bin is equal to $21.4[1/m]$. Slightly increasing the maximum excitable frequency, a Bin bandwidth equal to 22[1/m] can be achieved. The decision to select the same bandwidth in k_0 was taken to limit the dispersion effect. Due to the non-linear dispersion curve $k_0(f)$ shown in Fig. (6.4), when we increase the central wave-vector value k_{0c}, the corresponding central frequency is increased according to the following relation $f_c = f^{-1}(k_{0c})$. At the same time, when the frequency increases, the wave group velocity increases too. Due to the fact that the ability to solve two Bins related at two different defects is provided by $\delta R = v_g(f_c)(\delta T/2)$ and the uncertainty δT is inversely related to the (*effective*) bandwidth (according to the Eqs. (6.18)), equal Bins bandwidth in k_0 allows to increase the Bins bandwidth, when the wave velocity increases too. In other words, equal Bins k_0 bandwidths allow to equalize the δR uncertainty of the Bins/pulses at different f_c. Of course, the equalization is imposed only to the waves excited under the piezo-tranducer. Due to the dispersion, the higher are the distances of defects, the higher is the Bins δR uncertainty difference.

Theoretically, it is conceivable to select larger k_0 bandwidths for lower k_{0c} Bins. In this way, the ability to solve two signal patterns due to two different defects would be improved, by minimizing the distinguishable distance between two defects. However, this solution was not implemented, again to favor transducer feasibility: the quantization procedure shows poor performance when used to define in the dual domain (the Directivity domain) Bins clusters with different k_0 bandwidths. The reason can be identified in the filter used to get better results in terms of quantized shape function. This was defined considering a quantization processing to be applied on images described by discrete points in a Cartesian reference systems. Therefore, future developments are aimed to develop quantization procedure useful for Directivity functions shaped like *wedges with a cut-out.*

Finally, it is very important to select appropriately the binary configurations sequence. Our aim is to reduce the DoA uncertainty when a defect/damage is placed between two different discrete angular steps. The *Gray Code* ([86]) is especially important in applications where analog information is being converted to digital or vice-versa. For example, if two adjacent discrete angular steps are characterized by the configurations 00001 and 11111, wildly inaccurate measurements can occur at the boundaries between two angular sectors. The Gray code characteristic is that just one Bin configuration changes in k_0 and f, when moving by an angular step to the next or previous one.

Following the discussed strategy, the Directivity function was design as illustrated in Fig. (6.5) both in $\mathbf{k}$-space and in k_0, θ-space. In Fig. (6.5)(b) can be observed that the *Bins Gray tree* satisfies the assumption posed in Section (6.4.1). Apart from the first Bin on top, whose corresponding shape function is the furthest from the origin, the second Bins cluster with the smallest arches lengths are replicated in different directions to obtain a shape function with a radial size equal along all directions.

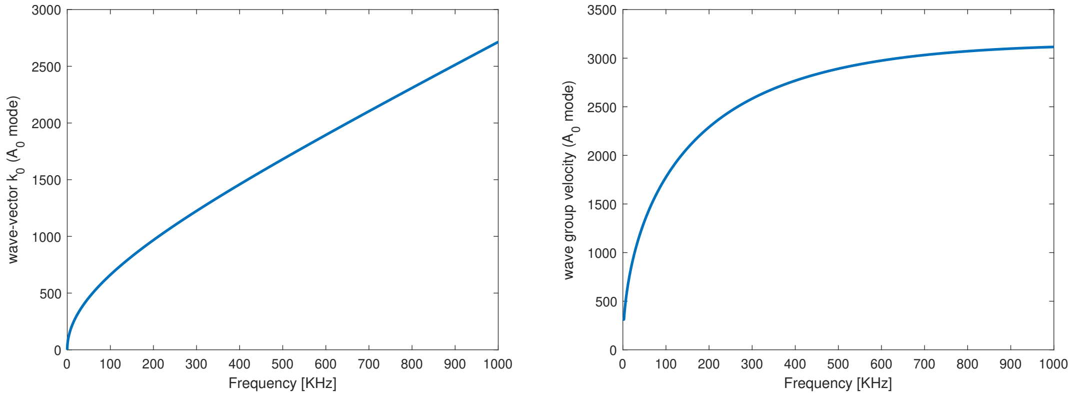

(a) (b)

Figure 6.4: The dispersion curve for an Aluminium Plate, 1[mm] thick: (a)wave-vector k_0 as function of frequency; (b)wave group velocity as function of frequency.

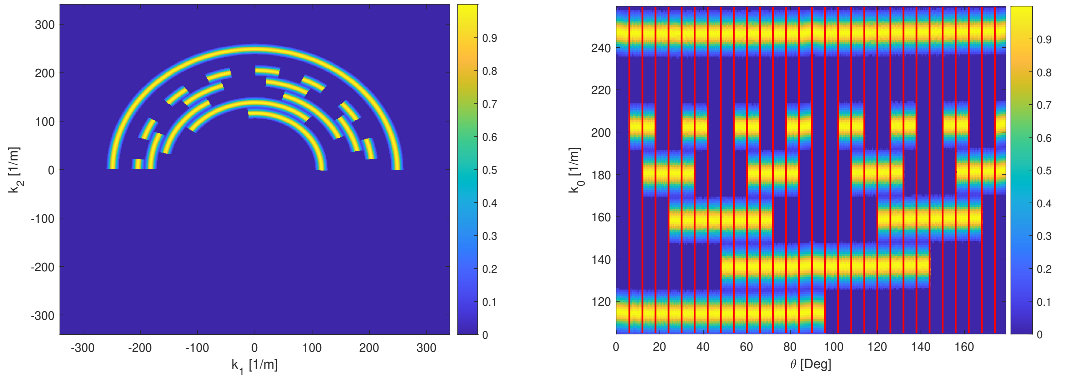

(a) (b)

Figure 6.5: (a) Imposed Directivity function according to the defined design criteria: (a) Directivity function in k_1, k_2-domain (b) Directivity function in k_0, θ-domain ($\sigma_k = 5.00[1/m]$)

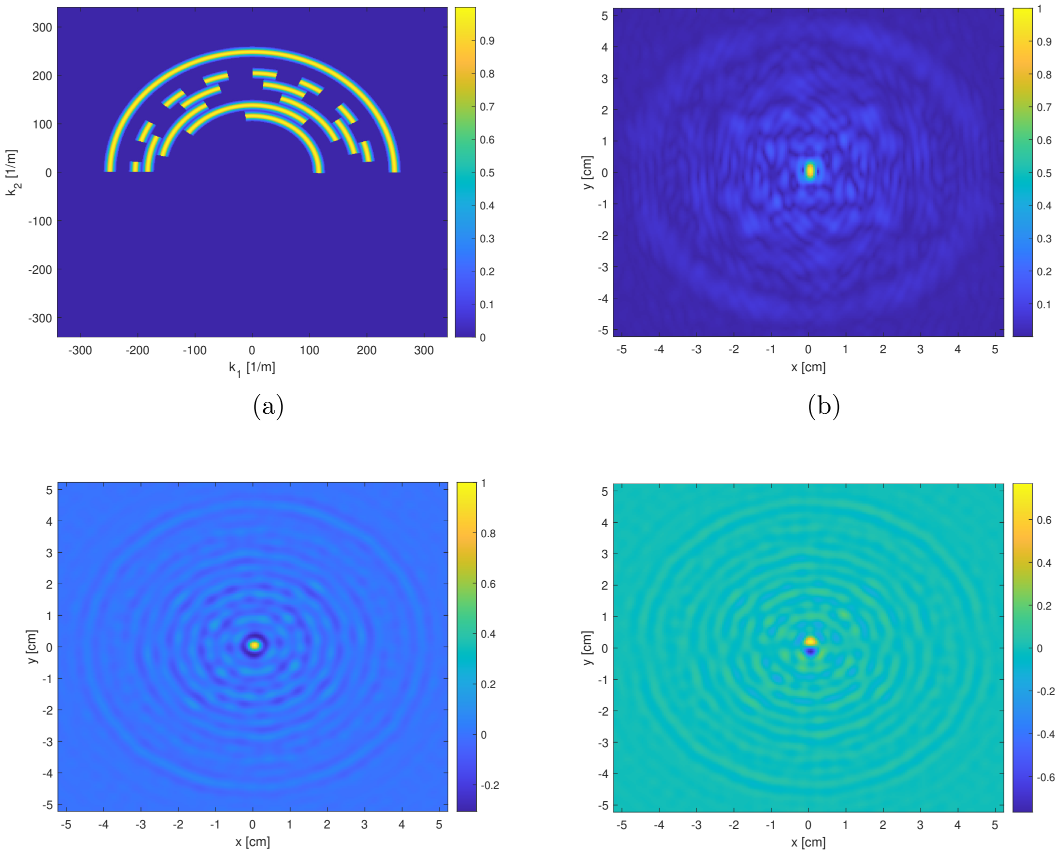

(a) (b)

(c) (d)

Figure 6.6: (a) Imposed Directivity function according to the defined design criteria; (b) Absolute value of the ideal shape function (ISF); (c) Real part of the ISF; (d) Imaginary part of the ISF;

6.5 S-SAT: Shape function transducer synthesis

The S-SAT Transducer shape function has to be computed so that its Fourier Transform is as close as possible to the designed Directivity function. According to the design procedure, defined in the Section (6.2.2), the ideal shape function can be computed by inverting the Eq. ((2.20)). In this way, a complex shape function, is obtained. Its absolute value and its real and imaginary parts are shown, respectively, in Figs. (6.6)(b,c,d).

As already observed in Section (6.2.3), the real part shows a even symmetry, while the imaginary part is charactized by an odd simmetry. The real part of the shape function has positive and negative values, so does the imaginary part. For this reason, the transducer requires two differential channels to excite and acquire the correct signal. Furthermore, observe that the obtained complex shape function is continuously modulated in values. Therefore, a quantization procedure has to applied. A numerical zero-padding procedure was used to increase the resolution in the space-domain, without reducing the **k**-space one, so that the quantization procedure provided better results when its Directivity function is computed. The discrete numerical dots have a 0.5[mm] physical size. In the next Subsection, the applied qauntization, the so called *double-phase Error Diffusion* technique, is illustrated.

6.5.1 Multi-phase Error Diffusion technique to emulate complex shape function

In Sec. (3.1.2) a quantization technique, called *Error Diffusion* ([40, 41]) was used in the passive SHM context to emulate shape functions which are continuously modulated.

However, it is worth noting that, for the purpose of the present work, each discrete value of the shape function, is a complex number. For such reason, the traditional error diffusion procedure (applied to real numbers) has to be rearranged. By following diagram shown in the patent [3] (see the Fig. (6.7)), the quantization procedure consists in the following steps:

1. The plane $(\mathrm{Re}, \mathrm{Im})$ is divided according to a phase quantization, so that

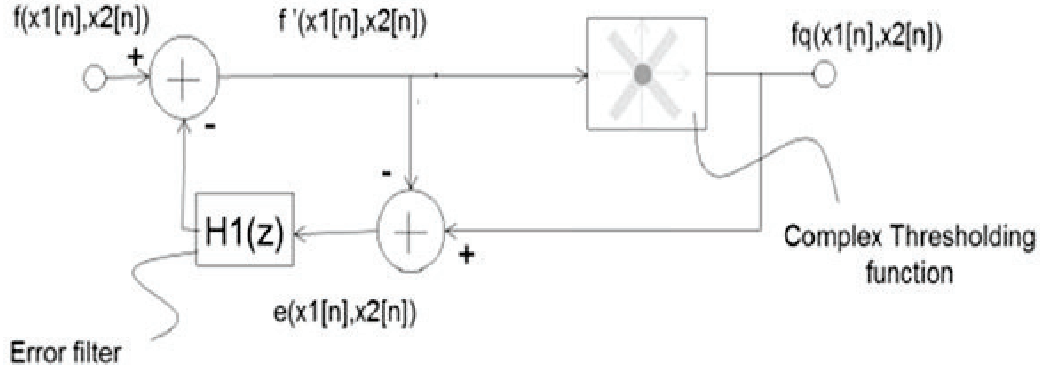

Figure 6.7: An illustrative scheme of the *Halftoning-Error Diffusion* quantization technique, useful for two channels images, namely for two-channels piezo-transducers

if |atan(Re/Im)| $<\pi/4$ or $> 3\pi/4$ the real plane values are selected, vice-versa, the imaginary ones. Therefore, the shape function in the nth point $f(x_1[n], x_2[n])$ is quantized as a function of the performed division of the plane $(\mathrm{Re}, \mathrm{Im})$.

2. The quantization error on point $e(x_1[n], x_2[n])$ is brought in feedback and summed to the new current value of $f(x_1[n], x_2[n])$ according to the weights associated to the error filters (H1).

3. Clustering: the numeric positive real values $fq(x_1[n], x_2[n])$, closely located, are clustered into a small region corresponding to the possible positioning of the electrical contact elements. The same procedure is executed for the negative real values and the imaginary positive and negative ones.

In this work, the following error filter (see [87]) is used:

$$\mathrm{H1} = \frac{1}{16}\begin{bmatrix} - & \# & 7 \\ 3 & 5 & 1 \end{bmatrix} \tag{6.23}$$

where "$-$" denotes a point in the current row which has already been processed (hence diffusing error to it would be pointless), and "#" denotes the pixel currently being processed.

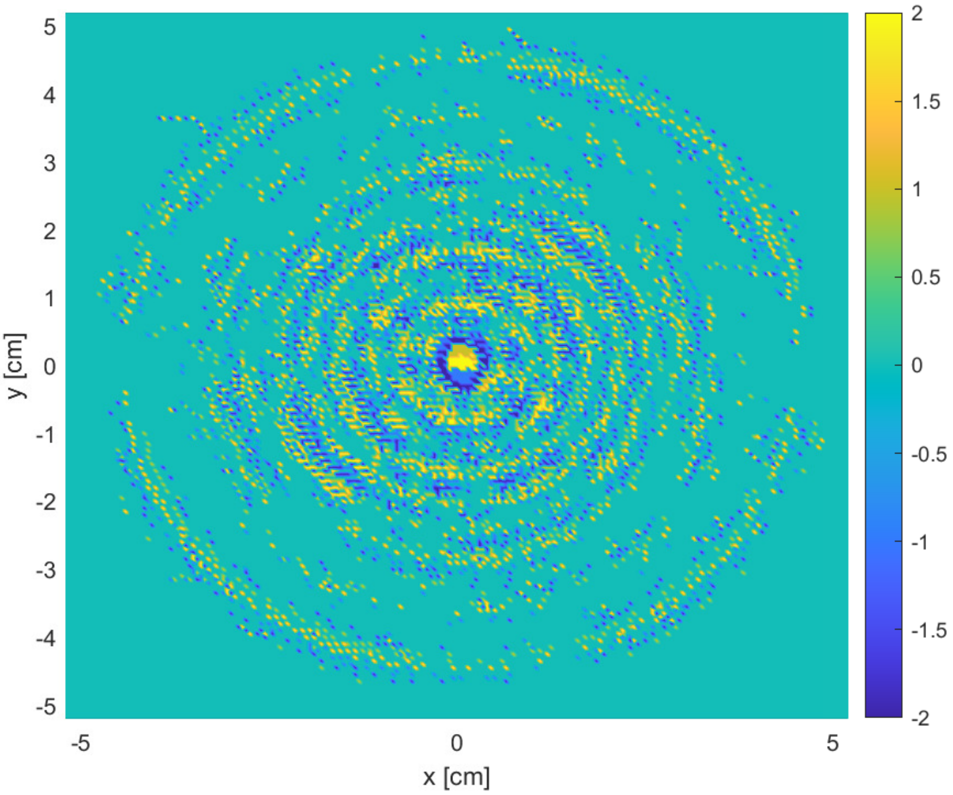

Figure 6.8: The Spectrum-Scanning Acoustic Transducer piezo-load, after the quantization procedure. The values +2 and −2 are related, respectively, to the positive and negative real part. The values +1 and −1 are related, respectively, to the positive and negative imaginary part.

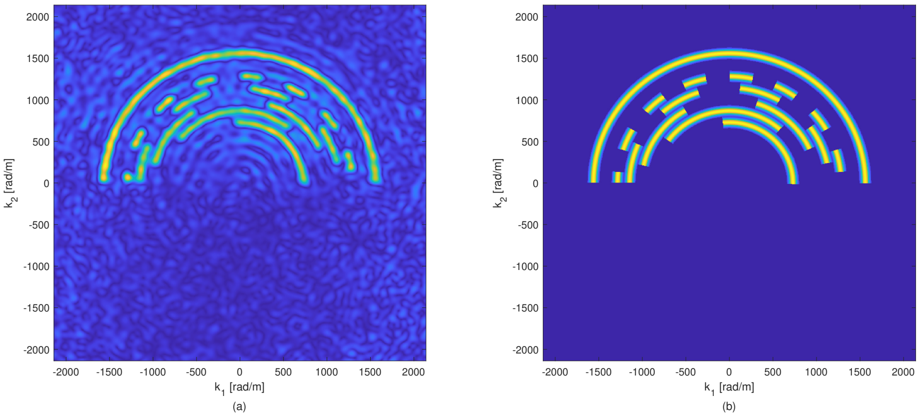

Figure 6.9: (a) Directivity function achieved after the quantization procedure; (b) Imposed Directivity function.

6.5.2 The feasible S-SAT and its directive properties

Once the *Halfotning Error diffusion* technique is applied to the ideal shape function, the transducer composed by 0.5[mm] dots and requiring just two differential channels is obtained. This is illustrated in Fig. (6.8).

By computing the Directivity function of the S-SAT piezo-load, it is possible to compare the ideal Directivity function and the achieved one. The Root Mean Square Error (RMSE), computed considering the range $[k_{0\,\mathrm{min}}, k_{0\,\mathrm{max}}]$, is equal to 0.15. A qualitative comparison of the ideal Directivity and the achieved one is provided in Fig. (6.9). Considering the dispersion curve $k_0(f)$ of the Lamb wave A0 mode which propagates in a Aluminium plate, 1[mm] thick, the angle-dependent spectral response of the implemented device is shown in Fig. (6.10).

It is interesting to show as the S-SAT (after the quantization procedure), satisfies the *constitutive equations* ((6.12)). This property is shown in the Fig. (6.11).

6.6 S-SAT: Numerical validation

6.6.1 Simulation Setup

Numerical simulations were run to evaluate the design transducer, considering the propagation of Lamb waves in an Aluminium plate, 1[mm] thick and with

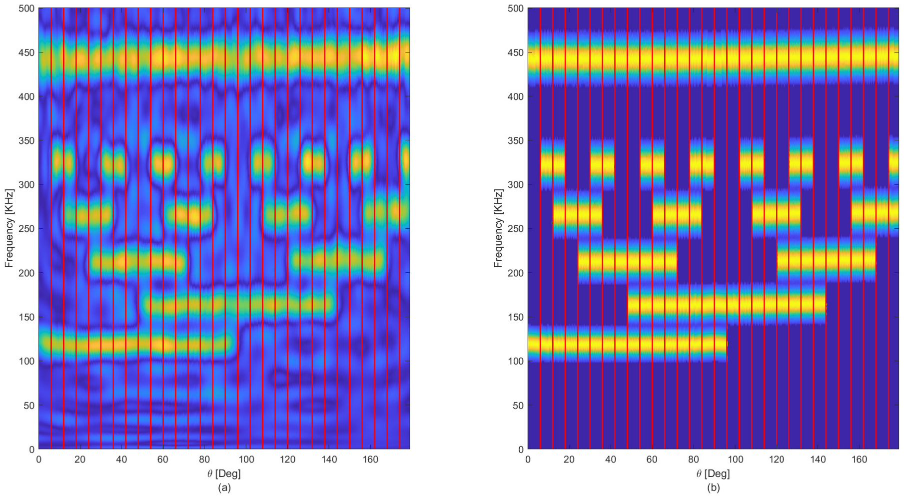

Figure 6.10: Directivity functions (in f, θ-domain) when the Lamb wave A0 mode propagates in an Aluminium plate, 1[mm] thick: (a) Directivity function after the quantization procedure (b) Imposed Directivity function.

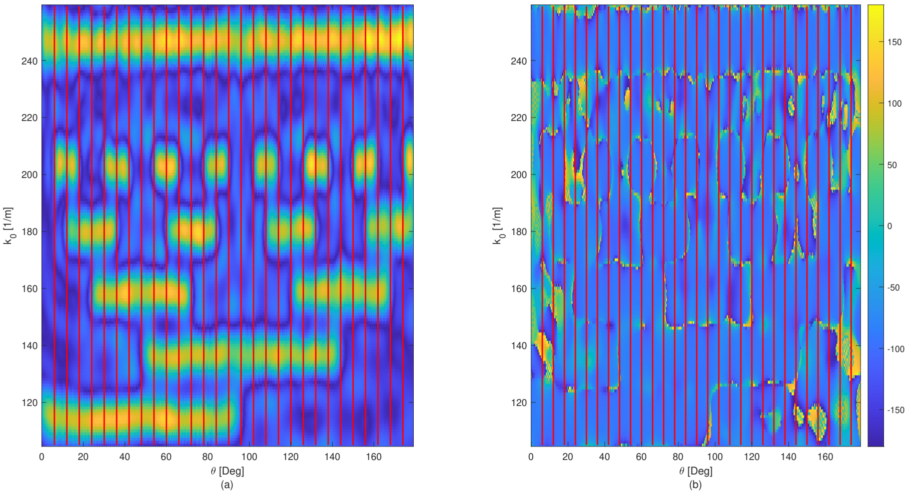

Figure 6.11: (a)Achieved Directivity function (in k_0, θ-domain); (b) a graphical explanation of the *constitutive equations* ((6.12)): the phase difference between the Directivity imaginary part and the real one is approximately equal to -90° over all non-zero Bins areas.

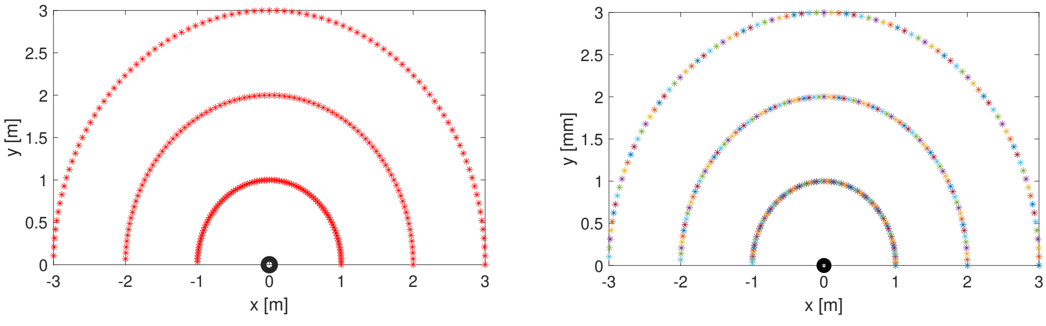

(a) (b)

Figure 6.12: (a) Excitation phase simulated as an acquisition phase: multiple phases acquisition considering impact points with different distances and angles were ran, considering the GPs train as the excitation signal. (b) The acquired signals due to waves impinging from different distances and angles were re-impacted considering the same corresponding distances and angles of the excitation signal.

the following parameters : Young's modulus 70 [GPa], Poisson's coefficient 0.3 and material density 2700 [kg/m3]. The same GFs formalism, detailed in Section (2.1.2), already adopted to validate the designed passive sensors network (shaped sensors, optimized disk-sensors array and directive sensors) was used in this context. Thanks to the reciprocity between the excitation of the waves acquisition and excitation phases, the last one can be simulated by using the transducer in passive way. Gaussian pulses train excitation signal were applied as input at a certain angle and distance from the transducer and, successively, the acquired signal was re-injected at the same angle and distance to emulate the effect of a perfect reflector. The last procedure was replicated for different distances and angles as illustrated schematically in the Fig. (6.12).

The excitation signal is shown in Fig. (6.13)(a). The Fig. (6.13)(b) shows the corresponding FT of the excited signal. The GPs central frequencies and bandwidths correspond nicely, via the dispersion curve $k_0(\omega)$, to the central wave-vector values and the bandwidths allocated to each Bin, during the design procedure (see Section (6.4.3)). More specifically, the central frequency values f_{c_i} and the bandwidths B_{HP_i} are given by the following values:

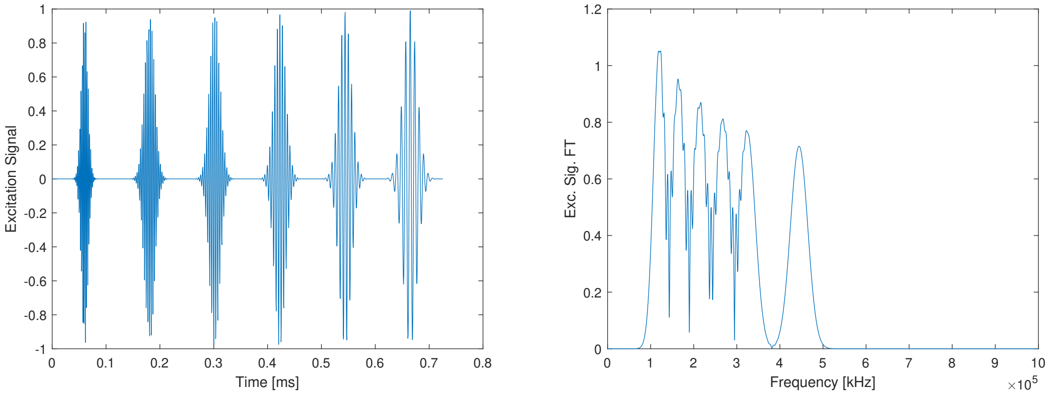

(a) (b)

Figure 6.13: (a) The Gaussian pulses train used as excitation signal; (b) The corresponding Fourier Transform (it is computed via the FFT, preserving the signal energy).

$$\begin{cases} f_{c_i} = (120; 164; 214; 267; 324; 444)[\text{kHz}] \\ B_{HP_i} = (22; 25; 27; 29; 31; 33)[\text{kHz}] \end{cases} \tag{6.24}$$

The numerical validation is very significant for two main reasons:

- The propagation along a mechanical medium in form of GWs was widely investigated and analytically well-formalised. Therefore, the propagation properties, such as the dispersion curves are well known and a numerical simulator can be reliably adopted.
- FEM simulations, tightly related to the experimental GWs propagation physics, were used in the Section (5.1.1) to assess the GFs simulations.

Therefore, experimental results are expected to be very close to the numerical ones.

Noteworthy, in practical cases some complexities have to taken into account. the GWs theory is derived considering a medium of infinite extension. However, even if an elongated structure is considered, mechanical boundaries generate reflections/reverberations or, in other words, multi-path interference. The edges reflections issue can be addressed, in the active monitoring, via the, so called, *baseline subtraction* ([88]). The last procedure allows to acquire the signals components

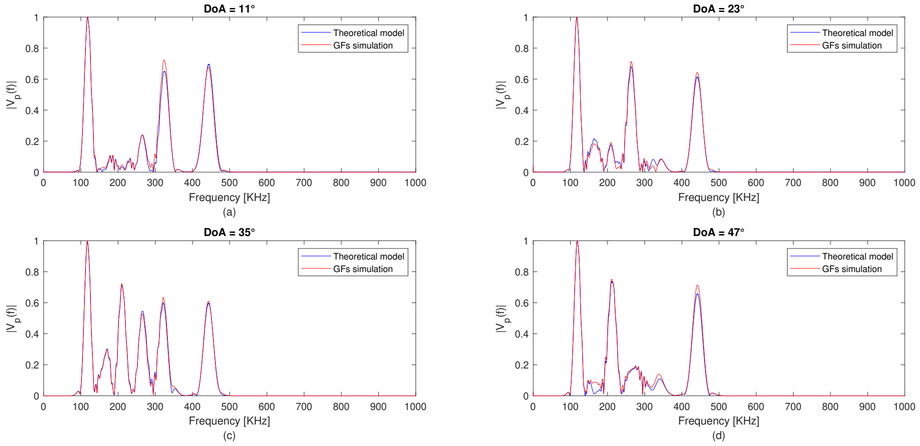

Figure 6.14: Frequency responses (divided by the constant terms and the known scale factor function ($\pm j$, $k_0(\omega)$) and normalized on the maximum value) for different DoAs (radius=0.8[m]) provided by the theoretical model (Eqs.(2.18)(2.20)) and the GFs formalism simulations.

due to boundaries reflections, on the pristine structure, free from damages. On in-service systems, edge reflections can be pre-computed by knowing the structure geometry.

Another issue is related to environmental and operational changes, such as temperature fluctuations, which can alter the wave propagation behaviour. The last effect can be addressed by using sensor able to estimate the dispersion curve variations via the known piezo-response model. By estimating the dispersion curve variations, the excitation signal can be tuned as well as the expected energy signals distributions for each directions can be re-computed. Therefore, in the following Sections the dispersion curves, derived in the Chapter (2), will be used, without prejudice to their potential variations.

6.6.2 Theoretical model and GFs simulations frequency-time responses matching

Although the validity of the theoretical model (2.18) was already proved (see Sec. (3.1.4)) via the GFs simulations by considering sensors quantized with pixeling procedure, as first step, due to the higher complexity of the S-SAT shape function,

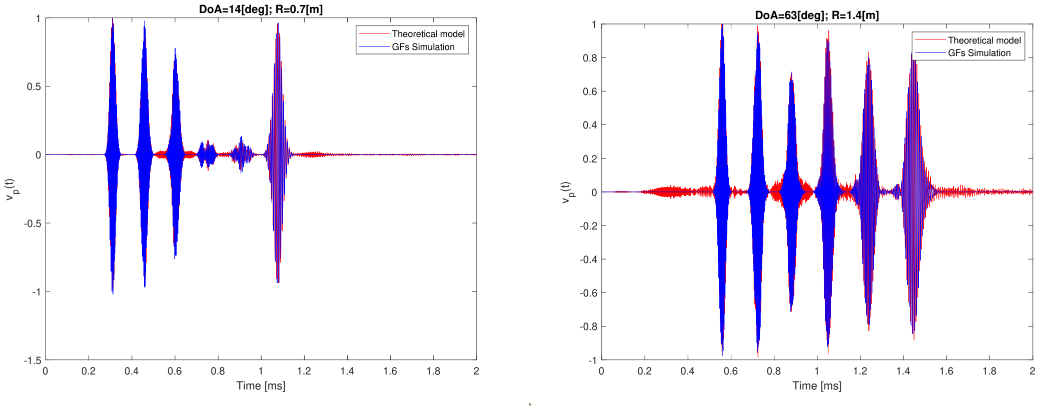

(a) (b)

Figure 6.15: Time responses (when the frequency responses are divide by the constant terms and the scale factor function ($k_0(\omega)$), and normalized on the maximum value) for two different DoAs and distances ((a) DoA=14°, R=0.35[m] (b) DoA=63°, R=0.7[m]), provided by the theoretical model (via the procedure of Section (3.1.4)) and the GFs formalism simulations.

namely a *multi-phase* function, was convenient to verify how well the responses, provided by the theoretical model and the GFs simulations one, match. As shown in Fig. (6.14), the considered models match quite-well in frequency. Note that, without lack of generality, the comparison, between the responses, is given only in terms of Directivity. Therefore, the frequency responses provided by the GFs simulations were divided by the constants ($\pm j$) and the scale factor function, $k_0(\omega)$, within the used frequency band. With the initial aim to compute the effect of the transducer filtering on the excited pulses (namely, how varied the time-spread of a Gaussian pulse) the theoretical time response was computed. Subsequently, the time responses were calculated by considering the dispersion effect of a propagating signal. To this aim, the procedure illustrated in Sec. (3.1.4) was applied. In Fig. (6.15) the S-SAT time-responses provided by the theory and the GFs simulations are given for two different distances and DoAs.

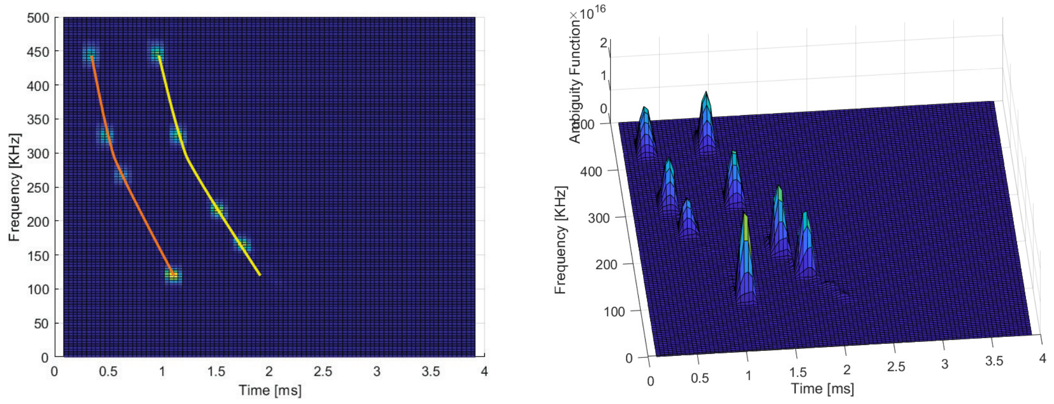

(a) (b)

Figure 6.16: The ambiguity functions, on the same FrT plane, of two signal patterns related at two different defects with radial and angular coordinates, respectively equal to 0.35[m] and 0.7[m], 14° and 63°: (a) top view (the signal patterns are traced by the red and yellow curves); (b) frontal view

6.7 S-SAT: Signal Processing and Estimation performance

In this Section, the Signal Processing procedures to localize multiple-defects and the estimation performance are will be detailed, when, the designed S-SAT Transducer is used in conjuction with GPs sequences as excitation signals.

In order to proceed, it is important to highlight the ability to distinguish two different signal patterns related to two different defects, when 180° are scanned simultaneously, and both their distances and angles are to be estimated. The previous ability is often called *ambiguity* in the Radar community.

In particular, it is often used the *ambiguity function* to define two different ambiguities. The desired ambiguity function is given by an impulsive function in the FrT plain. If this function is highly localized in the time domain, the distance resolution is enhanced. While a narrowband pulse is requested to better estimate the target (e.g. an aircraft) velocity, via the frequency shift, due to the Doppler effect. Therefore, the two ambiguities requires opposite signal properties.

In our context, the *targets* are static defects. However, the ambiguity function of an acquired signal can be again used to provide two information: the time-shift, i.e. the distance, and the sequence of pulses of the signal pattern, which provides the angular coordinate. This concept can be better clarified by seeing two signal patterns due to two different defects in the FrT domain. As an example, in Fig. (6.16) two ambiguity functions (their energy distributions) are shown in the same FrT plane. Such functions are related to two defects with different distances and angular coordinates. The signal patterns corresponding to the two defects are highlighted in Fig. (6.16)(a). It can be observed that:

- the two signals patterns are well-separated, even if their Difference in Time is less than the pulses trains time-duration.
- two signals patterns are given by two different sequences of Gaussian pulses. The binary pulses sequence provides the DoA information.

Observe that, the estimation of the DoA is hampered when multiple reflectors are located at the same distance. In case of multiple defects, their radial distance from the S SAT must be sufficiently large to generate separated patterns in the TF plane. The worst case pulse, namely the pulse most spread in time, is the one at the lowest central carrier frequency $f_c = 120$[kHz] and with lowest bandwidth $B_{HP} = 22.4$[kHz], even if this frequency corresponds to the lowest wave velocity $vg(f_c)$.

It is also worth noting the difference between the ability to distinguish two different signal patterns and the meaning of Eq. (6.22). The Eq. (6.22) shows a reduction of uncertainty δT, thanks to the multiple excited pulses. Theoretically, n_B cross-correlation procedures can be executed (after dispersion compensation) to have a more robust estimation of the ToF in presence of noise. Therefore, δT defines the ToA bound in presence of noise. Conversely, the ability to distinguish two signal patterns, i.e. the ambiguity δT_{A_S}, is equal to the uncertainty $2\delta T$ with $n_B = 1$, considering the worst case pulse (i.e. the pulse with the highest dispersion).

Several works proposed different tools to analyze Lamb waves signals in the FrT domain. In [89], the Wigner-Ville distribution was investigated for the mode analysis. In [90], it was shown that the *reassigned scalogram* distribution is able to better define the Lamb A_0 mode w.r.t. different FrT distributions. However,

SNR (dB)	Standard Deviation [m]	Maximum Error [m]
12	0.009	0.0151
10	0.0091	0.0162
8	0.0091	0.0186
6	0.0093	0.0193
4	0.0094	0.0233
3	0.0096	0.0217
2	0.0097	0.0255
1	0.0098	0.0236

Table 6.1: Defect Distance estimation performance for different values of the SNR (with: 51 random defects DoAs between 0° and 179°; 51 defects distances moving from 0.5[m] to 3[m], with a 5[cm] step, to take into account the slight dispersion effect; 100 AWGN simulated cases; removed distance attenuation).

it is important to observe that, when large distances are covered via GWs, the FrT distributions may require a computational cost incompatible with embedded systems applications. Alternatively, a bank of linear phase filters, such as FIR filters, can be used to distinguish the GPs with different carrier frequencies.

Therefore, it is necessary to find a useful signal processing procedure for a multi-defects localization with a limited computational cost. The considered signal processing can be divided in the following steps:

6.7.1 Step 1: compute the Directivity response

As first step, observe that the scale factor $k_0(\omega)$ may modify the shape of the GPs. Therefore, a single FFT is computed on the entire acquired signal (composed by multiple-signal patterns). The last one is divided by the scale factor function $k_0(\omega)$. Such procedure allows to restore the Gaussian shape of the pulses and to work just on the frequency response given by the applied signals (the real part one and its -HT application) and the Directivity function. The time-response can be computed via an IFFT.

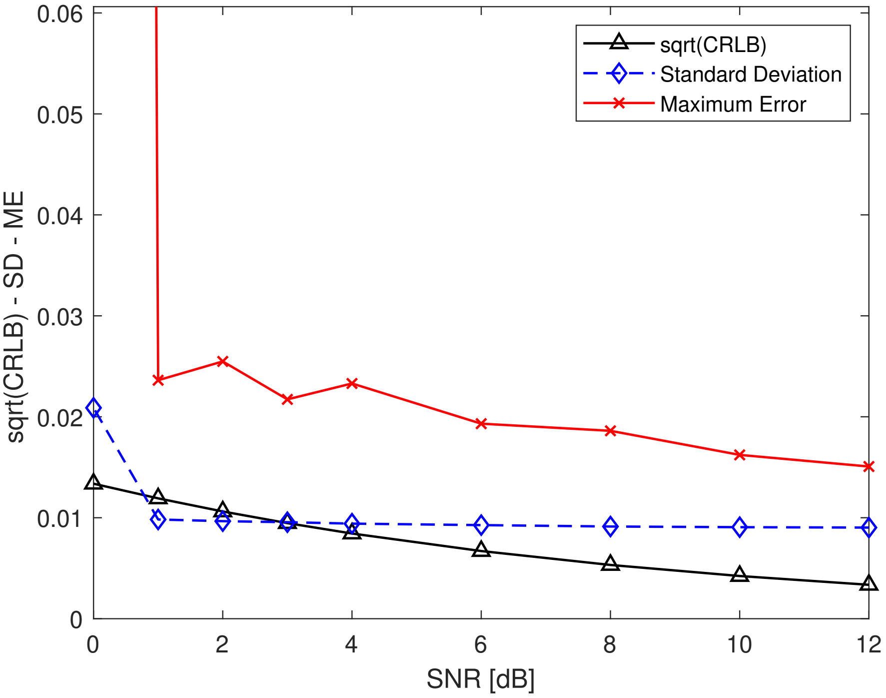

Figure 6.17: Defect distance estimation performance plots (related to the Tab (6.1)) in terms of Standard Deviation and Maximum Error (in meters), as function of the SNR. The estimation bound (the square root of the Cramér–Rao lower bound) is slightly attained.

6.7.2 Step 2: defects and distances estimation

As previously seen in Section (6.4.3), the S-SAT was designed by setting to 1 a Bin, called *reference bin*, between 0° and 179°. By using just its related signal, filtered by a linear phase 250 taps filter FIR (designed with a Gaussian window), the number of defects and their distances can be easily extracted. Thanks to the high Bin central frequency (f_c = 444[kHz]), the dispersion effect can be actually neglected. Indeed, for that frequency, the wave velocity is near to the constant Rayleigh velocity. Therefore, a single cross-correlation procedure can be computed. If the cross correlation is larger than a given threshold, fixed *a priori* considering the potential attenuation and the tolerated SNR value, a wave peak is detected. The ToA of each peak provides the defects distance information. The ToA uncertainty bound is given by the Eq. (6.22) with $n_B = 1$. To avoid multiple peaks identification in the same signal sub-band, which may result in false defects identification, only the peaks which are separated by sufficiently large time-intervals $2\delta T = 2\left(2.66 B_{HP}(SNR)^{1/2}\right)^{-1}$ are to be considered. Note that the $2\delta T$ dependence by the SNR can be neglected for large values range. In Tab. (6.1) and Fig. (6.17) are shown the distance estimation performance in terms of Standard Deviation (SD) and Maximum Error (ME) as function of the SNR, when a random DoA and 100 cases of AWGN are considered, and the bound $\delta R{=}vg(f_c)\delta T = \sqrt{\mathrm{CRLB}_R}$. The SD is near 1[cm] up to 1[dB], whereas the ME is held under 2.5[cm].

Observe that the factor $\sqrt{2}$ to multiply the $\sqrt{\mathrm{SNR}}$ in Eq. (6.18) can be achieved if two measurements are computed considering the same pulse. They rely on the determining when either the leading edge or trailing edge of the pulse crosses the threshold given by the 50% of the pulse peak. Due to dispersion effects, which can arise on large distances, it is more convenient to perform only one measurement for each pulse, determining the time-delay related to the peak value.

6.7.3 Step 3: GPs time-locating

Having designed a *reference bin* for the defects distances estimation and having selected the Gaussian shape for all bins and for the excited pulses are the two basic ingredients to easily time-locate all GPs, related to the same defect. This property involves two steps: first, detect the pulses related to the same defect and then filter them to avoid time-overlapped pulses due to other defects. After that, the pulses spectral integrals can be computed to decode a binary sequence and extract the DoA information.

The detection of a Gaussian pulse by just knowing the dispersion curve of the monitored structure can be done by considering the non-wide bandwidths in wave-vector k_0 of each bins, namely in (angular) frequency ω. The $\omega(k_0)$ function can be approximated via a Taylor expansion to the second order:

$$\begin{aligned} &\omega(k_0) \simeq \omega(k_{0C}) + (k_0 - k_{0C})\omega\prime(kc) + \tfrac{1}{2}(k_0 - k_{0C})^2\omega\prime\prime(k_{0C}) = \\ &= v_p k_{0C} + (k_0 - k_{0C})v_g + +\tfrac{1}{2}(k_0 - k_{0C})^2\Gamma \end{aligned} \tag{6.25}$$

where $\Gamma = \omega\prime\prime(k_{0C})$. Note that in non-dispersive medium, $\omega(k_0) = vk_0$, then $v_p = v_g = v$ and $\Gamma = 0$.

According to the last expansion, discarding the distance attenuation and considering the radial propagation at a certain angle, a Gaussian wave packet propagates along the spatial coordinate r over the time. Therefore, the GP can be written in the complex form as:

$$A(r, t = 0) = f(r) = e^{-\frac{1}{2\sigma_r^2}(r-r_0)^2} e^{jk_{0C}r} \tag{6.26}$$

$$F(k_0) = \frac{\sigma_r}{2\sqrt{\pi}} e^{-\frac{\sigma_r^2}{2}(k_0-k_{0C})^2} e^{jr(k_0-k_{0C})} \tag{6.27}$$

$$A(r,t) = \frac{\sigma_r}{2\sqrt{\pi}} \int e^{-\frac{\sigma_r^2}{2}(k_0-k_{0C})^2} e^{jr_0(k_0-k_{0C})} e^{j(rk_0 - \left[v_p k_{0C} + (k_0-k_{0C})v_g + +\frac{1}{2}(k_0-k_{0C})^2\Gamma\right]t)} dk \tag{6.28}$$

the last integral, is obtained considering the approximation in Eq. (6.25), and it is configured as the IFT of a Gaussian function, due to quadratic term in $k_0 - k_{0C}$ at the exponent. The last integral (excluding all terms which do not depend by k_0) provides:

$$A(r,t) = \exp\left[-\frac{1}{2}\left(\frac{r-(r_0+v_g t)}{\sqrt{\sigma_r^2 - j\Gamma t}}\right)^2\right] e^{jk_{0C}r} e^{-jk_{0C}v_p t} \tag{6.29}$$

It is helpful to pull the j out of the denominator, writing the solution:

$$A(r,t) = \exp\left[-\frac{1}{2}\left(\frac{r-(r_0+v_g t)}{\sigma(t)}\right)^2\right] e^{j\phi(r,t)} \tag{6.30}$$

where

$$\sigma(t) = \sigma_r\sqrt{1+\frac{\Gamma^2}{\sigma_r^4}t^2} \tag{6.31}$$

and

$$\phi(r,t) = k_{0C}r - k_{0C}tv_p - \frac{t\Gamma}{t^2\Gamma^2+\sigma_r^4} \tag{6.32}$$

The solution (6.30) magnitude shows again a Gaussian profile. The packet is centered at $(r_0 + v_g t)$ at time t. The width of the Gaussian profile is given by the $\sigma(t)$ (6.31). Note that the width is increasing with time, as expected, as the Γ term which takes into account the dispersion. The phase $\phi(r,t)$ causes the real solution to oscillate between positive and negative values.

Therefore, if t_{0_i} are the time-instants in which each excited GP peaks, R_{est} is the estimated distance via the *reference bin* pulse, $\delta R_{max}(\mathrm{SNR})$ is the maximum estimation uncertainty (see the Tab. (6.1)), σ_t is the time-width of the considered GP at central frequency f_{c_i}, and $\pm\sigma_{t-disp}$ is the time-width of the same dispersed pulse, a GP can be localized in the following time-window:

$$\left[t_{0_i} + \frac{2R_{est}}{v_g(f_{c_i})} - \sigma_{t-disp}(R_{est}) - \delta R_{max}(\mathrm{SNR})\ ,\ t_{0_i} + \frac{2R_{est}}{v_g(f_{c_i})} + \sigma_{t-disp}(R_{est}) + \delta R_{max}(\mathrm{SNR})\right] \tag{6.33}$$

where

$$\begin{aligned} &\sigma_{t-disp}(R_{est}) = \sigma_t \sqrt{1 + \frac{\Gamma^2}{\sigma_r^4}\left(\frac{2R_{est}}{v_g(f_{c_i})}\right)^2} \\ &\text{with} \quad \begin{cases} \sigma_r = \sigma_t v_g(f_{c_i}) \\ \Gamma = \left.\frac{dv_g(k_0)}{dk_0}\right|_{k_0=k_{0Ci}} \end{cases} \end{aligned} \tag{6.34}$$

Observe that the time-window (6.33), considering just $\pm\sigma_{t-disp}$, covers only the 68% of the GP width. Larger time-windows would reduce the probability of successfully distinguishing reflections generated by defects positioned at similar radial distances.

As conclusion, the duration of the time-window (6.33), related to the worst case (w.c.) pulse, namely the pulse with the narrowest bandwidth, defines the capability to distinguish two signal patterns (when both the defects distance and DoA are to be estimated). Observe that the w.c. pulse provides, without the dispersion effect, an half time-width σ_t equal to 51.85[us]. The corresponding half space-width is given by $\sigma_r = \sigma_t v_g(f_{c_i} = 122[\text{kHz}]) = \simeq 9.9[\text{cm}]$, having $v_g(122[\text{kHz}]) = 1916[\text{m/s}]$. In order to detect two defects, two pulses at the lowest frequency, 122[kHz], have to be detected. This involves a radial resolution, for low dispersion distances, equal to $2\sigma_{r-low-disp} + 2\delta R_{\max}(\text{SNR} \geq 6\text{dB}) \simeq (19.8 + 4)[\text{cm}]$.

6.7.4 Step 4: GPs filtering and spectral integrals

Each time-localized GP (with central frequency equal to f_{c_i}) related to the same defect has to be filter in order to remove all potential spectral components due to other defects pulses which can be superimposed in the time domain. Therefore, 5 FIR filters, designed with a Gaussian window and 250 taps, are used with central frequencies f_{c_i} and bandwidths B_{HP_i} given by the values (6.24).

The FFT of a *short-time window* composed by each (filtered) GP related to the same defect is computed. It, in turn, provides a short frequency-window w.r.t. the FFT of the acquired signal one. 4000 samples were considered to achieve a frequency resolution Δf equal to 500Hz. Subsequently, the pulses spectral integrals are computed within the bandwidths B_{HP_i}. It is worth noting that is more convenient to compute the spectral-integral rather than the time-integrals. In fact, the GPs widen and decrease over time, due to the dispersion effect, becoming more sensitive to the noise.

6.7.5 Step 5: GPs binary decoding and DoA estimation performance

In order to evaluate which pulses, related to the same defect, are to be decoded to 1 or 0 values, a suitable cost function was implemented. It was defined so that a fix optimal threshold value can be found, independently by the defect distance and the GPs energy (which is imposed the same for all GPs via the the excitation signal). For this purpose, the amplitude spectral integral is computed also for the pulse related to the *reference bin*, used firstly to estimate the defect distance. Therefore, the following cost function was defined:

$$CF(I_{S_{i-Bin}}) = \frac{I_{S_{i-Bin}}}{I_{S_{\mathrm{Ref}-Bin}}} \tag{6.35}$$

where $I_{S_{i-Bin}}$ is the spectral integral related to the $i-th$ GP/Bin and $I_{S_{\mathrm{Ref}-Bin}}$ is the spectral integral related to the reference bin of a certain signal pattern. Therefore, the $i-th$ Bit of the bits sequence, corresponding to a binary pulses sequence, is set to 0 or 1 according to the rule:

$$\begin{cases} Bit_i = 1 \quad if \quad CF(I_{S_{i-Bin}}) \geq r_{th} \\ Bit_i = 0 \quad if \quad CF(I_{S_{i-Bin}}) < r_{th} \end{cases} \tag{6.36}$$

The optimum value of the threshold r_{th} was found by using the theoretical model. It is computed as:

$$r_{th} = \min_{m} \left[\min_{i,j} \left(\frac{1}{2} \frac{I_{S_{m,i}} - I_{S_{m,j}}}{I_{S_{\mathrm{Ref}-Bin}}} \right) \right] \tag{6.37}$$

where the indexes i and j are related, respectively, to the Bin set to 1 and 0 at direction $m-th$. Therefore, according to the direction $m-th$, moving between 0 and 179 (considering a 1[deg] angular step discretization) the indexes i and j can move from 1 to a maximum of 5, when their sum is always equal to 5. Therefore, the Eq. (6.37), finds the optimal threshold r_{th} by computing the minimum spectral integrals difference between each couple of Bins set to 1 and 0 for all direction m. Then, the minimum value is computed among all directions, indexed by m.

Observe that, due to quantization non-idealities, the procedure (6.37) could output very small threshold values. Indeed, there is no sharp transition of the directivity function from 0 to 1 or vice-versa, moving along the polar coordinates. Therefore, without modifying the notation of (6.37), for each 6[deg] discrete angular step, $\Delta\theta_l$, the Bins set to 1, (with integrals $I_{\Delta\theta_l - S_{m,i}}$) which are preceded and/or followed by a Bin set to 0, moving along the polar coordinate, were excluded in the procedure (6.37). In the same way, the Bins set to 0, (with integrals $I_{\Delta\theta_l - S_{m,j}}$) which are preceded and/or followed by a Bin set to 1, moving along the polar coordinate, were excluded. In other words, we admit a sequence/symbol error between two adjacent configuration, particularly when the direction $m - th$ is near to a direction placed between two different 6° discrete angular steps. The Eq. (6.37) provides the optimum threshold value $r_{th} = 0.4751$.

Note that the cost function (6.35) follows the minimum distance in spectral integral for each Bin. This is a sub-optimal signal pattern estimation method (in time or frequency domain). The optimal method, provided by the Digital Communication Theory [91], finds the minimum distance between the spectrum of the acquired signal (the pulses train) and all possible spectral configurations (minimum *Euclidean distance* rule)). Therefore, for the designed S-SAT, at least 30 configurations are to be considered, with an associated increased processing complexity equal to 30 factor.

After all pulses of a signal pattern are decoded, a bit-sequence is obtained. The last one determine uniquely the associated 6[deg] discrete angular step.

The numeric results, obtained by considering 100 cases of simulated AWGN at different SNR values, and covering the 180° angular range with 1[deg] step, are given in Table (6.2) and in the Fig. (6.18), in terms of Standard Deviation and Maximum error values. Observe that Maximum errors were computed considering the middle angle of the estimated discrete angular step as the estimated angle. They show that the Standard Deviation value is less than to 2[deg], up to 10dB SNR value, while the Maximum Error vaue is limited to 8[deg].

In order to express the last result in terms of mainlobe-width, an equivalent average mainlobe can be defined. To this aim, it can be assumed that the probability function of $\theta - \theta_{est}$, with θ the "true" DoA value and θ_{est} the middle angle of the 6° discrete angular steps, is approximately Gaussian. The last assumption

SNR (dB)	Standard Deviation [deg]	Maximum Error [deg]	DoA estimation error ≥ 5[deg] probability
18	2	5	0.0101
16	2	5	0.0103
14	1.99	5	0.0092
12	1.99	5	0.008
11	1.98	7	0.0074
10	1.98	8	0.0068
9	1.99	10	0.0084
8	2.08	43	0.0124
7	2.37	51	0.0252
6	3.48	160	0.0516

Table 6.2: Defect DoA estimation performance for different values of the SNR (with: semi-round angle cover with a 1[deg] step; 100 AWGN simulated cases; removed distance attenuation).

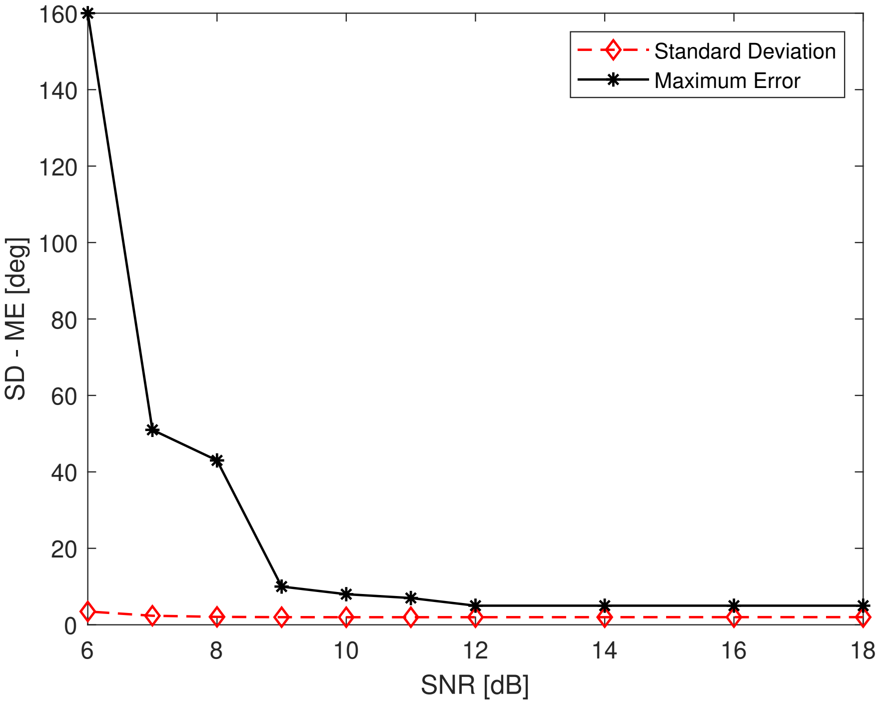

Figure 6.18: Defect DoA estimation performance plots (related to the Tab. (6.2) values) in terms of Standard Deviation and Maximum Error, as function of the SNR.

is justified considering that a binary sequence is well defined in the middle of a discrete angular step, and moving to the left and right adjacent angular steps, changes smoothly via a single Bin. Therefore, considering a mainlobe aperture which provides a 95% probability that the DoA is within it, the beamwidth is given by $\pm 1.96 \cdot 2$[deg] $\simeq \pm 4$[deg], namely a 8[deg] average aperture. Finally, observe that the probability that the DoA "error" is equal or higher than 5[deg], for a 10dB SNR, is less than 0.01%. The last one means that there is a small number of angles (namely 4 or 5 dependently by the noise case) which involve a wider equivalent maninlobe aperture. Future quantization procedure developments are aimed to remove these critical directions, at least for high-medium SNR values.

6.8 S-SAT: conclusions

Conventional solutions for Ultrasound active monitoring, such as the interdigited transducers or phased arrays, are typically limited by some issues. In particular, interdigited transducers have a fixed directionality, while phased arrays require many sensors, with a consequent large amount of data to be stored and processed. Therefore, phased arrays are unsuitable for low power applications, where the sensor nodes are battery-powered and wireless, in order to reduce the weight penalty due to cabling, a very important feature in the aeronautical or aerospace domains. In order to overcome the previous limits, single piezo-transducer can be designed so that all monitored structure can be scanned. This strategy was already used to design the, so called, F-SAT Transducer ([2]), but this solutions has some limitations in terms of defects localization, due to the wide mainlobe aperture, which increases when multiple frequencies are excited to better estimate the defects distances. Furthermore, it shows a 180° ambiguity when a defect is detected. In this Chapter, a design-procedure to remove the ambiguity issue was illustrated, with the aim to achieve a better defects localization capability, a novel design philosophy was devised to originate a new transducer, called S-SAT. It was designed to perform a simultaneous 180° scan and to associate a different signal pattern configuration for different discrete angular steps. In other words, the new monitoring system was designed according to the Encoder system principles.

Able to detect broadband defects, with size larger than 1[cm], it can be estimate the number of defects and their distances with a radial accuracy near to 2[cm], even for low SNR values. However, in presence of multiple-defects, to ensure a correct estimation both the defect distance and the its angle coordinate, the radial resolution decreases to about 24[cm], for low dispersion distances. When large distances are covered the last value increases, unless dispersion compensation procedures are applied for a pulse compression, allowing to fix the request minimum radial gap between two defects, independently by the covered distance.

The DoA estimation performance ensures an 8[deg] equivalent average beamwidth when the SNR is equal or grater than 10[dB], whereas a 16[deg] maximum apeture is limited just to few critical DoAs (namely, 4 or 5 directions according to the particular noise case).

The peculiar S-SAT design criterion and the excitation signal given by a Gaussian pulses train are so that the computational cost for multiple-defects distances and angles estimation is kept low. Only one FFT and IFFT and one peaks detection and Cross-correlation procedure are requested on the acquired long-lasting signal. Further signal processing is performed on short-time window, with a consequent low computational cost. Therefore, the S-SAT results to be very suitable for embedded applications which uses micro-controller units with limited processing capabilities and Wi-Fi-battery powered.

Observe that multiple DoAs are estimated at the same time, due the 180° simultaneous scan. Therefore, the low radial achieved resolution for multiple defects localization could limit the number of defects to be localize. This issue can be overcome under the hypothesis of periodic scans and that few new defects rise between two subsequent scans. When a defect is detected, its signal can be summed to the baseline signal. Thus, by applying the differential signal method, namely the *baseline subtraction*, new radial defects can be detected, during subsequent scans. Furthermore, three or more S-SATs, placed at different angles, can provide a majority report on the defect coordinates estimation. This means that if two defects are not actually neighbors, an S-SAT could "see" them radially too near to correctly estimate also their angular coordinates. Vice versa other S-SATs can "see" the two defects radially far, according to their positioning w.r.t. to the defects one. Therefore, set a single polar reference systems, when the defect estimated radial coordinate is the same, the angle coordinate can be selected as the most recurring estimated angle value among the S-SAT transducers.

Future developments are aimed to improve the quantization procedure, in order to exploit all available bandwidth, increasing the radial resolution, and minimizing the equivalent mainlobe aperture.

Chapter 7

Conclusions

This dissertation has illustrated the research work conducted to develop sensor systems in the ultrasonic SHM context. Both real-time monitoring and periodically activated inspection system were investigated and the sensors design paradigms were adapted, as well as the signal processing, to achieve improved performance in damage detection and ranging by using low power embedded devices. More specifically, the research work and the novel contributions can be summarized as follows:

- The first research part focused on passive SHM for damage/impacts localisation via Guided Waves in thin-wall structures (e.g. aircraft shells), by taking advantage of their large distances coverage with a low attenuation. The proposed method uses arrays of closely located piezo-sensors able to estimate the wave-front directions of arrival (DoAs) on each ones. Such solution was selected because it paves the way to low computational cost processing procedures and because it is suitable both for isotropic and anisotropic structures, being unknown the material properties. In order to minimize the corruption of noise generated by different sources (such as structural vibrations, noisy acquisition channels, noisy electronic devices etc.), unconventional shaped sensors were designed. The exploited shaping design procedure allowed to achieve the same sensors frequency response, avoiding the wavenumber tuning effect. An optimality criterion based on the Theory of Measurements and the Calculus of Variations was defined and applied to the case of three sensors array. The obtained array, refereed to as *Optimal Cluster of Shaped Sensors* (SS-OC), showed improved performance w.r.t. the *Standard Cluster* composed by three disk-sensors [16], when the acquired signals are affected by noise, especially for medium-low PSNR values.

- A more refined optimality criterion was defined starting by the system model, a model for the noise (i.e. AWGN), the Estimation Theory (i.e. the Cramér–Rao bound (CRB)) and considering the wave velocity unknown. It allows to find the optimal sensors shapes or the optimal disk-sensors positioning for a generic number M of array piezo-loads, to minimize the error in DoA estimation. It was applied again to the case of a three sensors array, and the optimal arrangement of disk-sensors within a restricted array area, i.e. a circle of fixed radius, was derived. The generated array was called *Optimal Cluster of Disk-Sensors* (DS-OC). An efficient DoA estimator, able to attain the minimized CRB of the unknown wave-velocity case, was found. It is based on the *Gauss-Markov* time-delays estimator. Moreover, it was shown that the proposed criterion is optimal also to design the *phased array* used in the active SHM context, when the parameters distance r, angle θ and velocity v are to be estimated.

- In order to address another well-known issue, namely the edge reflections/reverberation, the piezo-reshaping was used to design a novel array base sensor, referred to as *Directive Complex Sensor* (DCS). Requiring just two differential acquiring channels, it is able to filter undesired directional interference which impinging from DoAs out of the monitored angles work-range. Its directivity properties were assessed via a double numerical validation: the DCS theoretical beampatterns match the numeric ones provided by the Green's Functions (GFs) formalism simulations and the FEM ones. Thus, FEM simulations, which are able to provide results very tight to the experimental ones, validated the (GFs) simulator, widely used to assess the proposed sensor systems.

- In active SHM context, the double-phase design procedure [3], aimed at exciting directional waves, was investigated. Such procedure was linked to the less general procedure proposed in [2], which doesn't allow to avoid the 180° ambiguity during an acoustic inspection.

- Following the previous well-defined procedure, a novel single Transducer, called *Spectrum Scanning Acoustic Transducer* (S-SAT), was designed to overcome the hardware complexity required by the conventional phased array solution and the limited F-SAT performance (see [66, 81]) in defects detection and localization. Improved performance are achieved in detectable defects size (1[cm] versus 2[cm]) and angle accuracy (8° versus about 18°). At the same time the computational cost is limited. Only one cross-correlation procedure is required, and up to 180° are simultaneously inspected. Additional signal processing procedures are performed on short-time windows, thus minimizing the computational cost.

7.1 Future work developments

The research work described in this dissertation open the way to future developments to further increase the proposed sensory systems performance:

- The *Directive Complex Sensor* (DCS) directivity properties can be increased by applying the *halftoning* quantization technique already used to generate the S-SAT.
- Thanks to the high potential of Artificial Intelligence techniques to improve the DoA estimation performance via the reflections of boundaries, future developments are aimed to understand if M-L algorithms can result useful for low power consumption embedded electronic devices and compare their DoA estimation performance with the one achievable by a DCSs cluster.
- A sensor quantization technique able to work in polar coordinate, with an appropriate error filter, can be devoloped in order to increase both the angular resolution and the radial one (i.e. the necessary radial gap, to distinguish two defects, can be reduced).

- Similarly to the the Frequency-Time analysis tool, the sensor quantization procedure could be performed in the 4D $r - k$ space, namely in the 2D $\rho - k$ plane for each DoA (by using the transducer RT), in order to achieve the desired directivity function simultaneously in the time and in frequency domain. This strategy may be useful to design *Spread Spectrum* transducers, able to increase the radial and angular accuracy and, at the same time, minimize the interference due to signals excited by other transducers.

- The investigated design procedure to excite directional waves via a single Transducer led to peculiar even and odd symmetry piezo-patches properties. The last ones may used to reduce the patches area and the manufacturing costs.

- A physics-math model for quantized mechanical guided waves, i.e. a *phonons model*, can be defined. It could be used to do sensor-design, in order to achieve *super resolution* in damages localization.

Author's publications

1. Luca De Marchi, Marco Dibiase, and Nicola Testoni. "Piezoelectric Sensors for Lamb waves' Direction of Arrival (DoA) Estimation". In: Proceedings. Vol. 2. 13. MDPI. 2018, p. 806.
2. Marco Dibiase and Luca De Marchi. "Clusters of Shaped Ultrasonic Transducers for Lamb waves' DoA Estimation". In: Applied Sciences 10.22 (2020), p. 8150.
3. Marco Dibiase, Masoud Mohammadgholiha, and Luca De Marchi. "Optimal Array Design and Directive Sensors for Guided Waves DoA Estimation". In: Sensors 22.3 (2022), p. 780.
4. Marco Dibiase and Luca De Marchi. "An optimal shaped sensor array derivation". Submitted to Micromachines Journal (MDPI)

Personal contributes of each publication:

1. Luca De Marchi, Marco Dibiase, and Nicola Testoni. "Piezoelectric Sensors for Lamb waves' Direction of Arrival (DoA) Estimation". In: Proceedings. Vol. 2. 13. MDPI. 2018, p. 806.
    - Design of a reference sensor (in the Radon Transform domain) of a 3-shaped sensor array, so that the wave-fronts DoA can be estimated without knowing the wave velocity.
    - The numerical validation of the proposed cluster by exploiting the Green's function (GFs) formalism (the MATLAB scripts were provided by L. De Marchi). The last method was properly modified in order to compute the piezo-sensors voltage due to the sensor strain.

2. Marco Dibiase and Luca De Marchi. "Clusters of Shaped Ultrasonic Transducers for Lamb waves' DoA Estimation". In: Applied Sciences 10.22 (2020), p. 8150.
    - The Theory of Propagation of Uncertainty was investigated in order to re-define a 3-shaped sensors cluster so that the following points are simultaneously satisfied:
        - the DoA can be estimated as linear function of a time-delays ratio.
        - the DoA estimation uncertainty is minimized and the theoretical estimation bounds are derived.
        - the dimensions of the transducers and the time-delays estimation computational cost are minimized.
    - The numerical tests of the proposed cluster (by exploiting the GFs formalism) and the assessment of the improved DoA estimation performance w.r.t. a cluster of 3 disk-sensors.
3. Marco Dibiase, Masoud Mohammadgholiha, and Luca De Marchi. "Optimal Array Design and Directive Sensors for Guided Waves DoA Estimation". In: Sensors 22.3 (2022), p. 780.
    - The main methods for AS localisation were reviewed.
    - The main algorithms already proposed in literature for the DoA estimation in presence of directional interference (e.g. edge reflections) were reviewed.
    - A general N-sensor array design procedure was defined so that the DoA Cramér-Rao Bound is minimized, in *Bayesian* sense, when the wave velocity is considered to be unknown. Therefore, the system model and the cost function to be minimized were provided and specialized in the case of a 3-sensor array. For the last one, the optimal solution was found via the Lagrange multipliers method.
    - An efficient DoA estimator is found based on the time-delays Gauss-Markov estimator for a three sensors array.

- The Designed *Disk Sensor Optimal Cluster* (DS-OC) and the DoA estimator were validated by numerical simulations and compared, respectively, with a conventional cluster and other sub-optimal estimators.
- A novel *Directive Complex Sensor* (DCS) for guided waves was designed to cancel out undesired Acoustic Emissions impinging from DoAs out of the given angles range (e.g. edge reflections).
- The DCS theoretical beampatterns were compared with the ones obtained by the GFs simulations. The bempatterns matching was shown.
- Research joint efforts led also to the matching of beampatterns obtained by FEM simulations (the last ones were ran by M. Mohammadgholiha).
- GFs simulations were ran in presence of directional interference and noise considering an Optimal Cluster of DCS. They showed the DCS ability to drastically reduce the undesired spurious waves, allowing to estimate the DoA of the useful signal affected by noise.

4. Marco Dibiase and Luca De Marchi. "An optimal shaped sensor array derivation". Submitted to Micromachines Journal (MDPI).

    - The problem of designing the arrangement and shape of acoustical sensors was reconsidered by defining an optimality criterion based on Theory of Measurements.
    - The DoA minimum variance problem statement was addressed by the tools provided by advanced analysis, i.e. the Calculus of Variations for functionals.
    - The re-shaping procedure based on the Radon Transform (RT) tool, already employed in [1,2] to address the different wave number filtering among differently shaped sensors, was in more detail reviewed, providing the physical meaning of the sensors RT, i.e. an equivalent 1D piezo-load distribution able to provide the same effect of the in plane 2D piezo-load.
    - The *Error diffusion* technique (ideated by De Marchi et al.[3]) was applied to quantise the ideal sensors shape functions, provided by the re-shaping procedure.

- Different DoA estimators based on four different time-delays estimators were illustrated and discussed.
- Synthetic noisy signals were used in order to assess the expected 50% reduction of the Standard Deviation (SD) in DoA estimations via the designed *Shaped Sensors Optimal Cluster*(SS-OC) w.r.t. a Standard Cluster of piezo-disks.
- The numeric results were discussed and compared with the ones obtained in the previous work [3] via the DS-OC.

Bibliography

[1] Josef Krautkrämer and Herbert Krautkrämer. “Ultrasonic testing by determination of material properties”. In: *Ultrasonic Testing of Materials*. Springer, 1990, pp. 528–550.

[2] Matteo Senesi and Massimo Ruzzene. “A frequency selective acoustic transducer for directional Lamb wave sensing”. In: *The Journal of the Acoustical Society of America* 130.4 (2011), pp. 1899–1907.

[3] Luca De Marchi, Nicola Testoni, and Alessandro Marzani. *Device, method and system for real time structural diagnostics with guided elastic waves*. US Patent 10,914,711. Feb. 2021.

[4] Christopher B Scruby. “An introduction to acoustic emission”. In: *Journal of Physics E: Scientific Instruments* 20.8 (1987), p. 946.

[5] Horace Lamb. “On waves in an elastic plate”. In: *Proceedings of the Royal Society of London. Series A, Containing papers of a mathematical and physical character* 93.648 (1917), pp. 114–128.

[6] Ryan P Dalton, Peter Cawley, and Michael JS Lowe. “The potential of guided waves for monitoring large areas of metallic aircraft fuselage structure”. In: *Journal of Nondestructive Evaluation* 20.1 (2001), pp. 29–46.

[7] Victor Giurgiutiu and Adrian Cuc. “Embedded non-destructive evaluation for structural health monitoring, damage detection, and failure prevention”. In: *Shock and Vibration Digest* 37.2 (2005), p. 83.

[8] Mathias Fink. “Time reversal of ultrasonic fields. I. Basic principles”. In: *IEEE Transactions on Ultrasonics, Ferroelectrics, and Frequency Control* 39.5 (1992), pp. 555–566.

[9] Hyun Woo Park, Hoon Sohn, Kincho H Law, and Charles R Farrar. “Time reversal active sensing for health monitoring of a composite plate”. In: *Journal of Sound and Vibration* 302.1-2 (2007), pp. 50–66.

[10] Ros K Ing and Mathias Fink. “Time-reversed Lamb waves”. In: *IEEE Transactions on Ultrasonics, Ferroelectrics, and Frequency Control* 45.4 (1998), pp. 1032–1043.

[11] Francesco Ciampa and Michele Meo. “Impact detection in anisotropic materials using a time reversal approach”. In: *Structural Health Monitoring* 11.1 (2012), pp. 43–49.

[12] Yiu-Tong Chan and KC Ho. “A simple and efficient estimator for hyperbolic location”. In: *IEEE Transactions on signal processing* 42.8 (1994), pp. 1905–1915.

[13] Karl F Graff. *Wave motion in elastic solids*. Courier Corporation, 2012.

[14] Alessandro Perelli et al. “Best basis compressive sensing of guided waves in structural health monitoring”. In: *Digital Signal Processing* 42 (2015), pp. 35–42.

[15] Fikret Sivrikaya and Bülent Yener. “Time synchronization in sensor networks: a survey”. In: *IEEE network* 18.4 (2004), pp. 45–50.

[16] T Kundu. “A new technique for acoustic source localization in an anisotropic plate without knowing its material properties”. In: *Proceedings of the 6th European Workshop on Structural Health Monitoring, Dresden, Germany*. 2012, pp. 3–6.

[17] Tribikram Kundu. “Acoustic source localization”. In: *Ultrasonics* 54.1 (2014), pp. 25–38.

[18] Tribikram Kundu, Hayato Nakatani, and Nobuo Takeda. “Acoustic source localization in anisotropic plates”. In: *Ultrasonics* 52.6 (2012), pp. 740–746.

[19] Ferdinand Van Der Heijden, Robert P Duin, Dick De Ridder, and David MJ Tax. *Classification, parameter estimation and state estimation: an engineering approach using MATLAB*. John Wiley & Sons, 2005.

[20] XE Gros, K Takahashi, and M de Smet. “On the efficiency of current NDT methods for impact damage detection and quantification in thermoplastic toughened CFRP materials”. In: *Journal of Nondestructive Testing & Ultrasonics(Germany)* 4.3 (1999).

[21] Won Hyun Park, Pawel Packo, and Tribikram Kundu. “Acoustic source localization in an anisotropic plate without knowing its material properties–a new approach”. In: *Ultrasonics* 79 (2017), pp. 9–17.

[22] Novonil Sen and Tribikram Kundu. “A new wave front shape-based approach for acoustic source localization in an anisotropic plate without knowing its material properties”. In: *Ultrasonics* 87 (2018), pp. 20–32.

[23] Dirk Aljets, Alex Chong, Steve Wilcox, and Karen Holford. “Acoustic emission source location on large plate-like structures using a local triangular sensor array”. In: *Mechanical Systems and Signal Processing* 30 (2012), pp. 91–102.

[24] Stephen Grigg et al. “Development of a low-power wireless acoustic emission sensor node for aerospace applications”. In: *Structural Control and Health Monitoring* 28.4 (2021), e2701.

[25] Howard M Matt and Francesco Lanza di Scalea. “Macro-fiber composite piezoelectric rosettes for acoustic source location in complex structures”. In: *Smart Materials and Structures* 16.4 (2007), p. 1489.

[26] Emanuele Baravelli et al. “Double-channel, frequency-steered acoustic transducer with 2-D imaging capabilities”. In: *IEEE Transactions on Ultrasonics, Ferroelectrics, and Frequency Control* 58.7 (2011), pp. 1430–1441.

[27] Fred K Gruber, Edwin A Marengo, and Anthony J Devaney. “Time-reversal imaging with multiple signal classification considering multiple scattering between the targets”. In: *The Journal of the Acoustical Society of America* 115.6 (2004), pp. 3042–3047.

[28] Marco Dibiase and Luca De Marchi. “Clusters of Shaped Ultrasonic Transducers for Lamb Waves’ DoA Estimation”. In: *Applied Sciences* 10.22 (2020), p. 8150.

[29] Charles Knapp and Glifford Carter. “The generalized correlation method for estimation of time delay”. In: *IEEE transactions on acoustics, speech, and signal processing* 24.4 (1976), pp. 320–327.

[30] Harry H Ku et al. “Notes on the use of propagation of error formulas”. In: *Journal of Research of the National Bureau of Standards* 70.4 (1966), pp. 263–273.

[31] Victor Giurgiutiu. “Tuned Lamb wave excitation and detection with piezoelectric wafer active sensors for structural health monitoring”. In: *Journal of intelligent material systems and structures* 16.4 (2005), pp. 291–305.

[32] Luca De Marchi, Alessandro Perelli, and Alessandro Marzani. “A signal processing approach to exploit chirp excitation in Lamb wave defect detection and localization procedures”. In: *Mechanical Systems and Signal Processing* 39.1-2 (2013), pp. 20–31.

[33] Tony Gustafsson, Bhaskar D Rao, and Mohan Trivedi. “Source localization in reverberant environments: Modeling and statistical analysis”. In: *IEEE Transactions on Speech and Audio Processing* 11.6 (2003), pp. 791–803.

[34] JM Perez-Lorenzo et al. “Evaluation of generalized cross-correlation methods for direction of arrival estimation using two microphones in real environments”. In: *Applied Acoustics* 73.8 (2012), pp. 698–712.

[35] Stanley R Deans. *The Radon transform and some of its applications*. Courier Corporation, 2007.

[36] Peter Toft. “The radon transform”. In: *Theory and Implementation (Ph. D. Dissertation)(Copenhagen: Technical University of Denmark)* (1996).

[37] Jack D Gaskill. *Linear systems, Fourier transforms, and optics*. Vol. 576. Wiley New York, 1978.

[38] Massimo Rudan. *Physics of semiconductor devices*. Springer, 2015.

[39] Izrail Moiseevitch Gelfand, Richard A Silverman, et al. *Calculus of variations*. Courier Corporation, 2000.

[40] Thomas D Kite, Brian L Evans, and Alan C Bovik. “Modeling and quality assessment of halftoning by error diffusion”. In: *IEEE Transactions on Image Processing* 9.5 (2000), pp. 909–922.

[41] Daniel L Lau, Gonzalo R Arce, and Neal C Gallagher. “Green-noise digital halftoning”. In: *Proceedings of the IEEE* 86.12 (1998), pp. 2424–2444.

[42] Lorenzo Capineri, Alessandro Gallai, and Leonard Masotti. “Design criteria and manufacturing technology of piezo-polymer transducer arrays for acoustic guided waves detection”. In: *2002 IEEE Ultrasonics Symposium, 2002. Proceedings.* Vol. 1. IEEE. 2002, pp. 857–860.

[43] Filippo Bellan et al. “A new design and manufacturing process for embedded Lamb waves interdigital transducers based on piezopolymer film”. In: *Sensors and Actuators A: Physical* 123 (2005), pp. 379–387.

[44] Emanuele Baravelli et al. “Inkjet fabrication of spiral frequency-steerable acoustic transducers (FSATs)”. In: *Health Monitoring of Structural and Biological Systems 2012.* Vol. 8348. International Society for Optics and Photonics. 2012, p. 834817.

[45] Emanuele Baravelli, Matteo Senesi, Massimo Ruzzene, and Luca De Marchi. “Fabrication and characterization of a wavenumber-spiral frequency-steerable acoustic transducer for source localization in plate structures”. In: *IEEE Transactions on Instrumentation and Measurement* 62.8 (2013), pp. 2197–2204.

[46] Masoud Mohammadgholiha et al. “Finite element modeling and experimental characterization of piezoceramic frequency steerable acoustic transducers”. In: *IEEE Sensors Journal* 22.14 (2022), pp. 13958–13970.

[47] Marco Dibiase, Masoud Mohammadgholiha, and Luca De Marchi. “Optimal Array Design and Directive Sensors for Guided Waves DoA Estimation”. In: *Sensors* 22.3 (2022), p. 780.

[48] Ulkü Oktel and Randolph L Moses. “A Bayesian approach to array geometry design”. In: *IEEE transactions on signal processing* 53.5 (2005), pp. 1919–1923.

[49] W Hahn and S Tretter. “Optimum processing for delay-vector estimation in passive signal arrays”. In: *IEEE Transactions on Information Theory* 19.5 (1973), pp. 608–614.

[50] Luigi Malagò and Giovanni Pistone. “Information geometry of the Gaussian distribution in view of stochastic optimization”. In: *Proceedings of the 2015 ACM Conference on Foundations of Genetic Algorithms XIII*. 2015, pp. 150–162.

[51] Anthony Atkinson, Alexander Donev, and Randall Tobias. *Optimum experimental designs, with SAS*. Vol. 34. Oxford University Press, 2007.

[52] Brian Beavis and Ian Dobbs. *Optimisation and stability theory for economic analysis*. Cambridge university press, 1990.

[53] U Oktel and Randolph L Moses. “Source localization with isotropic arrays”. In: *IEEE Signal Processing Letters* 11.5 (2004), pp. 501–504.

[54] Hagit Messer. “Source localization performance and the array beampattern”. In: *Signal Processing* 28.2 (1992), pp. 163–181.

[55] J Albuquerque. “The Barankin bound: A geometric interpretation (Corresp.)” In: *IEEE Transactions on Information Theory* 19.4 (1973), pp. 559–561.

[56] R McAulay and E Hofstetter. “Barankin bounds on parameter estimation”. In: *IEEE Transactions on Information Theory* 17.6 (1971), pp. 669–676.

[57] Saeed V Vaseghi. “Spectral subtraction”. In: *Advanced Signal Processing and Digital Noise Reduction*. Springer, 1996, pp. 242–260.

[58] Cha Zhang, Dinei Florêncio, and Zhengyou Zhang. “Why does PHAT work well in lownoise, reverberative environments?” In: *2008 IEEE International Conference on Acoustics, Speech and Signal Processing*. IEEE. 2008, pp. 2565–2568.

[59] Ralph Schmidt. “Multiple emitter location and signal parameter estimation”. In: *IEEE transactions on antennas and propagation* 34.3 (1986), pp. 276–280.

[60] Haiyun Xu et al. “Direction-of-arrival estimation for both uncorrelated and coherent signals in coprime array”. In: *IEEE Access* 7 (2019), pp. 18590–18600.

[61] Koby Todros and Alfred O Hero. “Robust multiple signal classification via probability measure transformation”. In: *IEEE Transactions on Signal Processing* 63.5 (2015), pp. 1156–1170.

[62] Sina Hafezi, Alastair H Moore, and Patrick A Naylor. “Multiple DOA estimation based on estimation consistency and spherical harmonic multiple signal classification”. In: *2017 25th European Signal Processing Conference (EUSIPCO)*. IEEE. 2017, pp. 1240–1244.

[63] Gengxin Ning, Bowen Wang, Changku Zhou, and Yizhi Feng. “A velocity independent MUSIC algorithm for DOA estimation”. In: *2017 IEEE International Conference on Signal Processing, Communications and Computing (ICSPCC)*. IEEE. 2017, pp. 1–4.

[64] Ethem Alpaydin. *Introduction to machine learning*. MIT press, 2020.

[65] Joseph Melville, K Supreet Alguri, Chris Deemer, and Joel B Harley. “Structural damage detection using deep learning of ultrasonic guided waves”. In: *AIP conference proceedings*. Vol. 1949. 1. AIP Publishing LLC. 2018, p. 230004.

[66] Matteo Senesi, Buli Xu, and Massimo Ruzzene. “Experimental characterization of periodic frequency-steerable arrays for structural health monitoring”. In: *Smart Materials and Structures* 19.5 (2010), p. 055026.

[67] MATLAB. *version R2017b*. Natick, Massachusetts: The MathWorks Inc., 2017.

[68] COMSOL Multiphysics. *Comsol Multiphysics Reference Manual: Version 5.6*. 2014.

[69] B Lin and Victor Giurgiutiu. “Modeling and testing of PZT and PVDF piezoelectric wafer active sensors”. In: *Smart Materials and Structures* 15.4 (2006), p. 1085.

[70] Arun K Ramanathan, Leon M Headings, and Marcelo J Dapino. “Near static strain measurement with piezoelectric films”. In: *Sensors and Actuators A: Physical* 301 (2020), p. 111654.

[71] Jont B Allen and David A Berkley. “Image method for efficiently simulating small-room acoustics”. In: *The Journal of the Acoustical Society of America* 65.4 (1979), pp. 943–950.

[72] Lorenzo Capineri and Andrea Bulletti. *Interdigitated ultrasonic transducer*. Patent Number WO 2022/200980 A1. 2022.

[73] Mohammad A Moetakef, Shiv P Joshi, and Kent L Lawrence. “Elastic wave generation by piezoceramic patches”. In: *AIAA journal* 34.10 (1996), pp. 2110–2117.

[74] K Diamanti, JM Hodgkinson, and C Soutis. “Damage detection of composite laminates using PZT generated Lamb waves”. In: *1st European workshop on structural health monitoring*. 2002, pp. 398–405.

[75] Lingyu Yu and Victor Giurgiutiu. “In situ 2-D piezoelectric wafer active sensors arrays for guided wave damage detection”. In: *Ultrasonics* 48.2 (2008), pp. 117–134.

[76] WAK Deutsch, A Cheng, and JD Achenbach. “Self-focusing of Rayleigh waves and Lamb waves with a linear phased array”. In: *Journal of Research in Nondestructive Evaluation* 9.2 (1997), pp. 81–95.

[77] Willi G Schwarz et al. “Lamb wave tomographic imaging system for aircraft structural health assessment”. In: *Nondestructive Evaluation of Aging Aircraft, Airports, and Aerospace Hardware III*. Vol. 3586. SPIE. 1999, pp. 292–296.

[78] Victor Giurgiutiu and Jingjing Bao. “Embedded-ultrasonics structural radar for nondestructive evaluation of thin-wall structures”. In: *ASME International Mechanical Engineering Congress and Exposition*. Vol. 36258. 2002, pp. 333–340.

[79] Matteo Senesi, Emanuele Baravelli, Luca De Marchi, and Massimo Ruzzene. “Experimental demonstration of directional GW generation through wavenumber-spiral Frequency Steerable Acoustic Actuators”. In: *2012 IEEE International Ultrasonics Symposium*. IEEE. 2012, pp. 2694–2697.

[80] M.I. Skolnik. *Introduction to Radar Systems*. Electrical engineering series. McGraw-Hill, 2001. ISBN: 9780071181891.

[81] Octavio A Márquez Reyes et al. "A Numerical Study on Baseline-Free Damage Detection Using Frequency Steerable Acoustic Transducers". In: *European Workshop on Structural Health Monitoring.* Springer. 2023, pp. 24–33.

[82] David Slepian. "Estimation of signal parameters in the presence of noise". In: *Transactions of the IRE Professional Group on Information Theory* 3.3 (1954), pp. 68–89.

[83] AJ Mallinckrodt and TE Sollenberger. "Optimum pulse-time determination". In: *Transactions of the IRE Professional Group on Information Theory* 3.3 (1954), pp. 151–159.

[84] Anthony J Weiss. "Composite bound on arrival time estimation errors". In: *IEEE Transactions on Aerospace and Electronic Systems* 6 (1986), pp. 751–756.

[85] Trevor Lloyd Wadley. "Electronic principles of the Tellurometer". In: *Transactions of the South African Institute of Electrical Engineers* 49.5 (1958), pp. 143–172.

[86] D.E. Knuth. *The Art of Computer Programming, Volume 4A: Combinatorial Algorithms, Part 1.* pt. 1. Pearson Education, 2014. ISBN: 9780133488852.

[87] Robert W Floyd. "An adaptive algorithm for spatial gray-scale". In: *Proc. Soc. Inf. Disp.* Vol. 17. 1976, pp. 75–77.

[88] Guoqiang Liu, Yingchun Xiao, Hua Zhang, and Gexue Ren. "Baseline signal reconstruction for temperature compensation in lamb wave-based damage detection". In: *Sensors* 16.8 (2016).

[89] Ahmad B Zoubi, Sungwon Kim, Daniel O Adams, and V John Mathews. "Lamb wave mode decomposition based on cross-Wigner-Ville distribution and its application to anomaly imaging for structural health monitoring". In: *IEEE Transactions on Ultrasonics, Ferroelectrics, and Frequency control* 66.5 (2019), pp. 984–997.

[90] Marc Niethammer, Laurence J Jacobs, Jianmin Qu, and Jacek Jarzynski. "Time-frequency representations of Lamb waves". In: *The Journal of the Acoustical Society of America* 109.5 (2001), pp. 1841–1847.

[91] J.G. Proakis and M. Salehi. *Digital Communications*. McGraw-Hill, 2008. ISBN: 9781283387460.